University of Birmingham

Quantum metrology with a single ytterbium ion optical clock

Author:
Jonathan Jones

Supervisor:
Prof. Kai Bongs
Dr Rachel Godun

A thesis submitted to the University of Birmingham for the degree of DOCTOR OF PHILOSOPHY
September 2017

Experimental work carried out at:

National Physical Laboratory
Hampton Road
Teddington
Middlesex
TW11 0LW

NPL
National Physical Laboratory

Abstract

The thesis is focused on the developments and measurements of the Yb^+ optical clock at NPL. During my period there, new ion traps, trap control electronics and optical cavities have been developed. Numerous measurement campaigns have been conducted, where we measured the absolute frequency of both optical clock transition in Yb^+ relative to caesium, for the first time ever directly measured the frequency ratio of these transitions, and performed numerous international comparisons against other optical clocks. The total systematic uncertainty of the clock is now expected to be at the mid-low 10^{-18} level, with published uncertainty budgets at the mid 10^{-17} level, making it a strong candidate for a future redefinition of the second.

The exotic electron structure of the excited levels in Yb^+ make it a promising system for tests of fundamental physics. The frequencies of the transitions used in the Yb^+ clock are highly sensitive to changes in the fine structure constant, α, which is predicted to vary by many physical theories beyond the standard model. By combing our absolute frequency measurements with a history of atomic clock measurements, we can place new best limits on the present day time variation of α, and the proton-electron mass ratio, μ.

Acknowledgements

A great thanks goes out the members of the Yb^+ team I worked with whilst at NPL: Rachel Godun, Steven King, Peter Nisbet-Jones and Charles Baynham. Thank you for teaching me what I know and making my time there so enjoyable. A particular thanks goes to Rachel, who as my supervisor at NPL has provided many useful comments about the content of this thesis. I also extend a thanks to the other ion trappers at NPL, Hugh Klien, Geoff Barwood and Guido Wilpers, and the head of the combs team Helen Margolis, for providing very useful discussions and advice, especially over a cup of tea. I am additionally grateful to Kai Bongs and the cold atoms group at Birmingham.

I would also like to thank my family for their continued support throughout my studies.

My thanks also go to the gravitational waves group at Birmingham for making their optics graphics library available at `http://www.gwoptics.org/ComponentLibrary/`, which is used as a basis for many optical setups illustrated in this thesis. ComponentLibrary by Alexander Franzen is licensed under a Creative Commons Attribution-NonCommercial 3.0 Unported License.

Contents

List of Figures

List of Tables

CHAPTER 1

Introduction

This chapter introduces the reader to both the discipline of precision frequency metrology, and ultra cold atoms. These, when combined, have produced the atomic clock - a precise frequency reference that allows for the realisation of both the second and hertz units more accurately than any other unit in the SI system [14]. This thesis focuses on developments and measurements of the ytterbium ion optical clock based at the National Physical Laboratory (NPL) in Teddington, the UK's national metrology institute responsible for the UK's realisations of the SI units. After introducing the reader to both the history of and key concepts behind both frequency metrology and cold atom physics, we will move on to a brief discussion of state of the art optical and microwave clock systems, and then an outline of the content and scope of this thesis.

1.1. Setting the scene

The measurement of time has long been an important development for civilisation. Both short term time measurements that allow for a day to be subdivided, to longer term time keeping, allowing for the accurate prediction of season changes and precession of the Earth were developed my early civilisations. Many of these early 'time scales' involved observations of astronomical bodies - a calendar based on phases of the moon, equinoxes and solstices for

example, and the use of the shadow of a large structure to measure the time within one day, such as the obelisks built by the ancient Egyptians. These are not the most portable solution for the time keeper on the go, and quickly more user friendly solutions were developed. A common clock was based on the regulated drainage of water through a hole. Another early example would be the burning of a candle or lamp with graduated marks [15]. Most people are familiar with the hourglass - another early portable clock. These solutions all have one thing in common - they integrate the change of a quantity that is monotonically varying in order to calculate the time elapsed from when the clock was started. This is still true today, where an atomic clock is essentially counting the number of oscillations of an electric field.

Historically, even until the 1950's, the time scale has been set by the motion of the earth, with one second being defined as 1/86 400 of a mean solar day[16], with a redefinition in terms of a fraction of a year in 1956. Atomic time was born with the first successful demonstration of the caesium beam clock at NPL by Louis Essen, building on previous work conducted at NBS in the USA and Essen's work with crystal oscillators. This clock was based on measuring the frequency of the microwave transition between the two hyper-fine states of caesium's ground state. After a series of measurements that compared the caesium clock to the astronomical time scale that, at the time, was the definition of the second, the advantages of atomic time were obvious and a redefinition was possible. In 1967 the CGPM redefined the second as:

> The second is the duration of 9 192 631 770 periods of the radiation corresponding to the transition between the two hyperfine levels of the ground state of the caesium 133 atom [16].

In 1997 the definition was clarified to be a caesium atom at rest and at 0 K. The convention of reporting atomic frequencies at absolute zero has been carried over to other atomic frequency standards, including optical clocks.

1.2. Progress of cold atoms

Over the past few decades, (cold) atomic physics research has been one of the most active and rewarded areas of research - from laser cooling single trapped ions[1] [17], to the creation of Bose-Einstein condensates [18, 19] which was

[1] Through this thesis 'atom' can refer to both neutral atoms and ions.

awarded the Nobel prize in 2001 [20], testing quantum information protocols on strings of trapped ions [21], to testing fundamental physical theories with atomic clocks (for example [22, 23, 24, 25, 26]), ultra cold atoms are staking a claim as the work horse of the modern physics laboratory. This is in part due to the near ideal quantum states one can produce with the interaction of coherent laser light and atoms. The atom can be trapped and cooled to just above absolute zero, and due to the weak coupling to the environment and strong coherent interactions with the light, the desired quantum state can be engineered and still have a low level of decoherence making experimentation attainable.

The development of the laser is the driving force behind the explosion of cold atom research. The narrow frequency distribution and tunability of the laser enables easy Doppler and sub-Doppler cooling of atoms. When combined with the electrodynamic Paul trap, it enables a single ion to be cooled to near the quantum ground state of the trapping potential. This cold single ion is the basis of optical ion clocks at NPL.

1.3. Progress of optical clocks

Optical clocks were first suggested around the time that single ion traps and laser cooling were being first developed [27], Dehmelt considered a narrow optical transition in a well isolated, trapped ion to potentially be the ultimate laser frequency standard. During the next 20 years, a number of candidate transitions in ions were identified [28], one of the most interesting of which was the incredibly narrow electric octupole transition in singly ionised ytterbium [29, 30, 31, 32] which is used substantially in this thesis.

One of the major developments that has helped the advance of optical clock technology was the development of the frequency comb [33]. This device acts as a frequency gearbox, allowing the high optical frequency to be directly referenced to the much lower microwave frequencies that can be easily counted and currently define the second. This innovation also has applications in other spectroscopy based technologies, and was considered important enough to be awarded the Nobel prize [34]. These systems not only allow for a much simpler measurement of the frequency of the light, but also allow for the stability of one laser to be transferred across the whole optical spectrum.

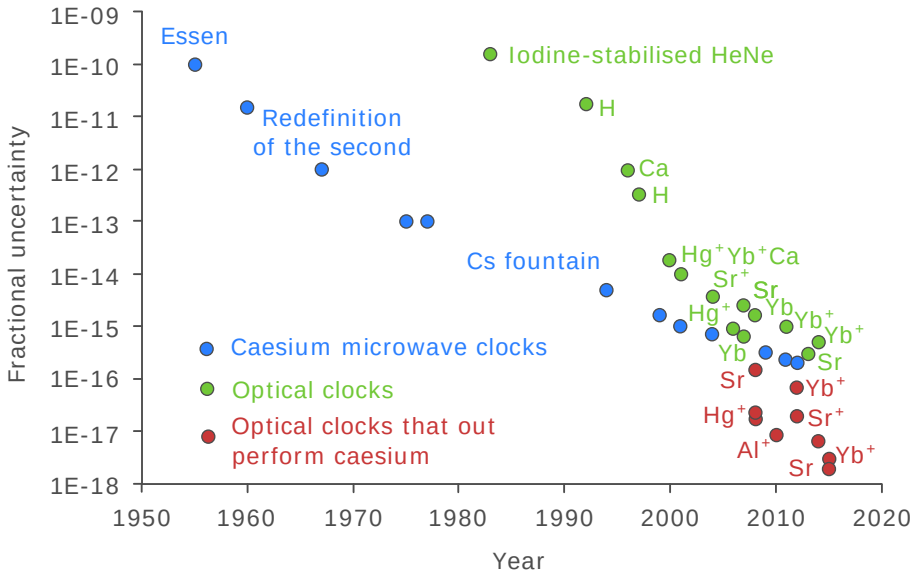

Figure 1.1: Progress of atomic clocks since the first caesium clock developed by Louis Essen. Figure updated and adapted from [1].

1.4. The optical atomic clock

An atomic clock has 3 main subsystems - the local oscillator, the atomic reference, and the frequency counter. Modern atomic clocks fall into 2 categories - microwave and optical, based on the frequency of the clock transition used. Microwave clocks have been around as early as the 1930s, but the first accurate system that spurred the redefinition of the second was developed at NPL in the 1950's by Louis Essen. It consisted of a thermal beam of caesium atoms that experienced a Ramsey style interrogation of the hyperfine ground state splitting of 9.19 GHz. Modern versions of this clock are available today, with most rack mounted commercial atomic clocks functioning in this manner. Once laser cooling was discovered, the accuracy of the caesium clocks could be further increased, using a 'fountain'. A cold stationary cloud of caesium can be produced and, using a laser, launched about 1 m vertically. A microwave cavity is placed near the start of the cloud, such that the cloud passes through it twice: once on the way up and once on the way down. This technique allows for a much longer time between the 2 Ramsey pulses than any reasonably sized beam clock, meaning the observed resonance is much narrower, and allows for much better control of the systematics allowing for more accuracy. The best caesium clocks

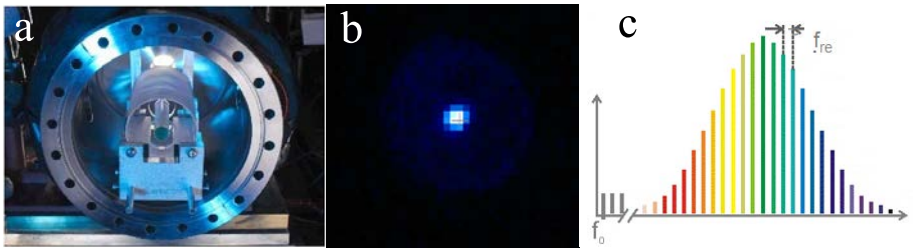

Figure 1.2: The 3 components of an ion optical clock. (a) A laser locked to a high finesse cavity provides a very fast "ticking" electric field. (b) This is referenced to a highly forbidden and spectrally narrow atomic transition in a single ion. (c) A frequency comb allows this optical reference to be measured and transferred across the optical and microwave/RF frequency spectra.

today operate using this technique.

There are 2 main types of optical clock: ones based on a large number of neutral atoms trapped in a 'magic' wavelength optical lattice, and ones based on one or more ions trapped in an electrodynamic Paul trap. This thesis is concerned with the latter. No matter which type of optical clock, they are broadly similar, with the main difference being the number and confinement of the atomic references. The other clock subsystems are broadly similar. Figure 1.2 shows the 3 major components of a single ion optical clock.

1.4.1. Local oscillator

The local oscillator produces the frequency that will ultimately be output by the clock. The frequency can be either a microwave or an optical frequency, depending on the clock. What is important for the clock operation is that the frequency is spectrally pure, stable enough, and agile enough to be disciplined to the atomic reference.

1.4.2. Atomic reference

The atomic reference is generally going to be some 'forbidden' electronic transition in a carefully prepared sample of atoms, or single ion. Forbidden transitions are electronic transitions that are not allowed when using the electric dipole approximation. Because they only occur through much weaker multipoles, they are spectrally much narrower, and it is this narrow, well defined frequency that makes them a useful frequency reference. For the sake of clarity not only do

they possess a very narrow frequency, all atoms of a given element isotope are identical, and as such every atomic clock will be referenced to the same ideal frequency. By tuning the frequency of the local oscillator to the atomic resonance and using a servo algorithm to keep it there, we ensure the output of our clock is referenced to the atomic transition. Atoms make an ideal reference not only because they are all identical, but also because of their weak interaction with the environment. We can cool them to just a fraction of a kelvin above absolute zero, and store them in an ultrahigh vacuum to minimise interactions with background gas. Even so, there are still some small perturbations to the atomic transition frequency caused by interactions with, e.g., the black body spectrum of the experimental chamber, residual magnetic fields etc. Careful evaluation and minimisation of these effects is essential for a meaningful performance of the clock, and has been at the centre of atomic clock research since the birth of atomic time.

1.4.3. Frequency counter

The final component of the clock is a frequency counter. This allows the ticking of the clock to be converted into some sort of time scale, and also allows different clocks to be compared against each other. For a microwave clock it could be something as simple as fast electronics. For the optical clocks something different is required that can cope with the extremely high optical frequencies - the frequency comb. This is a pulsed mode locked laser that produces an output of evenly spaced 'teeth' in the frequency domain (hence the name comb). These teeth are spaced by a radio or microwave frequency, often in the region of a few hundred MHz. By beating the laser with a nearby tooth, we produce a low frequency beat note that can easily be counted with electronics. The tooth frequency is simply the tooth number multiplied by the spacing between the teeth, plus any offset frequency of the first tooth. Furthermore, the frequency comb can be used to directly measure the frequency ratio of 2 or more optical clocks without needing accurate knowledge of the RF/microwave frequencies[35]. Figure 1.3 shows a typical setup for measuring the absolute (referenced to caesium) frequency of an ion optical clock. The invention of the frequency comb was rewarded with the Nobel prize in physics in 2005 [34].

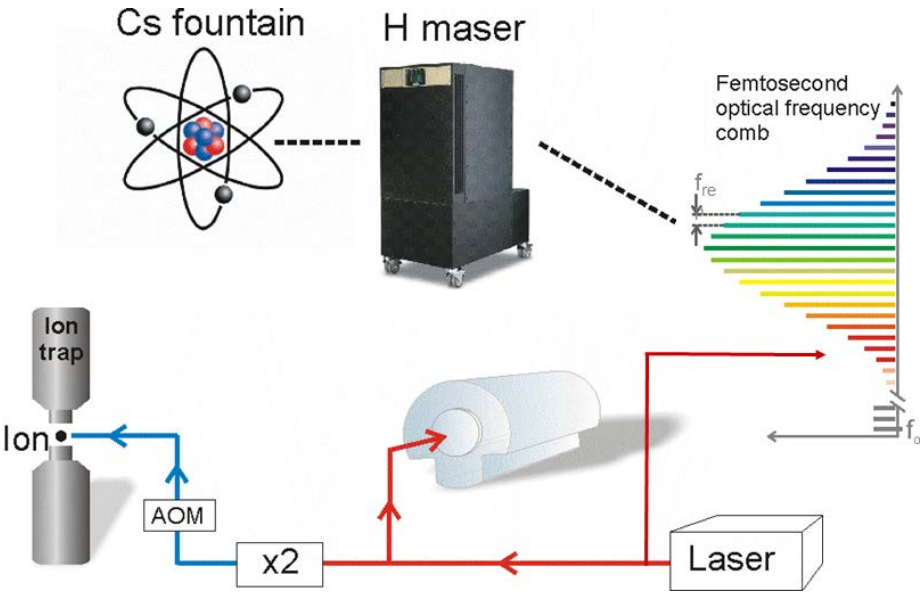

Figure 1.3: A frequency comb has optical 'teeth' separated by a microwave/RF repetition frequency of the pulsed laser. The resultant of beating the atomic referenced laser to the comb is an RF frequency. These RF frequencies can all be counted easily and referenced to the local time scale produced by a hydrogen maser. This timescale is calibrated by a caesium fountain to link it to the SI second. Note the colours of the teeth here just represent a generic change in frequency - the comb is mostly in the NIR. Figure adapted from [2].

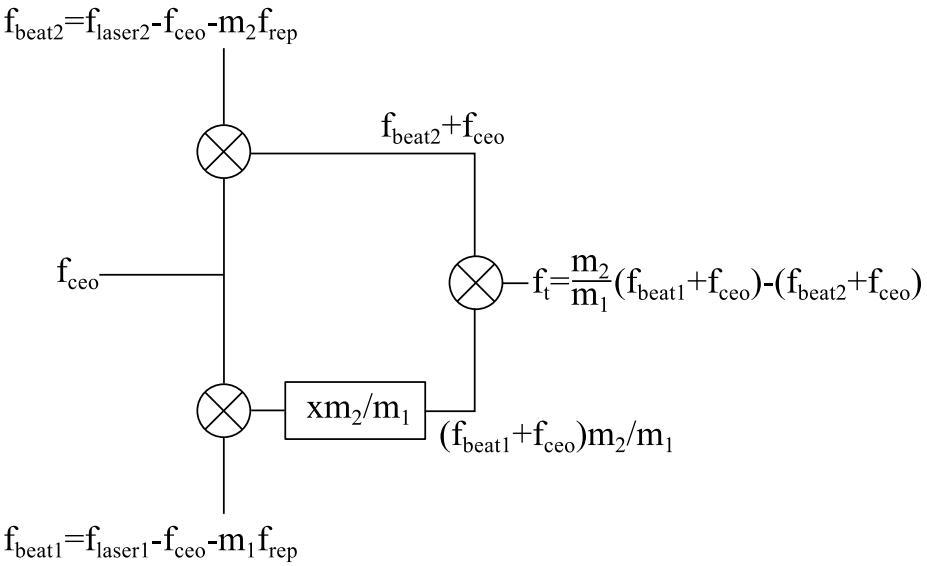

Figure 1.4: Mixing procedure for producing the transfer beat f_t between 2 optical frequencies f_1 and f_2. The beats between the lasers and the comb, f_{beat1} and f_{beat2} are mixed with the carrier envelope offset frequency. One of the intermediate beats is then scaled by m_2/m_1 before being mixed with the other intermediate beat. The resultant transfer beat f_t is not a function of the comb's microwave frequencies f_{rep} and f_{ceo}.

Frequency comb

The 'teeth' of the frequency comb are spaced by the repetition rate of the pulsed laser, f_{rep}, and offset from zero by f_{ceo}, caused by a change in phase from pulse to pulse of the laser (carrier envelope offset). Beating the clock output with the nearest mode of the frequency comb, the frequency of the clock can be measured relative to that of an RF or microwave standard governing f_{rep} and f_{ceo},

$$f_{laser} = f_{beat} + mf_{rep} + f_{ceo}. \tag{1.1}$$

When measuring the ratio of 2 optical frequencies, f_1 and f_2, a transfer beat, f_t, between the 2 lasers is created, shown in figure 1.4. The beat frequency f_{beat} of each laser is mixed with the offset frequency of the comb. One of the resultant beat frequencies is the multiplied by the ratio of the comb mode numbers m_2/m_1 before being mixed directly with the other intermediate frequency. This gives

the transfer beat,

$$f_t = \frac{m_2}{m_1}(f_{beat1} + f_o) - (f_{beat2} + f_{ceo}) \tag{1.2a}$$
$$= \frac{m_2}{m_1}(f_1 - m_1 f_{rep}) - (f_2 - m_2 f_{rep}) \tag{1.2b}$$
$$= \frac{m_2}{m_1} f_1 - f_2 \tag{1.2c}$$

which is a purely a function of the two optical frequencies f_1 and f_2 and independent of the microwave frequencies used to operate the comb, f_{ceo} and f_{rep}. This technique is not only used to measure the optical frequency ratio of optical clocks, but also to transfer the stability of an ultra stable laser across the frequency combs spectrum. The optical frequency ratio can then be found,

$$\frac{f_1}{f_2} = \frac{m_1}{m_2}\left(1 + \frac{f_t}{f_2}\right). \tag{1.3}$$

The precise value of f_t and f_2 only need to be known to 10^{-11} in order to determine the frequency ratio to 10^{-18}[35].

The performance of the NPL frequency combs has been demonstrated beyond even state of the art optical clocks, with comb-comb agreement of an optical frequency ratio at the 3×10^{-21} level[35].

1.4.4. Quantifying the performance of frequency standards

There are 2 figures of merit, accuracy and stability, that are used to quantify the performance of a frequency standard, and a third, the reproducibility, that quantifies the agreement between different frequency standards based on the same transition.

Accuracy

The ultimate accuracy of a frequency standard is the systematic uncertainty of the clock. A clock can have relatively large systematic shifts, but if they are precisely known they can be very accurately corrected for and thus the clock can be very accurate. A clock may also have very small but poorly known systematic effects, leading to an inaccurate clock. Chapter 6 focuses on the analysis of the systematic effects in Yb^+.

Stability

The stability of a clock tells us about the statistical noise of the output. It is normally characterised by an Allan deviation, or modified Allan deviation, though on occasion spectral phase or frequency noise plots can be used. If we imagine a discretely sampled time series of frequency data y_i, with M samples, each averaged over a sample time τ for a total measurement time $T = M\tau$, the Allan deviation is given by[36, 37, 38],

$$\sigma_y(\tau) = \left[\frac{1}{2(M-1)} \sum_{i=1}^{M-1} (y_{i+1} - y_i)^2 \right]^{1/2} . \tag{1.4}$$

The minimum sampling time is determined by the systems measurement interval. In general this will be of the order 1 s for the majority of clock comparisons. The Allan deviation is a generalisation of the standard deviation of a data set that allows for non-white noise processes. It calculates the average difference between neighbouring data points of a data set at different time scales. For example, the 1 second Allan deviation is the average difference between all the data points that are one second apart, the 10 second Allan deviation is the average difference between neighbouring data points that are averaged into 10 second chunks etc. By looking at how the Allan deviation changes as a function of this timescale we can learn about what noise processes the underlying data exhibits and at what timescales. A whole family of modifications to the Allan deviation exists, which changes the response of the deviation to different noise spectra, and make more efficient use of the available data, reference [38] gives a detailed analysis of different deviation types used to analyse frequency stability. All forms of the Allan deviation converge with the standard deviation in the limit of white noise.

The clock laser is stabilised by excitation information from a finite number of atoms. This leads to statistical fluctuations - noise - of the error signal. This is termed quantum projection noise, since the statistical fluctuations are caused by the projection of the superposed quantum state of the atoms onto basis states for the measurement [39]. Creating an optimum servo routine that stabilises a laser to the atomic transition has been covered in detail [40]. The stability of an atomic clock operating on a transition frequency ν, with a signal to noise ratio of SNR, and an observed transition line width of $\Delta\nu$, has a stability of,

$$\sigma_y(\tau) = \frac{1}{\pi}\frac{\Delta\nu}{\nu}\frac{1}{\mathrm{SNR}}\sqrt{\frac{1}{\tau}}, \tag{1.5}$$

where the factor of π is a line shape dependent constant, depending on the exact form of spectroscopy being used. Different forms of spectroscopy will be discussed in chapter 5.

The quantum projection noise sets a natural limit of the stability a particular clock can achieve[2]. For a lattice clock, with $\sim 10^4$ atoms sampled each cycle, this stability can be extremely small, for a single ion clock, the value is much larger. Single ion clocks repeatedly probe the transition in a serial manner to average out the projection noise, operating with a cycle that can contain many clock pulses before the clock frequency is updated. Since the probes happen one after another the stability of the ion clock is not improved by increasing the number of probes per cycle, since the amount of information acquired per unit time is the same. Increasing the number of probes per clock cycle gives better information, lowering the statistical noise, at the expense of a longer acquisition time, reducing the ability of the servo to dynamically respond to noise processes. The number of probes per cycle should balance the reduction in statistical noise, making the frequency updates more accurate, with the increased time taken to update the servo, making the servo more susceptible to drifts and other frequency fluctuations.

1.4.5. State of the art

As of writing there are currently a large number of optical clocks with total systematic fractional frequency uncertainties in the mid-low 10^{-17} range [42, 43, 44, 45, 46, 47]with a handful of clocks in the 10^{-18} range[3, 48, 49]. The best optical lattice clock has an uncertainty of 2×10^{-18}[48] and the best ion clock is at 3×10^{-18}[49]. The best caesium fountains, which are used to realise the SI second, are at about 1×10^{-16}(see, for example, [50]). The red points in figure 1.1 show the reported optical clocks that have a superior uncertainty budget to the best caesium fountains. It is clear that the modern optical clocks are outperforming the microwave clocks as a precision frequency standard, with numerous different clocks competing for the lowest uncertainty.

Historically there have been problems with the reliability of optical clocks, however as laser technology improves and experimenters take part in large scale

[2]There are quantum enhanced detection methods that allow for quantum projection noise limit to be surpassed, e.g. [41]

measurement campaigns concerted efforts have been made to increase their reliability, with many European systems demonstrating uptimes of over 70% during multiple weeks of running. These developments are making an ever stronger case for an optical redefinition of the second, although which transition is chosen is still up for debate. This further motivates direct comparisons of optical clocks not only against caesium, but against other optical clocks of both the same and different species. A large number of international comparisons would demonstrate reproducibility, allowing for the redefined time scale to have a smooth transition, and would allow countries without the chosen optical clock to still maintain an SI referenced optical time scale.

1.5. Beyond Timekeeping

Atomic clocks are some of the most precise measurement tools ever created. Due to this unprecedented precision, they are useful as tools for investigating fundamental physics that usually manifests itself at such a low level as to be unimportant to the vast majority of experiments. An early example of this was the Hafele-Keating experiment [51], which used atomic clocks to test relativity. A clock was flown on a plane, and compared to a clock that remained on the ground. The difference between the clocks was consistent with the predictions of general and special relativity.

One such area is theories beyond the standard model that predict time variations of the constants of nature, such as topological defect dark matter [52, 53, 54]. Since these constants of nature determine the structure of atoms, changes in these constants would manifest as changes to the energy levels of atoms, and therefore changes to the frequency of atomic clock transitions. Throughout this section, conventions from Lea [22] will be used. In order to discuss changes in these constants in a meaningful way, one must be concerned with the dimensionless constants of nature, in this work we shall discuss the fine structure constant $\alpha = \frac{e^2}{4\pi\varepsilon_0\hbar c}$, and the proton-electron mass ratio $\mu = m_p/m_e$. The reason for using dimensionless constants is that different unit systems can observe changes in different constants purely because of the way the units are defined - consider trying to observe changes in the speed of light using a unit system where length is measured in light years and time in years, the speed of light $|c| \equiv 1$ by definition of the unit system, see refs[55, 56] for a discussion on this idea. These dimensionless constants take the same value in all unit systems, and so changes in the constant are unambiguous.

The frequency of an atomic clock transition will be dependent on the gross structure, fine structure and hyperfine structure of the atom. Generally optical transitions are most dependent the first 2, whilst microwave transitions are strongly determined by the hyperfine structure [22]. The gross and fine structure have a dependence on the fine structure constant α, and the hyperfine structure is dependent on the nuclear magneton, $\mu_N = \frac{e\hbar}{2m_p}$, and Bohr magneton, $\mu_B = \frac{e\hbar}{2m_e}$[57], the ratio of which is equivalent to the proton-electron mass ratio, $\mu = m_p/m_e$. In order to measure the change in an atomic clock frequency, it must be compared to a reference frequency such as that from another atomic clock based on a different transition. The fractional rate of change in the ratio of these frequencies, $r = \nu_1/\nu_2$, is then given by [22],

$$\frac{\dot{r}}{r} = (A_1 - A_2)\frac{\dot{\alpha}}{\alpha} + (B_1 - B_2)\frac{\dot{\mu}}{\mu} \tag{1.6}$$

where A_i is the fine structure sensitivity of the i clock transition, and B_i is the sensitivity of the i transition to changes in μ. These sensitivity coefficients are regularly calculated by theory groups, see [58, 59, 60] for examples. Optical clocks in general have $B \approx 0$ and microwave clocks $B \approx 1$. The intercombination lines used for neutral Sr, Al^+ etc have A very close to zero[61], whereas the dipole forbidden transitions in Yb^+ and Hg^+ have a sensitivity close to $|1|$ or greater [60]. The E3 and E2 transitions in Yb^+ have the largest negative and positive A sensitivities of all transitions currently being used in optical clocks. This makes the ratio between them of great interest for testing fundamental physics that depends on electromagnetic couplings, and hence α. In addition to this, absolute frequency measurements, relative to caesium, can also be used to derive limits of changes in both α and μ.

There have been numerous experiments that have attempted to measure such changes in these dimensionless constants. Many are based on absorption lines in the gas clouds of the early universe [62, 63, 64]. Some of these measurements have observed a statistically significant change and even a spatial variation of the fine structure constant. Laboratory based measurements based on atomic clocks [45, 60, 65, 61, 22] and transitions in dysprosium [66, 4] provide a complementary test to this, and as of yet no statistically significant results have been reported, though increasingly stringent limits are being placed on any possible variation.

1.6. Thesis outline

This thesis details work carried out on the ytterbium ion optical clock at NPL. During the time period of this work, we have developed a new ion trap system and electronics, including RF trap drive resonators and DC micromotion compensation. Various improvements to the laser systems have been made, including changes to the frequency doubling of the clock lasers and construction of a new clock laser cavity, as well as the ability to lock to the universal synthesiser. Over the course of this research a number of measurement campaigns have been completed, including the first direct ratio measurement of the E3/E2 Yb^+ clock transitions, the strongest constraint on $\dot{\mu}$, first multi-way direct comparison of European optical clocks.

This thesis starts with an overview of the ytterbium ion, looking at its structure, cooling cycle and the clock transitions. We will then move on to the trapping of ions in electrodynamic Paul traps, how these are implemented at NPL, and how the new NPL design improves over other designs. A chapter will be dedicated to the spectroscopy of dipole forbidden transitions, which will provide some crucial techniques that are used in the latter chapters. The experimental set-up of the lasers will then be described, giving the reader information on how the optical systems are set up, and how the experimental sequence works. We will then move on to the evaluation of the systematic frequency shifts of the clock transitions - the purpose of this chapter is to provide some theoretical frame-work where appropriate and a description of how we calculate, control and analyse the shifts. The final chapter details the measurement campaigns that we have taken part in, which is the summation of the work in all of the previous chapters. Included are both published and unpublished results.

CHAPTER 2

Ytterbium ions

The work in this thesis is based on experiments with singly ionised ytterbium. In this chapter the basic properties of the element shall be introduced, and some of the more interesting and unique properties that make it a viable optical clock and interesting system to study physics shall be highlighted.

2.1. Structure

Ytterbium is a heavy lanthanide element, with an atomic number of 70. There are 7 observationally stable isotopes of ytterbium, table 2.1, of which the 171 isotope is used exclusively in this work. The neutral atom has group II type

Isotope	Nuclear Spin	Abundance
^{168}Yb	0	0.13%
^{170}Yb	0	3.05%
^{171}Yb	1/2	14.3%
^{172}Yb	0	21.9%
^{173}Yb	5/2	16.12%
^{174}Yb	0	31.8%
^{176}Yb	0	12.7%

Table 2.1: Naturally abundant isotopes of ytterbium, abundances taken from [11]

structure, and can be ionised by either electron bombardment or photoionisation.

To photoionise, a laser at 399 nm excites the $^1S_1 \rightarrow {}^1P_1$ transition. From this state excitation to the continuum requires a photon at 394 nm or shorter wavelengths, though it is also possible to ionise with a second 399 nm photon and the large electric field of the ion trap[11]. Of the stable and naturally abundant isotopes, $^{171}Yb^+$ possesses a number of favourable attributes for an atomic clock, namely it is the only isotope with nuclear spin $I = 1/2$, meaning it has magnetically insensitive $\Delta m_F = 0$ transitions, whilst still having a simple magnetically sensitive structure for cooling and state selection.

Singly ionised ytterbium has alkali-like structure, see figure 2.1 for a simplified term scheme. There is a strong $^2S_{1/2} \rightarrow {}^2P_{1/2}$ transition at 370 nm, with a natural linewidth of $\Gamma = 19.6 \times 2\pi$ MHz[67] suitable for Doppler cooling. There is a small chance of decaying from the $^2P_{1/2}$ state to the metastable $^2D_{3/2}$ state. This state can be depopulated with 935 nm light, which excites to a $^3[3/2]_{1/2}$ state that rapidly decays to the ground state. There is occasional (twice per day) population of the stable $^2F_{7/2}$ state, which is believed to be caused by collisional excitation of $^2D_{3/2} \rightarrow {}^2D_{5/2}$, which can then decay to $^2F_{7/2}$ with 83% probability[68]. This state is then depopulated with 760 nm light to the $^1[3/2]_{3/2}$ state. Note that this repumping transition is forbidden by electric dipole selection rules.

Due to having nuclear spin, the 171 isotope has hyperfine structure, with a ground state splitting of 12.6 GHz. The integer hyperfine quantum numbers results in the Zeeman structure of the levels having $m_F = 0$ components, allowing for spectroscopy insensitive to magnetic fields to first order. The hyperfine structure also allows the quadrupole transition at 436 nm to be used with a simple state detection technique, since the cooling cycle only populates the $^2D_{3/2}$(F=1) state, we can use the F=2 state for the electron shelving detection.

The electronic structure of Yb^+ can explain some of its more unexpected properties that are elaborated on in section 2.1.3. It has features in common with many group II ions. The ground state configuration is $[Xe]4f^{14}6s$. The D state has a familiar excitation of the $6s$ electron to $5d$.The configuration of the F state is $[Xe]4f^{13}6s^2$, so we see that a core electron has been excited to the now full $6s$ orbital, leaving a hole in the $4f$ orbital. The hole interacts strongly with the $6s^2$ valence electrons, resulting in very large and inverted fine structure splitting, leaving the $^2F_{7/2}$ state as the lowest excited state. This state is very stable as it can only decay to the ground state via a heavily supressed electric

octupole transition.

2.1.1. Cooling cycle

In order to remove the substantial line broadening and shift of the Doppler effect, the ion must be cooled to a point known as the Lamb-Dicke regime [69]. In this regime, the ion is spatially confined to a region much smaller than the wavelength of the interrogating light. Recoil energy from absorption of a photon from the clock beam is insufficient to change the motional quantum number of the ion, resulting in Doppler free spectroscopy to first order. Given a sufficient trap depth, the Lamb-Dicke regime can be reached with simple Doppler cooling.

Yb^+ has a fast cycling accessible transition at 370 nm that is suitable for cooling the transition, with a natural line width resulting in a Doppler cooling limit of 0.5 mK. By operating on the $^2S_{1/2}(F = 1) \rightarrow {}^2P_{1/2}(F = 0)$ transition we create an almost closed cooling cycle, since decay from the $P_{1/2}(F = 0)$ to the $S_{1/2}(F = 0)$ is strictly forbidden. There is a small decay channel from the P state to the meta stable D state, which can be repumped by 935 nm light. This, along with a small chance to off resonantly excite the $P_{1/2}(F = 1)$ state, can result in the ion ending up in the $S_{1/2}(F = 0)$ ground state. In order to pump the ion back into the cooling cycle, the hyperfine ground states must either be mixed using microwaves, or the F=0 ground state can be directly pumped by light addressing the $^2S_{1/2}\,(F = 0) \rightarrow {}^2P_{1/2}(F = 1)$ transition, which can decay to either of the hyperfine levels of the ground state. A similar scheme can be used to prepare the ion in the F=0 ground state for the spectroscopy operations. The $^2D_{3/2}(F = 2)$ state is the clock state of the E2 436nm transition, so in order to perform electron shelving we need to be able to run the cooling cycle without depopulating the F=2 state. Therefore the experimenter must ensure that the 2 hyperfine levels of this state can be depopulated separately.

Due to the magnetic structure of the upper and lower states in the cooling transition, care must be taken to avoid population trapping in a coherent dark state. When operating in a low magnetic field, a coherent superposition of the magnetic sub levels of the F=1 ground state can be created, which cannot be addressed by any static polarisation of the cooling laser. This can be avoided by working in a sufficiently large magnetic field to lift the degeneracy of the Zeeman levels, allowing a time dependant phase to develop between them. A coherent dark state can also be destabilised by 'spinning' the polarisation of a cooling beam with respect to a fixed π polarised second cooling beam. By

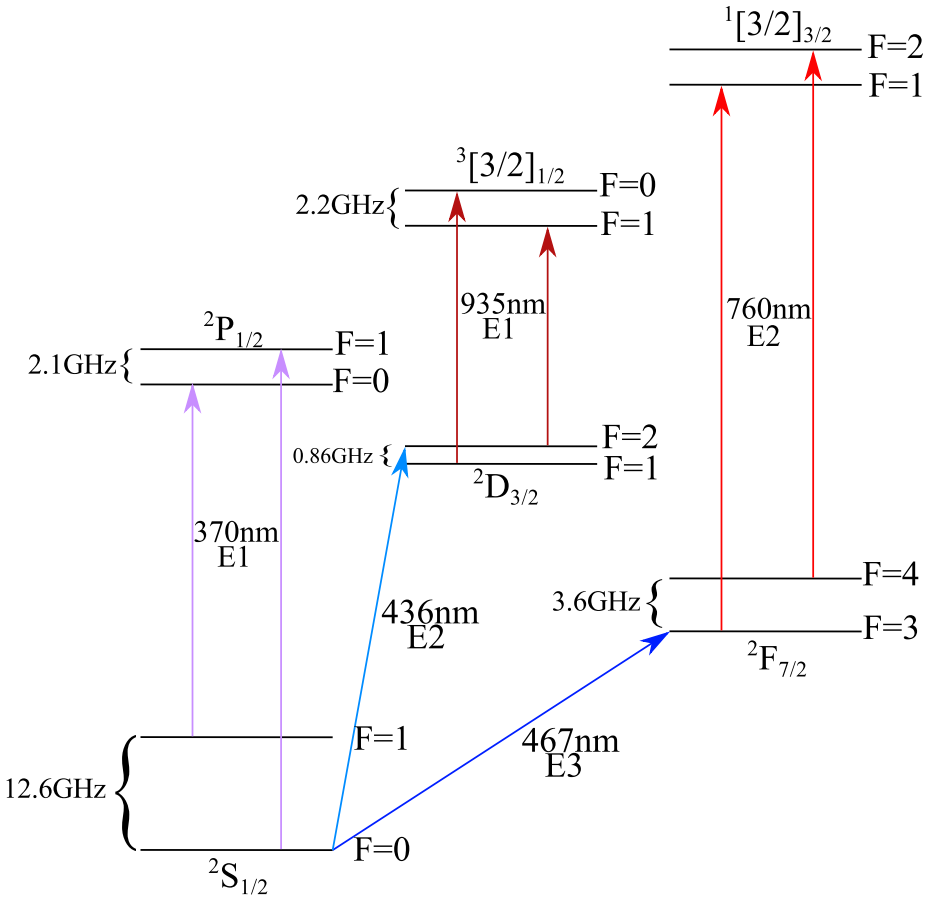

Figure 2.1: Partial term scheme of $^{171}Yb^+$, showing all of the relevant energy levels and transitions, with optical transitions given in nanometres and hyperfine splittings given in gigahertz. Throughout this report, the electric quadrupole transition at 436nm will generally be referred to as the E2 transition, and the electric octupole transition at 467nm as the E3 transition. All other optical transitions will be referred to by their wavelengths.

quickly modulating the polarisation of a beam from $\sigma+$ to $\sigma-$, we ensure that any superposition of states can be addressed. Although this is not as effective as a large magnetic field, and is experimentally more complicated, it is very useful when quickly switching magnetic fields is impractical. A similar coherence effect can be observed in the 935 transition, where the D state develops a coherent dark state that cannot be addressed. This requires a much smaller magnetic field to destabilise than the S state, with the operating field of a few μT being perfectly adequate, thus no polarisation spinning is required. See reference [70] for a detailed analysis of this phenomenon and how to avoid it.

2.1.2. Clock transitions

There are a number of transitions in Yb^+ that have been used as frequency standards. The ground state splitting of the 171 isotope is suitable for use as a microwave standard, and the 3.43 μm transition between the $^2F_{7/2} \rightarrow {}^2D_{5/2}$ has been proposed, as has the 411 nm transition between $^2S_{1/2} \rightarrow {}^2D_{5/2}$[68]. The two transitions in Yb^+ currently recognised as secondary representations of the second by BIMP are both used in this work. The first is the quadrupole allowed $^2S_{1/2} \rightarrow {}^2D_{3/2}$ transition at 436 nm. Because of the use of electron shelving to detect the ion state, this transition is only available in odd isotopes[1] . The transition has a natural linewidth of around 3 Hz, and as such it is a useful frequency standard, but the standard is limited by the lifetime of the state.

The other transition is the electric octupole allowed $^2S_{1/2} \rightarrow {}^2F_{7/2}$ transition at 467 nm. This transition is incredibly narrow, with a natural line width of $\sim$nHz. This means for all practical purposes the lifetime of the transition will never limit clock operation. This transition occurs when a core electron is excited into the $6s$ orbital. Due to the involvement of the core and the compact spatial extent of the $6s$ orbital, the transition has a much lower sensitivity to external field perturbations than the quadrupole transition, generally by around one order of magnitude.

These two clock transitions are both accepted secondary representations of the SI second, with the BIPM giving them frequencies of

$$\nu_{436} = 688\,358\,979\,309\,308.3\,\text{Hz}, \tag{2.1}$$

[1] One could use this transition in an even isotope by transferring the ground state population to the F state and then performing electron shelving detection. This would vastly increase the complexity of running the clock

Clock Species	Transition	A_α	B_μ
Cs	$^2S_{1/2}(F=3) \rightarrow {}^2S_{1/2}(F=4)$	2.83	-1
Yb^+	$^2S_{1/2} \rightarrow {}^2D_{3/2}$	0.88	0
Yb^+	$^2S_{1/2} \rightarrow {}^2F_{7/2}$	-5.95	0

Table 2.2: Sensitivity factors to changes in α and μ for transitions relevant to this work [12].

and

$$\nu_{467} = 642\,21\,496\,772\,645.0\,\text{Hz}, \tag{2.2}$$

both with a fractional standard uncertainty of $\sigma/\nu = 6 \times 10^{-16}$[71]. We shall also see later that both of these transitions are relatively insensitive to external electric and magnetic fields.

2.1.3. Yb^+ as a physics probe

As discussed in chapter 1.5, the frequency of atomic transition depends on the constants of nature, and thus atomic clocks make a prime candidate to test if these constants are changing. The large and inverted fine structure, caused by the electron-electron and electron-nucleus correlations means that there are large relativistic corrections to the F state energy level, giving a much larger and negative sensitivity to changes in α than other transitions commonly used for optical clocks. In addition to this, the E2 transition has the most positive α sensitivity of optical clock transitions, leaving the E2/E3 frequency ratio as the most sensitive optical ratio to changes in α. Sensitivities for the 2 optical transitions used in Yb^+ and the groundstate splitting in Cs that currently defines the second are shown in table 2.2. By making absolute frequency measurements relative to caesium, we can increase the sensitivity to α and also introduce a sensitivity to μ.

The long excited lifetime of the F state make it a suitable candidate for an interferometric experiment that examines the isotropy of the laws of physics. In an analogous way to the famous Michelson-Morely experiment, one can use the electron magnetic substates of atoms as an electronic test of Lorentz invariance, as first described and demonstrated in [72]. In this experiment an entangled pair of calcium ions were prepared in superposition of magnetic substates of the metastable D state. It has since been proposed that using ytterbium ions would provide an improved sensitivity of this experiment of up to 3 orders of

magnitude. This is because the lifetime of the F state would allow for much longer interference times than the comparatively short lived D state of calcium, and the sensitivity of the F state is over an order of magnitude larger than the D (in either Yb^+ or Ca^+)[73]. Since this requires operations on the clock state of ytterbium, we are in a great position to attempt this experiment. To operate in a manner similar to [72], a linear trap would be required.

The high mass and numerous stable isotopes also makes ytterbium a promising system to measure Higgs coupling constants with electrons and nucleons, as proposed in [74]. The effects are proportional to Z^2 and would manifest as a nonlinearity in the isotope shift of the clock transition, requiring a candidate system with enough isotopes to accurately detect the nonlinearity. Ytterbium is a good choice of system for this experiment, as there are 7 stable isotopes that are naturally abundant, and ytterbium also has a higher mass than most other optical clock candidates, meaning the expected nonlinearity is larger. This experiment is not trivial and requires precise theory calculations, which are generally difficult due to the large amount of electron-electron interactions found in singly ionised ytterbium. Another complication to this experiment is the Zeeman structure of the isotopes of ytterbium, which results in a non trivial clock operation.

CHAPTER 3

Ion traps

In this section, the trapping of charged atomic ions is discussed. The aim of this is to provide a general background into how ion traps work and are implemented at NPL, as well as provide the theory that will be needed later to understand certain systematic frequency shifts. Much of the treatment and background will follow the review article by Leibfried, Blatt, Monroe & Wineland[75]. For more detailed derivations, deeper background, and generally more information about the different quantum states one can generate in ion traps, the reader is directed to that review article and references therein.

3.1. Trapping charges with electric fields

Ions have a net electric charge, thus electric fields can be used to trap them. An electric potential must obey the Laplace condition,

$$\nabla^2 \Phi = 0. \tag{3.1}$$

As a result of this, a static electric potential cannot trap in all directions simultaneously. It is possible however to create a time varying field that can trap charged particles in a dynamic way that still satisfies the Laplace condition. The potential takes the form,

$$\begin{aligned}\Phi(x,y,z,t) = &\frac{U_{dc}}{2}\left(\alpha x^2 + \beta y^2 + \gamma z^2\right) \\ &+ \frac{U_{ac}}{2}\cos(\Omega t)\left(\alpha' x^2 + \beta' y^2 + \gamma' z^2\right),\end{aligned} \tag{3.2}$$

where U is the potential applied to the electrodes, and the $\{\alpha \dots \gamma'\}$ factors describe how the applied potential affects each degree of freedom. In order to satisfy the Laplace condition, $\alpha + \beta + \gamma = 0$ and $\alpha' + \beta' + \gamma' = 0$.

By carefully balancing the voltage and frequency of the trap drive with the charge-to-mass ratio of the ion, a stable situation occurs where a time averaged trapping potential is formed. This phenomenon, that allows an unstable potential to become stable via an oscillation is a family of problems described by the Mathieu equation. It leads to some counter-intuitive phenomena, such as upside down pendula.The equation of motion of the ion is given by the Mathieu equation,

$$\frac{d^2x}{d\tau^2} + [a_x - 2q_x\cos(2\tau)]x = 0, \tag{3.3}$$

where,

$$\tau = \frac{\Omega t}{2}, \qquad a_x = \frac{4|e|U_{dc}\epsilon}{mr_0^2\Omega^2}, \qquad q_x = \frac{2|e|U_{ac}\epsilon'}{mr_0^2\Omega^2} \tag{3.4}$$

where Ω is the angular frequency of the oscillating potential, t is time, U is the electric potential, ϵ is a geometric term that governs how the fields applied to the electrodes are experienced by the ion, m is the ion mass, e is the electron charge and we have assumed the ion is singly positively charged, and r_0 the distance between the ion and the electrode. The parameters a_i and q_i are known as trapping parameters, and govern whether the trap is stable or unstable. q governs the dynamic part of the trap and a the static part. In general the trapping parameters for each spatial direction are independent. The stability in a particular direction, i, is described to lowest order by,

$$\beta_i = \sqrt{a_i + \frac{q_i^2}{2}}, \tag{3.5}$$

and the trap is stable if $0 \leq \beta_{x,y,z} \leq 1$. The displacement of the ion is then given by,

$$x(t) = 2A\cos\left(\beta_x\frac{\Omega}{2}t\right)\left(1 - \frac{q_x}{2}\cos(\Omega t)\right), \tag{3.6}$$

where A is determined by the thermal energy of the ion. The motion is harmonic about the centre of the trap, but comprises 2 frequency components. There is a driven motion at the trap drive frequency, Ω, and a slower motion a factor of $\beta_i/2$ slower than the driven motion. The fast, driven motion has a smaller amplitude than the slow motion, for this reason it is dubbed micromotion. The slower motion is generally called secular motion, and expressed with the lower case omega: $\omega_i = \beta_i\Omega/2$.

In general the ytterbium ion traps at NPL are operated with $a_{x,y,z} = 0$ and $2q_{x,y} = q_z < 0.4$, this ensures that the trap operates safely within the region of stability.

3.1.1. Micromotion minimisation

Stray electric fields, such as those caused by charge build up or patch potentials which are a natural consequence of operating the trap, will cause a displacement of the ion from trap centre. Equation 3.6 is only strictly valid when the ion is centred around the true RF minimum of the trap (trap centre). Away from trap centre a driven motion at the trap drive frequency is introduced to equation 3.6, leading to a term proportional to the mean displacement, $\bar{x}$, and oscillating at Ω,

$$x(t) = 2A\cos\left(\beta_x\frac{\Omega}{2}t\right)\left(1 - \frac{q_x}{2}\cos(\Omega t)\right) + \bar{x}\left(\frac{q_x}{2}\cos(\Omega t) + 1\right). \tag{3.7}$$

This is termed excess micromotion, and is fundamentally different from the micromotion in equation 3.6 which is at a frequency $|\Omega \pm \omega|$ called intrinsic micromotion. As the ion gets further away from the trap centre, it experiences more of the RF field, and as such the excess micromotion has an amplitude proportional to the average displacement from trap centre, as opposed to the intrinsic micromotion, whose amplitude is dependent on the amplitude of the secular motion. This driven motion can be very large, causing a systematic shift from both the electric field and second order Doppler effects. When the excess micromotion is too large, it also has a detrimental effect on the ion, changing the cooling transition line shape etc. and as such it is vital that it is minimised.

Micromotion can be detected a couple of ways. If a camera is used to image the ion, increasing the trap depth will move the ion towards the null. This method is quite useful for initially finding the micromotion null, but is not sensitive enough to null the micromotion for precision spectroscopy. For this

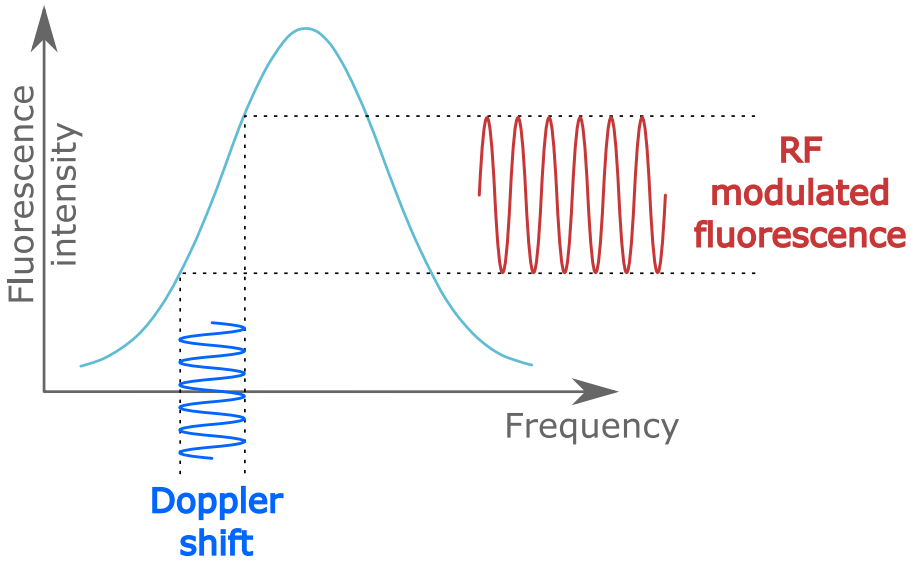

Figure 3.1: The micromotion causes a driven motion of the ion at the trap drive frequency, which in turn causes a modulation of the Doppler shift of the cooling laser. By red detuning the cooling laser by $\Gamma/2$ we can use the cooling transition as a frequency discriminator, causing a modulation of the detected fluorescence at the trap drive frequency.

we use the RF-photon correlation technique, shown in figure 3.1. The driven motion of the ion causes a Doppler shift of the cooling laser, this creates a modulation of the light scattered by the ion at Ω. The RF trap drive is used to trigger a time to amplitude converter (TAC)[1], and the PMT is used to stop the TAC when a photon arrives. By acquiring the TAC signal for 15-60 seconds (depending on the size of the ion signal), we build up a picture of how many photons the ion is scattering as a function of the phase of the RF trap drive. Any micromotion results in a driven motion of the ion, which results in a Doppler shift of the cooling laser, and thus a modulation of number of photons scattered by the ion, as shown in figure 3.1. A fast Fourier transform (FFT) is then performed on the fluorescence data to acquire the modulation depth at the trap drive frequency Ω. The modulation depth tells us how large of a correction to make, and the phase tells us the sign of the correction. The modulation depth, M can be related to the mean ion displacement $\bar{x}$ by,

$$\bar{x} = \frac{M\Gamma\lambda}{4\sqrt{2}\pi\omega_x}, \tag{3.8}$$

obtained using the relations from chapters 2 and 7 of [10],

$$\bar{x} = \frac{v_{max}}{\sqrt{2}\omega_x}, \tag{3.9a}$$

$$v_{max} = c\frac{M\Gamma}{2\nu_{369}} = \frac{M\Gamma\lambda}{4\pi}, \tag{3.9b}$$

where v_{max} is the peak ion velocity and ν_{369} the frequency of the cooling transition used to detect the micromotion. The ion's displacement can then be corrected by applying static electric fields via compensation electrodes.

3.1.2. Ion motional heating rate

The trapping potential is well described as a quantum harmonic oscillator, with a large number of energy levels separated by $\hbar\omega_i$. The temperature of the ion then determines the average energy level, $\langle n\rangle$, of the ion. If we have a radially symmetric trap with secular frequencies of $\omega_r = 2\pi \times 1\,\text{MHz}$, and a Doppler cooling limit of 0.5 mK (typical operating conditions for the NPL Yb^+ traps), this gives an average energy level of $\langle n\rangle \approx 10$. Because of the strong coupling of the ion to electric fields, any electric field noise near the motional frequencies

[1]Model: Ortec 566 TAC

can result in the ion gaining motional quanta and thus being heated. The rate at which quanta are gained by a trapped ion can be used as a sensitive tool to measure the electric field noise [76], and can limit the fidelity of multi qubit gate operations and the accuracy and stability of an atomic clock by introducing a dephasing mechanism and a 2nd order Doppler shift. In general there are 3 parameters of the trap determine the electric field noise at the ion: the secular frequency of the ion ω, the ion electrode distance d, and the temperature of the trap electrodes, T . There have been a number of experimental investigations into this, and a good review is given by Brownnutt [76], Starting from the ansatz for the electric field noise experienced by the ion, S_E, the scaling is measured to be

$$S_E \propto \omega^{-1} d^{-2\cdots-4} T^{+0.54\cdots+2.13}. \tag{3.10}$$

The large discrepancy between reported scaling is due to complicated nature of these effects.

For high precision spectroscopy, we want a small heating rate, as changes to n will change the Rabi frequency of the clock transition, and will also change the velocity of the ion, causing a 2nd order Doppler shift. A large heating rate will decrease the contrast of longer clock pulses, and can significantly change the systematic shifts from the start to the end of a pulse as the ion heats up, creating a challenging evaluation of the systematic shifts.

By altering the drive frequency, size and temperature of the trap, we can reduce the heating rate at the expense of altering the trapping potential - from equation 3.4 we see that changes in Ω quadratically reduces the trap depth and changes in d linearly reduce trap depth. Since d scales the heating rate much more favourably than changes in Ω^2 and has a smaller impact on trap depth, creating a larger trap is more favourable, though Ω is a simpler experimental parameter to change. Significantly changing T is challenging and normally reserved for ions that require cryogenics for other reasons.

The ions motion is a 'thermal state': rather than occupying a single phonon level $|n\rangle$, the ion has a probability of occupying each phonon level. Since temperature is an ensemble effect, the state is described by a density matrix,

$$\rho_{nn} = P_n |n\rangle\langle n|, \tag{3.11}$$

where the coefficients P_n are described by the normalised Boltzmann factors,

[2]For certain ions Ω is set to a 'magic' frequency that cancels micromotion induced shifts. There is no such cancellation for Yb^+.

$$P_i = \frac{\exp\left(-\frac{n_i+1/2}{\langle n\rangle+1/2}\right)}{\sum_j \exp\left(-\frac{n_j+1/2}{\langle n\rangle+1/2}\right)}, \tag{3.12}$$

where $\langle n\rangle$ is the average phonon level at current temperature, T, and is given by,

$$\frac{1}{2}k_B T = \hbar\omega\left(\langle n\rangle + 1/2\right). \tag{3.13}$$

The heating rate describes how $\langle n\rangle$ increases over time, and can be different for each motional degree of freedom of the ion.

The phonon heating rate can be measured in a few different ways. We first used the Doppler recooling technique[77], where the ion is left without cooling for a period of time, and then the fluorescence recovery is measured as the ion is recooled, allowing the ion temperature after the heating period to be inferred. We also measured the heating rate by looking at the dephasing of Rabi flops on the E3 transition after allowing the ion to heat up for a short period of time. These techniques will be discussed in more detail in section 3.3.3. The more common method of heating rate measurements, where the motional quantum number, $\langle n\rangle$, is measured by looking at the imbalance of the secular sidebands of the clock transition has not been used due to our clock lasers not having enough power to drive very quick π-pulses on the secular sidebands.

3.1.3. Ion trap geometry

In order to realise an ideal trap, the RF electrode surfaces need to be at equipotentials of ideal parabolic trapping potential curve, if not then there are higher order terms added to the potential that can cause a trapping instability or other undesirable effects. The traditional design of a Paul trap involved having 2 hyperbolic electrodes and a ring electrode, in order to satisfy the equipotential condition. In practice, the anharmonicity is not significant if the electrodes are small and the ion is cold and confined close to the centre of the trap. One such trap design that takes advantage of this is the Schrama end cap trap design [78], where the hyperbolic end cap electrodes are replaced by small cylindrical electrodes, and the ring electrode is split in 2, with each half wrapped around the RF electrode and held at ground. The major advantage of this trap geometry is the much larger optical access allowed by removing the ring electrode.

3.2. Single ions

Ion traps are suitable for isolating individual ions, giving the experimenter access to a single, well isolated quantum system. Multiple ions can also be trapped, and can exist in different phases, such as a hot gas like cloud (plasma), or a cold structured crystal. Multiple ions in a crystal are suitable for QIP type experiments, and also for ion clocks where there is no suitable cooling transition [79], or simply increasing the signal to noise ratio. As ytterbium has a readily accessible cooling transition, we can avoid the extra complications of a multiple ion crystal and use a single ion.

Determining how many ions are in the trap is a simple process that can be done in a number of ways. The first is to look at the quantum jumps, where a discrete fluorescence level is observed for each ion in the trap (this is discussed in more detail in section 3.2.1). Another method is to examine the behaviour of the cooling transition as the detuning is changed. Multiple ions can exist in numerous phases, and changes between these phases occur as the cooling laser and trap parameters are altered. The most characteristic phase transition is from a hot cloud phase to a cold crystal phase. As the cooling laser is taken from a far detuned state towards the resonance this phase transition produces a characteristic spike in the fluorescence, as the ions scatter more photons, get cold and then form an ordered phase with a much lower Doppler broadening. This phase transition is absent for a single ion. The final method is to image the ions with a CCD, where the strong Coulomb repulsion between ions, $\sim 10\,\mu$m apart and makes them spatially resolvable, see for example the images of 1 and 2 ions in figure 3.2a. It is possible to isolate a single ion from a trapped cloud/crystal by ejecting the other ions from the trap, but generally the loading parameters of the trap are optimised such that a single ion is loaded with high fidelity, generally on the first or second loading attempt. Once a single ion has been trapped, the micromotion is minimised and cooling parameters optimised such that we can begin clock operation.

3.2.1. Detection of internal state

To determine the internal state of the ion, we employ the method of quantum jumps. By continuously monitoring the fluorescence of the E1 369 nm transition, any successful attempt to drive the ion to a metastable 'clock' state results in the ion being shelved in that state - it can no longer scatter 369nm light. This results

in a sudden drop in the ion fluorescence, with two discrete levels being measured, see figure 3.2a. Since the ion signal can be in excess of a few thousand counts per second, and the dark counts are less than 100 per second, this method allows for very high fidelity read-out with very short detection times. This method can also be used to count the number of ions in the trap. If we have, for example, 2 ions in the trap, there is a probability that both will be bright, one will be bright and one dark, or both dark. This results in 3 distinct signal levels, one for each ion and a background level. As the number of ions gets large this method can become difficult as our imaging and probing setup is designed specifically for single ions, as well as the trap being optimised only for single ions.

3.3. NPL ion traps

All of the ion traps used in the Yb^+ clock at NPL are based on the end cap geometry. As part of a European collaboration, the Czech Metrology Institute (CMI) performed a thermal analysis of our traps (as well as those used by PTB and QUEST) [80], using both experimental measurements and numerical modelling, to calculate the thermal environment experienced by the ion, and thus help us to evaluate the BBR shift, part of which is shown in figure 3.6. The resulting publication also gave design tips to help other researchers design ion traps suitable for high precision metrology [80]. In this section I shall describe the designs of ion traps used in this thesis. We have recently introduced an updated design of end cap trap, which has been designed to have an optimum thermal performance. In addition to this there have been other performance gains by optimising the vacuum chamber geometry and the optics, resulting in a much better trap that is much lighter and smaller. These changes will be expanded on in this section, and contrasted with the more traditional designs of the older traps. This will partly overlap with the collaborative work with CMI, but there are other quality of life improvements that have been made to make the operation of the traps easier and better.

3.3.1. Traps 1 & 2

Traps 1 & 2 are the oldest traps in the lab, dating from the mid-late 90s. The design is heavily based on the original Schrama end cap trap [78]. The electrodes are made from tantalum with an alumina insulator to separate the RF electrodes from the DC electrodes. The separation between the RF electrodes is 560 μm.

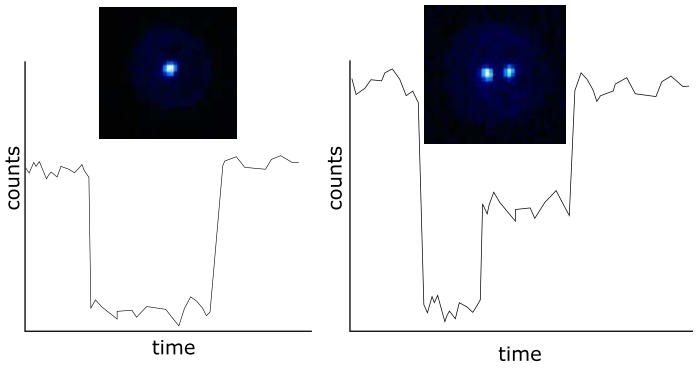

(a) Image showing the state detection of a single ion and a 2 ion crystal. A background level of PMT counts is observed when all ions are dark. A much high, distinct level is observed for each ion that is in the trap. Fluorescence data in this figure is simulated, but the images of the ions were taken in trap 3.

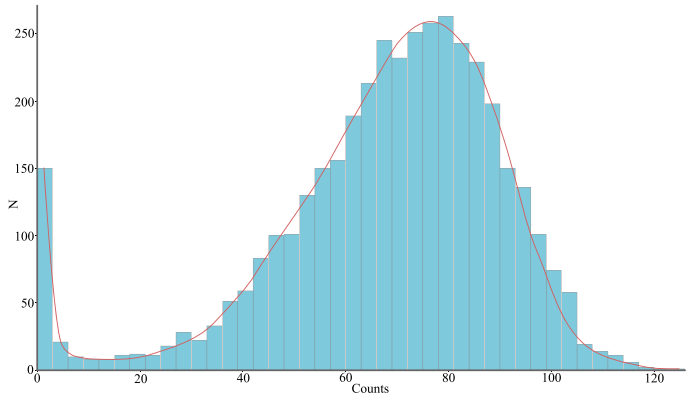

(b) Single ion quantum jump histogram. Red line is to guide the eye.

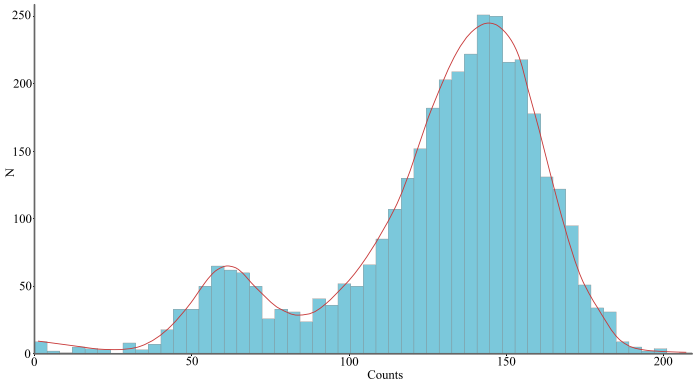

(c) 2 ion crystal quantum jump histogram. Red line is to guide the eye.

Figure 3.2: Detection of single ions versus multiple ions.

A schematic diagram and image of the vacuum chamber design is shown in figure 3.3. The vacuum chamber is based on a cube, and as such there is limited optical access. There are 3 pairs of windows that give optical access, each pair has an AR coated window and a Brewster window. Generally the AR window is used as the entrance port, though the IR beams enter through a Brewster window. The use of Brewster windows limits access to the transmitted beam if the polarisation of the beam isn't matched to the Brewster window. Ideally the 3 beams would be mutually orthogonal, allowing for unambiguous determination of micromotion in each axis with zero crosstalk between each beam and control electrode, and optimum polarisation spinning of the cooling beams. This isn't possible with the vacuum chamber used, instead the up and the down beam have a 45 degree angle between them. For the horizontal beam, the blue (369, 399, 436 and 467) light enters from one window, and the red (760 and 935) light enters from the other, so the beams counter propagate. Since the red beams enter through a Brewster cut window, this limits how well the ion can be repumped in certain magnetic fields.

Because of the large steel chamber the imaging system doesn't have the best possible numerical aperture. A x10 telescope is used to image the ion onto a photomultiplier tube (PMT). In general a signal of about 900 counts.s^{-1} on a background of 100 counts.s^{-1} is observed, using polarisation spinning on the up and down beams in a $10\,\mu$T magnetic field. The large steel chamber also limits how quickly the magnetic field coils can be switched between fields, and how quickly a cooling bias field can be applied, meaning that polarisation spinning must be used, which slightly lowers the signal from the ion.

The RF source for the trap drive is a synthesiser, generally running at about 13 MHz. This signal is amplified by about 30dB, and then stepped up in voltage through a resonant toroidal transformer. The peak voltage on these traps is about 400V, which results in radial secular frequencies of ~ 1 MHz. The resonant transformer is connected to the feedthrough via a coaxial cable, and then the feedthrough is a generic DC feedthrough. This setup has a not insignificant capacitance which results in a sizeable loss of RF power and heating of the trap electrodes. Since none of the windows can transmit the mid IR thermal radiation quantifying exactly the temperature of the trap is not easy. CMI modelled and measured the temperature of a test trap when mounted on its feedthrough and driven at operating power.

Micromotion compensation is provided by the outer DC endcaps, and 2 horizontal electrodes. The horizontal electrodes are not orthogonal, and they

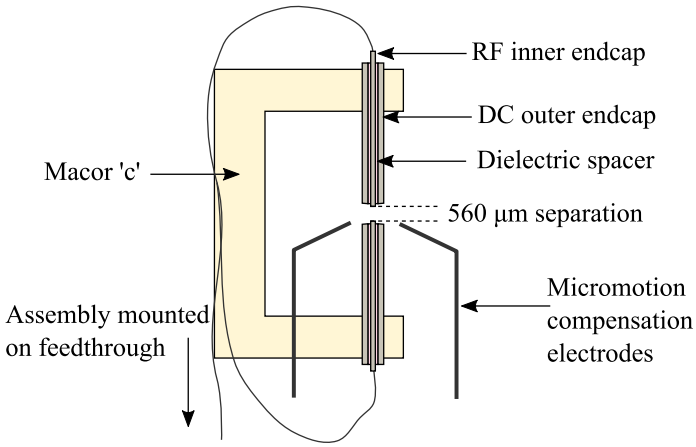

(a) Schematic of the trap 1 and 2 assemblies. The entire assembly is mounted onto a multi-pin electric feed through that is used for both DC and RF signals.

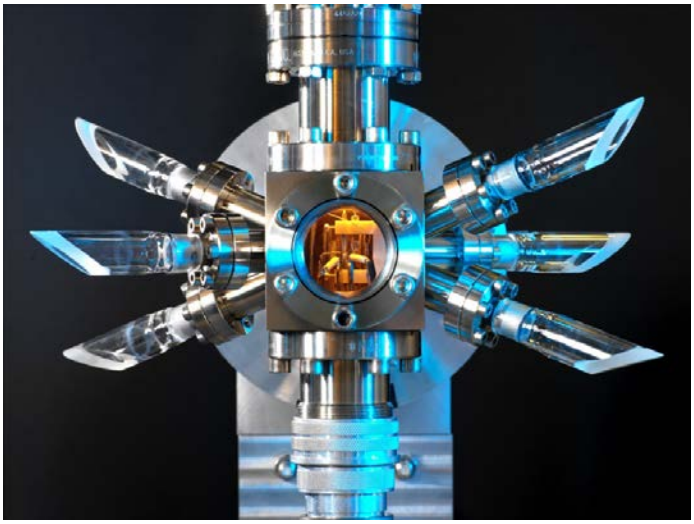

(b) Image of an NPL endcap trap vacuum chamber. Note the limited optical access from the windows. Note this particular trap is an Sr^+ , but the geometry of the trap and vacuum chamber is identical. Reproduced from [81].

Figure 3.3: Image and schematic view of the NPL Schrama style endcap traps.

are not orthogonal to the beams used to detect micromotion in the 2 horizontal directions. This means that there is significant cross talk between the two directions. Also of note is that there is a small vertical micromotion in trap one that cannot be compensated. This has been blamed on a slight path length

imbalance between the upper and lower RF electrodes. The resultant phase mismatch causes a driven motion of the ion at the RF drive frequency.

3.3.2. Trap 3

The main purpose of the trap 3 design was to minimise trap heating, improve the knowledge of the thermal environment, and to allow the atomic polarisability in the mid IR to be measured. Figures 3.4a & 3.4b show a schematic of the design and layout of trap 3. The main way to lower the trap heating is to reduce the amount of dielectric between the RF and any DC. The RF endcaps have been changed from tantalum dowels mounted in a Macor 'c' holder to molybdenum pins mounted in a copper 'c' holder. The copper 'c' is mounted directly to a dedicated RF vacuum feed through. This ensures that there is less dielectric heating in the feedthrough and ensures a much better phase matching of the RF endcaps. The DC electrodes are mounted on fused silica horse shoe blocks on the flat arms of the copper c. This allow for a much greater separation of the RF and DC and ensures a low volume of dielectric; this minimises the RF heating of the trap structure. Another important aspect is that the bulk of the trap is copper, which has excellent electrical and thermal properties for this task. Modelling of the temperature change of the trap during operation was performed by CMI [80], with experimental input from measurements performed on the real trap, shown in figure 3.6. The trap performs a lot worse in real life than the modelling suggests, partly because of losses in the feedthrough and helical resonator heating the structure and partly due to the surface roughness of the trap components preventing any heat build up from conducting effectively, which was not taken into account in the model. A heat sink bar made from AlN was constructed and added between the ceramic of the RF feedthrough and the breadboard on which the trap was mounted (shown in figure 3.5b); a new helical resonator constructed , which has no dielectric support of the resonator coil and operates at a slightly lower resonant frequency, to reduce losses and lower the power requirement of the trap, and the trap operated at a lower trap depth (see figure 3.6b), all in an attempt to minimise trap heating.

A custom vacuum chamber machined from aluminium, with indium sealed windows houses the trap. The chamber is only 24 mm thick, and the windows are 35 mm in diameter, giving much greater optical access and allowing the imaging optics a much larger numerical aperture (NA$\approx$ 0.43) than the previous traps, as shown in figure 3.4b. In addition to this, the small aluminium chamber allows

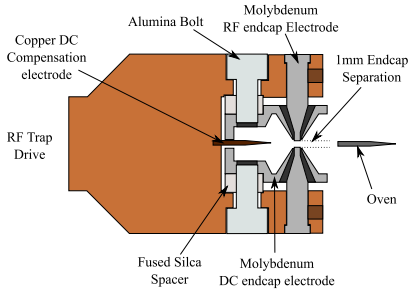

(a) Schematic of trap 3's trap electrodes

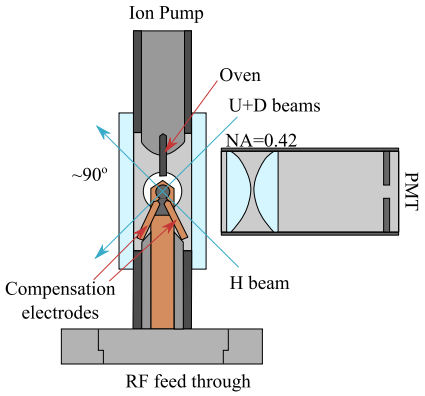

(b) Overhead schematic of trap 3's physics package, showing the impressive optical access.

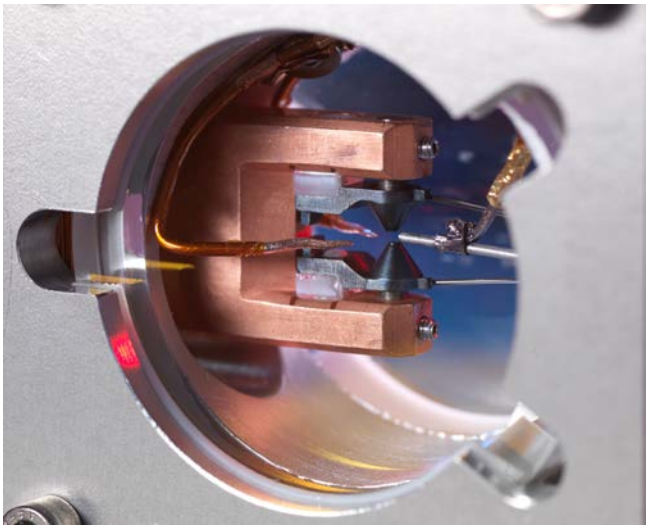

(c) Photograph of the trap 3 assembly. Visible is the trap, the compensation electrodes and oven. Note the notches in the window mount to allow entry of the laser beams at the desired angle.

Figure 3.4: Schematic views of trap 3

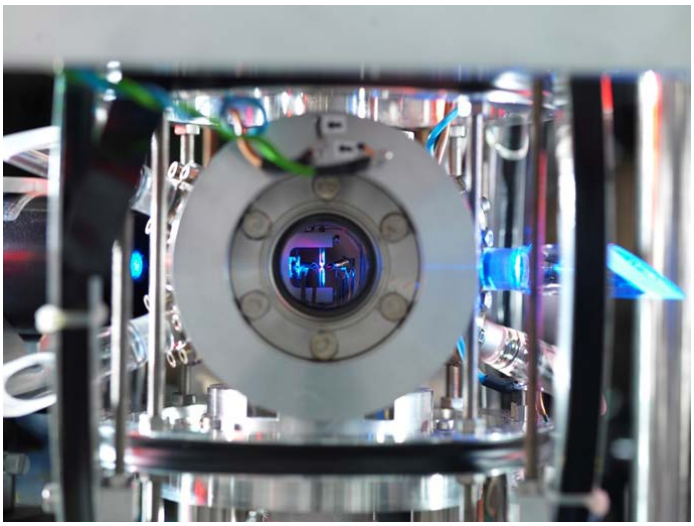

(a) Trap 2's vacuum chamber, trap structure and magnetic compensation coils. In this image the 467 nm light is entering from the central AR coated window on the left and leaving from the central Brewster window on the right.

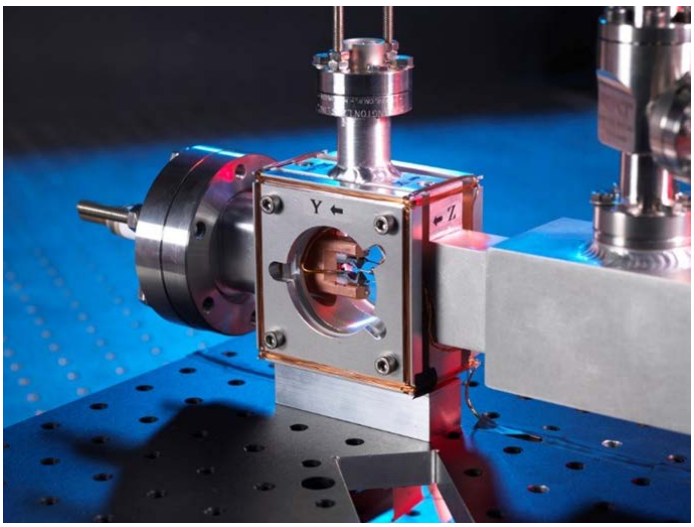

(b) Trap 3's vacuum chamber, trap structure and magnetic compensation coils, which are wrapped directly around the chamber. The thin design of the chamber allows 2 large windows to be placed close to the trap, giving improved optical access and larger NA when compared to the trap 1 and 2 design. Note trap 3 has a dedicated RF feed through (rear) and separate DC feed through (top).

Figure 3.5: Comparison images of the design of trap 2's and trap 3's vacuum chambers and compensation coils, highlighting important differences that improve the performance of trap 3.

for magnetic field coils to be placed closer, have fewer turns, and therefore switch much quicker than in the older traps. This means that a large bias magnetic field can be switched on for cooling and state detection, and be switched off for spectroscopy without having to wait an unacceptable length of time for the fields to decay or ramp up. A comparison of the design of the chambers and magnetic coils for the older traps and trap 3 is included in figure 3.5

The horizontal beam delivers all of the light necessary for operation to the trap, despite spanning a wavelength range of 369 nm to 935 nm. This is made possible by using an endlessly single mode fibre from NKT and a pair of Thorlabs parabolic mirrors to provide achromatic focusing of the beams, achieving a beam waist of about 5 μm on the 467 nm light resulting in intensities $> 1\,\mathrm{kW/cm^2}$ at the typical operating powers of 1 to 5 mW for the E3 clock pulse. Prior to the fibre input, the beams are combined using a combination of polarisation optics and dichroics. The input coupling collimator lens to the fibre is optimised for 369 nm light. The up and down beams allow for all 3 degrees of freedom of the ion to be explicitly addressed by a cooling laser and for the operation of polarisation spinning, with the up beam having spun polarisation. They are exclusively 369 nm beams, and have a much larger spot size of about 100 μm with up to 10 μW of power available for these beams. Fluorescence is detected by a nominally 3:1 imaging telescope and a PMT, with a 400 nm knife edge Semrock filter in the imaging setup to remove spurious light. The setup can yield a peak count rate of about 10000 counts.s^{-1} with a background of < 100 counts.s^{-1}. The SNR is much better than trap 1 and 2's due to the much tighter focussed horizontal 369 nm beam, $\sim 10\mu$ m, and larger trap structure, resulting in less scattered light, and the larger NA of the imaging optics achieving a greater collection efficiency. The RF endcaps are polished to a mirror finish in order to minimise point charge sources and lower the ion motional heating rate. In order to further lower the heating rate, the end cap separation has been almost doubled to 1 mm. From equation 3.10 heating rate scales as $\Delta n[\mathrm{quanta.s^{-1}}] \propto d^{-2\cdots-4}$. Therefore the increased size alone should improve the heating rate by a factor of 4 to 16 when compared to traps 1 and 2. Trap 3 has had its heating rate measured using a Doppler recooling technique [82] and by looking at the contrast of Rabi flops on the E3 transition. The combination of large ion-electrode separation, highly polished electrode surfaces and quiet compensation voltage enables us to achieve an impressive heating rate as measured by both the Doppler recooling method and dephasing of Rabi flopping.

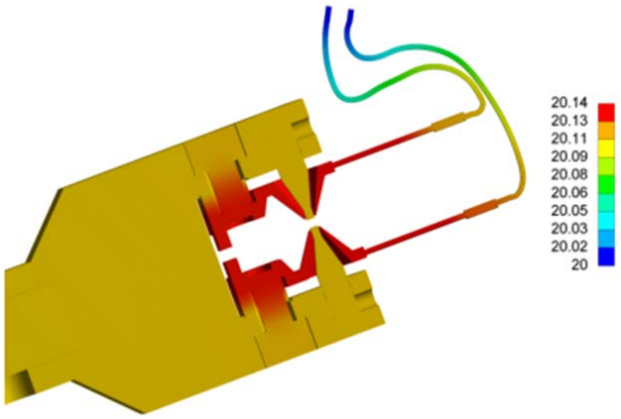

(a) Thermal model of RF heating in trap 3 created by CMI [80]. The design of trap 3 exhibits exceptionally low heating compared to most other ion trap designs.

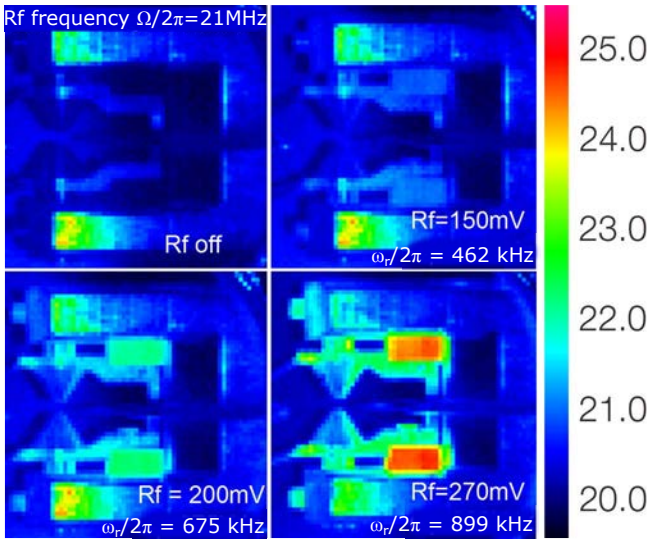

(b) Heating of trap 3 measure with a FLIR thermal camera. The quantity of interest is the temperature of the fused silica spacers, since they are of a reasonably well known emissivity. The RF voltage is the output of the synthesiser prior to amplification and the helical resonator, and the resultant secular frequencies are also quoted. The excess heating compared to the thermal model is a result of losses in the feedthrough and imperfect surfaces of the components degrading heat sinking.

Figure 3.6: Simulated and measured temperature changes of trap 3's structure.

3.3.3. Phonon heating rate measurements

Doppler recooling is a well established technique for measuring heating rates in ion traps [77]. The technique relies on time resolved measurement of the ion's fluorescence when exposed to the cooling laser after a dark period of time where the ion is allowed to under go heating. The heating of the ion induces a Doppler shift of the cooling laser, Δ_D, changing the effective detuning, $\Delta_{eff} = \Delta + \Delta_D$. This results in a reduced photon scattering rate, dN/dt, when the hot ion is first subjected to the cooling laser. As the ion scatters photons, it is cooled, reducing the Doppler shift and allowing more photons to be scattered. This is seen as a rise in the number of photons recorded by the PMT. Larger heating rates result in the ion getting hotter during the dark period, and thus a larger reduction in scattering rate and longer recovery time to the steady state. Mathematically, the average scattering rate of an ion with scaled thermal energy $\bar{\varepsilon}$ at a scaled time τ is given by [82],

$$\left\langle \frac{dN}{d\tau} \right\rangle_{\bar{\varepsilon}} = \int_0^\infty P(\varepsilon') \left. \frac{dN}{d\tau} \right|_{\varepsilon = \Xi(\varepsilon' \tau)} d\varepsilon'. \tag{3.14}$$

where energy, E has been scaled by the power broadened scattering rate

$$\varepsilon = \frac{2E}{\hbar\Gamma\sqrt{1+s}}, \tag{3.15}$$

where s is the saturation parameter $s = I/I_{\text{sat}}$, and time, t, has been scaled by the on resonance power broadened scattering rate,

$$\tau = \frac{t\Gamma s/2}{1+s}. \tag{3.16}$$

$\Xi(\varepsilon, \tau)$ is a propgation function that gives the energy at time τ of an ion that has energy ε at time $\tau = 0$, and $P(\varepsilon')$ is the Boltzman factor for the ion with scaled energy ε analogous to equation 3.11.

Due to the use of very short binning of the fluorescence data and low number of collected phtons per bin, the recooling must be averaged over many experimental runs to build an accurate picture. This technique is not suitable for very low heating rates, as the dark times required to resolve the recooling quickly become excessively long, for example figure 3.8a shows recooling measurements from trap 3, where the recooling feature is almost unresolvable after 60 s of heating. This technique is sensitive to changes in both the intensity of the cooling

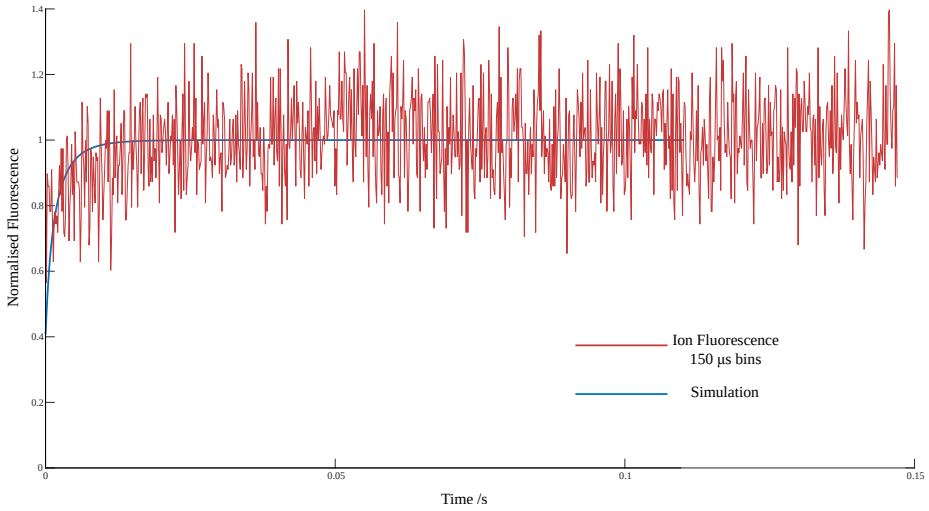

Figure 3.7: Red: Ion flourescence from trap 1 after a 50s heating time, with the cooling laser at I_{sat} and 5 MHz red detuned. Blue: Simulation with the ion starting at $\langle n \rangle = 150\,000$ and the laser with the same parameters as the experimental data.

laser and the detuning of the cooling laser. Whilst taking heating measurements in trap 1, it became apparent that the technique is highly sensitive to the excess micromotion of the ion due to the complicated dynamics of Doppler cooling in the presence of micromotion [82]. For accurate measurements it was vital the micormotion was minimised and stable for the duration of the measurement. Figure 3.7 shows an example recooling measurement in trap 1, taken 5 MHz detuned at I_{sat} with a 50 second block time. The simulated data shows the fluorescence from an ion with $\langle n \rangle = 150\,000$, which corresponds to a heating rate of $3000\,\text{quanta.s}^{-1}$ given the 50 second block time. Note over the course of this measurement the cooling laser drifted slightly more red detuned and so the deduced heating rate is a slight underestimate. The sensitivity of Doppler recooling proved to be too low to adequately work for trap 3's low heating rate - long heating times lead to measurements taking many hours to gather adequate statistics which risks losing control of the experimental parameters, such as a laser becoming unlocked or losing the ion etc.

The ion's motion state is described by the density matrix given in equation 3.11. As the ion's average phonon level $\langle n \rangle$ increases, the population of the density matrix element ρ_{nn} is also changed in accordance with the Boltzmann factors in equation 3.12. This means a hot ion not only has more average

motional energy $\langle n \rangle$, but its density matrix has significant population across a larger distribution of motional energy levels n. Increasing the vibrational quantum number of the ion weakens its coupling to the probe laser and thus reduces its Rabi frequency. The Rabi frequency, Ω_n, of an ion in the n^{th} motional energy level is given by[75, 10],

$$\Omega_n = \Omega_0 \exp\left(\frac{-\eta^2}{2}\right) L_n\left(\eta^2\right), \tag{3.17}$$

where Ω_0 is the Rabi frequency for $n = 0$, η the Lamb-Dicke parameter of the ion and L_n the Laguerre polynomial of rank n. Here we have only considered transitions that leave the motion quantum number, n, unchanged. When we consider this effect in relation to an ion with a temperature described by the density matrix in equation 3.11, we are required to average over all possible vibrational energy levels n, weighted by their probability of occupancy, P_n. This results in a dephasing of the Rabi oscillation with increasing $\langle n \rangle$,

$$|c_1(t)|^2 = \frac{1}{2}\left(1 - \sum_n P_n \cos\left(\Omega_n t\right)\right), \tag{3.18}$$

where c_1 is the excited state amplitude. Rabi oscillations were measured on the E3 transition after allowing the ion to heat for 10 ms to 500 ms. This was done by altering the preprobe delay already built into the experimental cycle that is typically kept at 10 ms. For each oscillation a best fit value of $\langle n \rangle$ was computed to minimise the χ^2 value of the model. The heating rate could then be estimate from calculated $\langle n \rangle$ and the corresponding wait times.

Figure 3.8a shows trap 3's Doppler recooling trace, taken at $\delta = 5\,\text{MHz}$ and $I = I_{sat}$. There is no significant sign of an increase in fluorescence, which would be expected if the ion was getting hot. The detected heating rate is 50^{+100}_{-50} quanta per second, limited by the trap control software time resolution. By using the dephasing technique, we can achieve a higher sensitivity, shown in figure 3.8b. This method has a greater sensitivity, giving a heating rate of 24^{+30}_{-24} quanta per second, which is consistent with the Doppler recooling, though neither method is sensitive enough to accurately measure the heating rate. In order to improve the sensitivity further, we plan to measure the heating rate by looking at changes in the imbalance of the motional sidebands of the E2 transition.

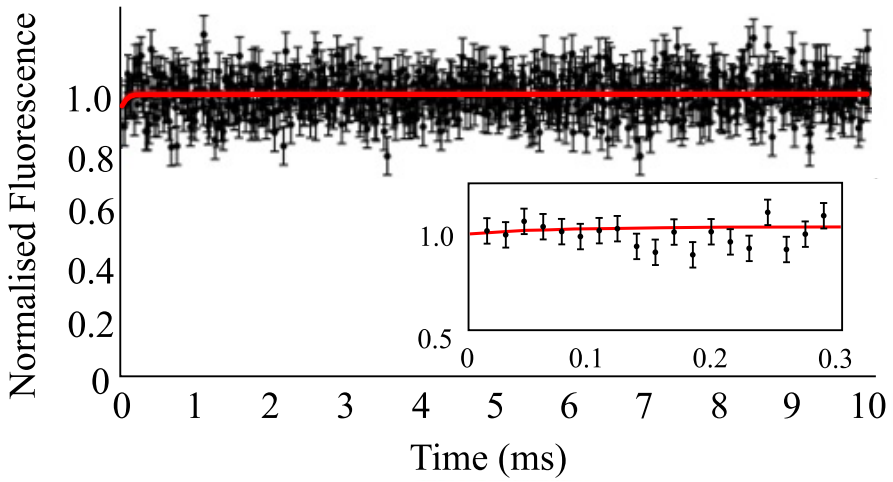

(a) Doppler recooling profile taken in trap 3, showing fluorescence recovery after cooling has been blocked for 60 seconds. This data gives a heating rate of $d\langle n\rangle/dt = 50^{+100}_{-50}\,\mathrm{s}^{-1}$. The recovery of the fluorescence occurs in a very short period of time, yielding a heating rate limited by the sensitivity of the measurement.

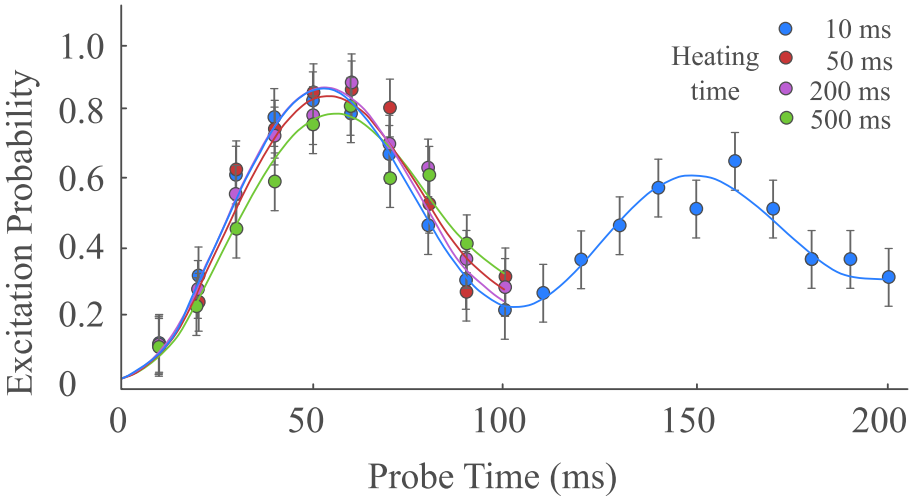

(b) Rabi flopping measurement of the heating rate. No significant changes to the Rabi frequency or excitation amplitude can be observed for heating times of up to 500ms prior to the clock pulse. Analysis of this method gives a heating rate of $d\langle n\rangle/dt = 24^{+30}_{-24}\,\mathrm{s}^{-1}$

Figure 3.8: Data traces from the measurement of trap 3's phonon heating rate using both the Doppler recooling method 3.8a and thermal dephasing method 3.8b.

3.3.4. Computer controlled micromotion voltage compensation supply

In order to minimise the micromotion of the ion, there are 4 DC electrodes inside the vacuum chamber which provide electric fields that can be used to null any stray fields that are displacing the ion from the centre of the trap. 2 of the electrodes are the outer endcaps, which form a pair that deals with vertical motion, and then there are 2 horizontal electrodes that are nearly orthogonal to each other that deal with micromotion in the horizontal plane. The voltages applied to the electrodes can vary from less than 1 V to over 100 V in typical operating conditions. Supplying quiet, stable and repeatable voltages is essential for good performance of the trap and a low systematic error budget.

In order to improve the performance of trap 3 further, new compensation voltage supplies were designed. Previously a number of different designs had been used that all shared one feature - a high voltage was divided down with a potentiometer to produce the compensation voltage. This is undesirable due to a manually controlled knob required to set a desired voltage level. To allow for automation of the minimisation process, a computer controlled design was implemented, which involved a DAC and high voltage amplifier and upgraded filters. An image of the output section of the PCB is shown in figure 3.10b.

The Design uses an AD5764 DAC, which is a 4 channel 16-bit DAC with an output range of ± 10 V and programmed over SPI. The computer interface was handled by an Arduino Uno running a C program to interface with the DAC. The DAC output is amplified with an Apex PA443 HV amplifier, set with a gain of 14, and powered by some Recom DC-DC converters set to give ± 150 V. For situations where a low voltage is required, such as the endcaps, each channel can bypass the amplifier and output straight from the DAC. The system as a whole easily fits onto a standard Eurocard PCB. The downside with this small system is the use of digital electronics and DC-DC converters, all of which can add extra noise to the output, and tend to do so at similar frequencies to the motional frequencies of the ion, for example a DC-DC converter may switch at 300kHz, which is a plausible secular frequency for an Yb^+. To remove this noise, which can cause heating of the ion, a separate PCB was designed that would filter the voltages immediately before the vacuum chamber, to remove any additional voltage noise picked up during transmission to the trap. A schematic of the filter is shown in figure 3.9a, and a complete circuit diagram is included in figure 3.11. These filters use surface mount components, rather than leaded components, which significantly lowers the self-inductance of the components that hinders

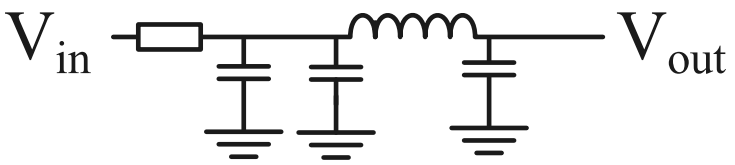

(a) Schematic of the DC filtering of the micromotion compensation voltages.

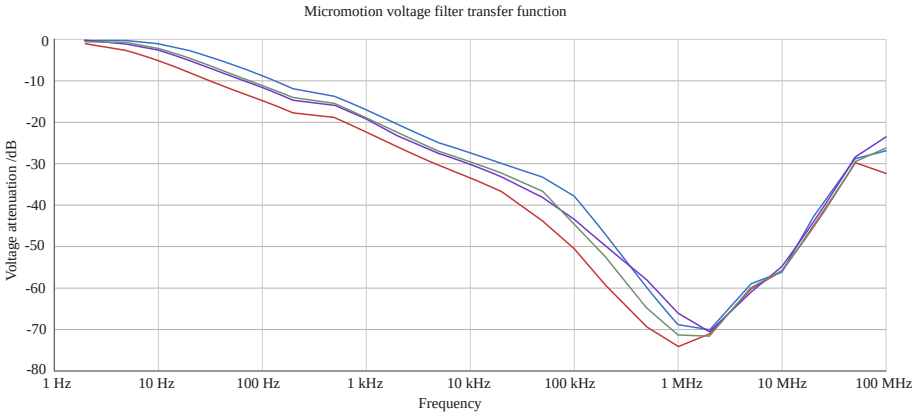

(b) Graph of the transfer function of a 4 channel filter assembly based on SMD, low self-inductance components. Note how we see the second order of the filter kick in at about 100kHz, and how the self-inductance of the components leads to a decrease in performance past a few MHz. The optimum performance is at about 1MHz, which is our preferred secular frequency for a trapped ion.

Figure 3.9: Compensation voltage filters.

performance of filters in the 1MHz frequency region, which is generally where our ion's secular frequency is! The capacitors used have a special package where the contacts are on the long edge of the capacitor, as opposed to the more usual short edge, which lowers their self-inductance even further. The performance of these filters is shown in figure 3.9b. At frequencies higher than 1MHz, the small self inductance of the components starts to degrade the performance of the filter.

The Labview software used to measure the micromotion of the ion has been extended to communicate with the voltage supplies, allowing for a more automated nulling of the micromotion. The process is not fully automated yet due to requiring additional shutters to allow for individual control of the up, down and horizontal 369 nm beams.

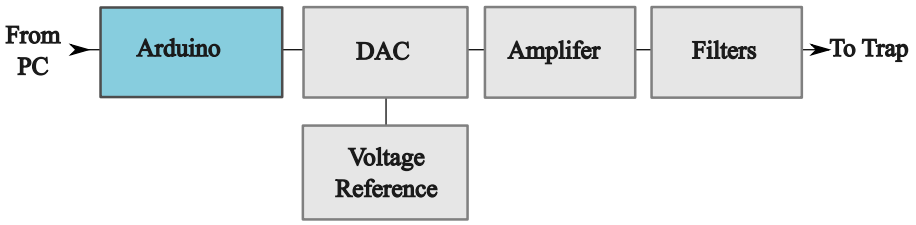

(a) Block diagram of the computer controlled voltage supply.

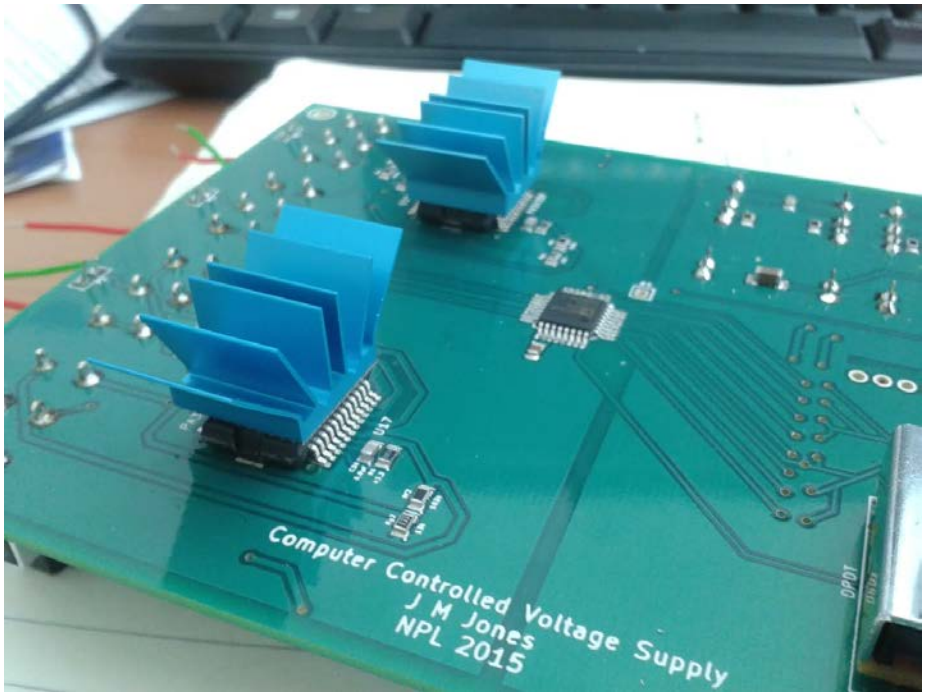

(b) Voltage supply PCB, the 4 Channel DAC is the small square chip in the centre of the board. The high voltage amplifiers are shown with blue heat sinks attached. DC-DC converters attach to the underside of the board on the right hand side, in an attempt to provide a little bit of shielding to the analogue outputs.

Figure 3.10: Compensation voltage supply board.

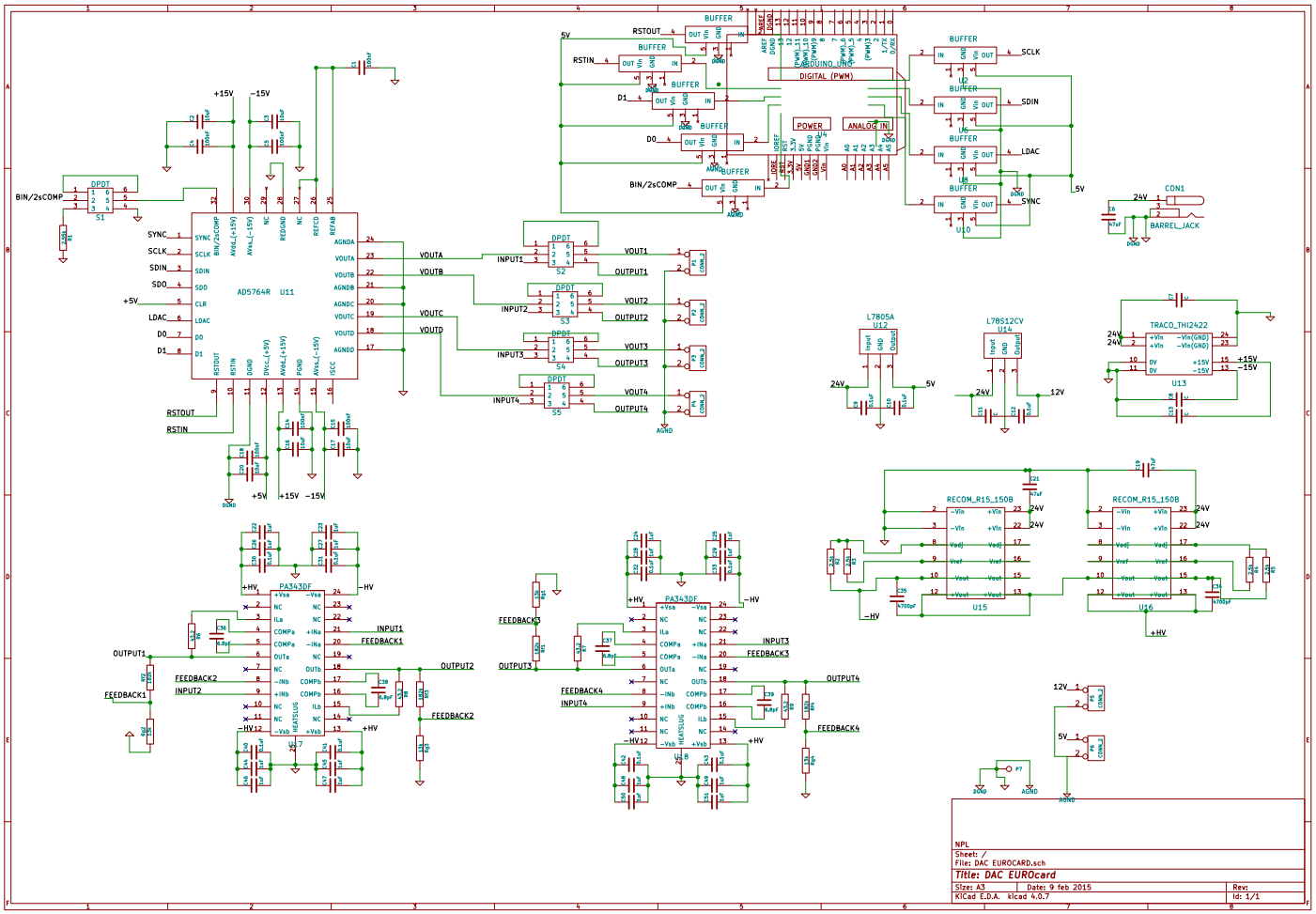

Figure 3.11: Complete circuit diagram of the 4 channel micromotion voltage supply developed for trap 1 & 3.

An improved version of this board has been designed, with lower noise DACs and voltage sources being used, an active and passive filter section, in addition to having two additional channels. This board is intended for use in an improved version of trap 3 that is also being constructed. This has 6 electrodes for micromotion nulling - 3 opposing pairs, which should allow for a better nulling of the electric field gradient at the ion. In addition to this the trap has a better design of RF feed through, which should dramatically lower heating of the trap structure, and a new vacuum chamber, designed to be placed in a 3 layer mu metal shield. This should not only improve the systematic error budget but make operation of the clock a much simpler and automated process.

CHAPTER 4

Laser systems and experimental control

This chapter describes the laser systems used to cool and prepare the ion. On the whole, the setup is very similar to when it was last described in the thesis of Steven King in 2012[10], however there have been a couple of changes to the 369 nm, 935 nm and 760 nm set-ups, as well as a new 934 nm optical cavity and the ability to lock to the universal synthesiser. The Pound-Drever-Hall (PDH) locking scheme [83] is used extensively in this experiment, predominantly but not limited to, locking the clock lasers to high finesse cavities. This is a standard but non-trivial technique that has extensive literature coverage, for example the excellent paper by Black [84] that gives a comprehensive introduction to PDH locking.

Since the laser systems are nearly identical to the prior work, the author's main contribution in this area was the upkeep and maintainence of the laser systems. The major permanent changes made were upgrading the 369 nm DLpro to a more powerful diode and swapping the cavity the 935 nm laser was locked to due to a vacuum pump failure.

4.1. Laser systems

Ytterbium ion clocks require quite a wide range of wavelengths, from 369 nm to 935 nm. With advances in semiconductor technology and photonic crystals, all of the wavelengths can be made using diode lasers and waveguide frequency doublers. All of the lasers are based on the extended cavity diode laser (ECDL) principle, whether home built or commercial, apart from the 760nm laser, which is based on a DFB design.

4.1.1. Ionisation, cooling & repumping

The ions are created by photoionisation of the neutral atom. The first stage to photonionisation is to drive the 399 nm transition in the neutral ion. From here any photon shorter than 392 nm will ionise the ytterbium. This is accomplished by either a 369 nm photon, or a 399 nm photon plus the large electric field of the ion trap. The 399 nm laser is a home built grating stabilised ECDL. The diode is a direct 399 nm source made by Nichia.

The 369 nm laser used for cooling is a Toptica DL Pro with a 369 nm diode made by Nichia. The laser is split into numerous beam paths as shown in figure 4.1. One path is sent to an NPL low drift etalon for stabilisation. The low drift etalon is a Fabry-Perot cavity with re-entrant mirrors mounted on piezos to allow the cavity length to be tuned (see [85] for the product specifications). The cavity is 10 cm long with a spacer made from ultra low expansion glass (ULE) in a temperature controlled enclosure. The laser is locked to this reference using a side of fringe lock, as this means no frequency modulation is required on the laser. The voltage reference for the side of fringe lock is derived from a pick off of the light sent to the cavity, meaning the lock point in insensitive to changes in the laser power. The light at the cavity is ~ 200 MHz red detuned from the main cooling transition $^2\mathrm{S}_{1/2}\mathrm{F}= 1 \rightarrow ^2\mathrm{P}_{1/2}\mathrm{F}' = 0$.

To repump the F=0 ground state of the cooling transition, the light used for cooling has 14.7 GHz sidebands added using an EOM in a phase modulation set-up. The EOM runs at half the sideband frequency, and the 2nd order sidebands are used to perform the repumping. This light is then frequency shifted by double passing through a +110 MHz AOM and split to create up, down and horizontal beams at the ion. The AOM provides quick shuttering and precise frequency control, and gives access to the 0^{th} order beam, which is combined with the up beam and used as a far (220 MHz) detuned beam to improve the

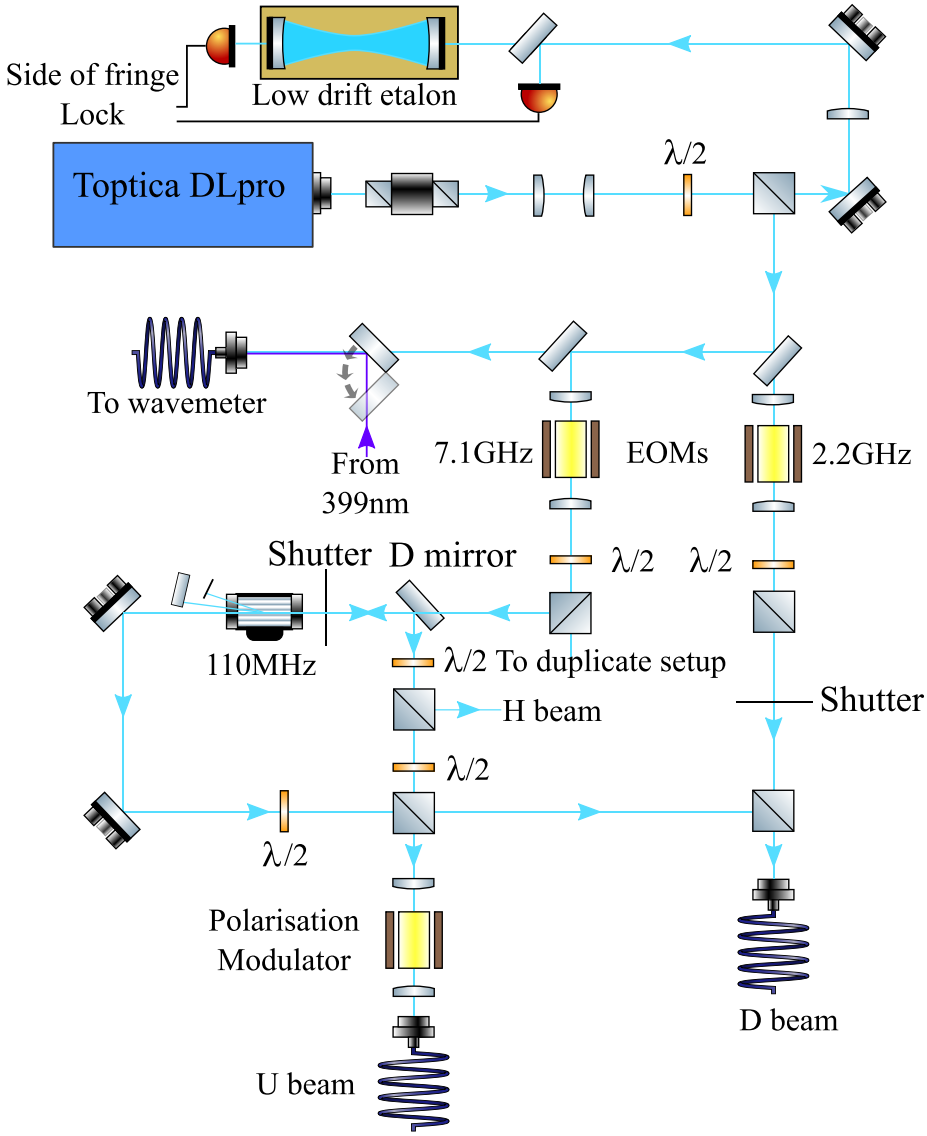

Figure 4.1: Schematic of the 369 nm laser set up. The schematic has been slightly simplified by removing some steering mirrors, compressing the setup and removing repeated assemblies for each trap.

cooling efficiency of hot ions. This can be useful during loading or after a large collision with background gas. The up beam is the 'spun' beam during polarisation spinning. It passes through an EOM, set up as a polarisation modulator, and shifts between $\pm\pi$ at 1.4 MHz. A second 369 nm beam with

2 GHz sidebands is used to pump the ion into the F=0 ground state for state preparation prior to spectroscopy. This light is locked to the cavity but not sent through the AOM, meaning it is 220 MHz red detuned, but still effectively pumps the ion into the ground state.

The 935 nm laser is a Newport Vortex ECDL, as shown in figure 4.2. It is locked to a low drift etalon using the Pound-Drever-Hall technique. The transmission of the cavity is used to repump the $^2D_{3/2}(F = 1)$, so that the cavity acts as a frequency filter to remove the ASE pedestal from the 935 nm laser, which could otherwise depopulate the F=2 hyperfine state that is used as the clock state for the E2 transition, which would prevent using the electron shelving technique. During cooling, however, it is desirable to repump the $^2D_{3/2}$F= 2 state as well and so a portion off the 935 nm light is picked of and 3.06 GHz sidebands added to address both hyperfine levels.

The 760 nm laser is used to depopulate the $^2F_{7/2}$ state. The F=3 hyperfine level is the clock state of the E3 467 nm transition. The repumping transition is dipole forbidden, and thus requires both high power and good frequency stability. The laser used is a DFB laser. The frequency dift is low enough that it is left free running, with a manual tuning of the current every few days to compensate for drift. Approximately 5 mW of power is incident onto the ion. There are 2 DFB lasers, which can be used such that each one repumps one hyperfine state. Alternatively, only one laser may be used and the current stepped periodically to repump the F=3 state most of the time and only occasionally the F=4 state, since the rate of population of the F=4 state is only a couple of times a day. Figure 4.2 shows a schematic of the single 760 nm laser setup, note how the use of a DFB laser greatly simplifies the setup compared to other systems. The stability of these lasers is such that they require no locking and only an occasional manual tuning of the wavelength, which is optimised by minimising the time taken to repump the F=3 state.

4.1.2. Clock lasers

In order to excite the highly forbidden clock transition, an ultra stable laser is required. These lasers have a line width of 1 Hz or less, and are fractionally stable to 1×10^{-15} or better at time scales of a few seconds. In order to achieve this, a standard laser is locked to an optical cavity - two highly reflective mirrors that allow for a build up of a standing wave of light. This acts as a frequency reference for the light, allowing a servo to accurately stabilise and narrow the

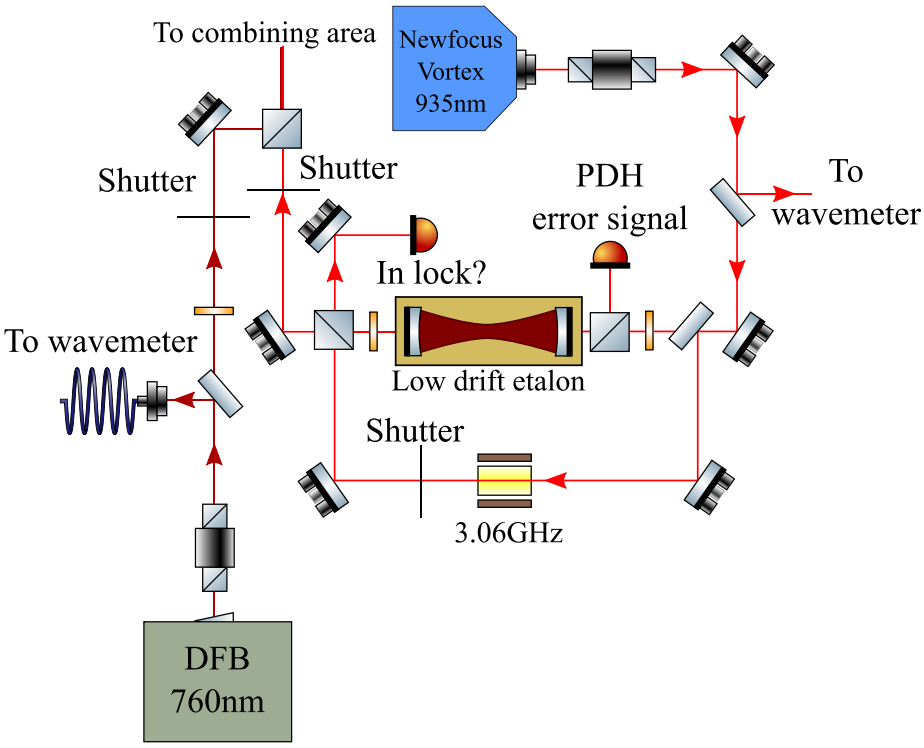

Figure 4.2: Schematic of the 935nm and 760nm laser set up. The schematic has been slightly simplified by removing some steering mirrors, compressing the setup and removing repeated assemblies for each trap.

laser. We shall first discuss the laser setups and then move on to the cavities.

The 467 nm light begins as 934 nm before being frequency doubled. Due to the extreme narrowness of the E3 transition, a large amount of power is required to achieve adequate spectral density to drive the transition. The 934 nm laser is a Toptica TA Pro, which combines an ECDL with a tapered amplifier to provide 500 mW of optical power. A small portion of the light is used to lock the laser to a 10 cm high finesse ($\mathcal{F} \approx 150\,000$) ultra stable cavity, which narrows the laser from a few hundred kHz to 1 Hz. The majority of the light is coupled to a fibre which delivers it to an NEL waveguide doubler. The doubler has a collimated free space output, after which a dichroic beam splitter is used to separate the doubled 467 nm light from the remaining 934 nm light.

The remaining 934 nm light, about 80 mW, is coupled to a fibre that distributes the light to the two combs labs and the 30 cm long 934 nm high finesse cavity.

Each combs lab and the long 934 nm cavity have an AOM at the far end of the fibre to cancel any phase noise introduced in the fibre, using the technique described in [86] and shown in figure 5.7, where a small portion of the diffracted light is retroreflected back down the fibre and interfered with some of the unshifted light in a Michelson style interferometer. Any phase noise introduced by the fibre causes the beat note between the 2 interferometer arms to deviate from twice the nominal AOM driving frequency. Mixing the beat note with twice the nominal AOM frequency generates an error signal, which corrects the AOM frequency to remove the fibre induced noise. The long cavity AOM runs at about 110 MHz to bridge the frequency difference between the laser and the cavity. The 2 combs labs have AOMs running at 82 and 80 MHz. A small portion of light after these remote AOMs is retroreflected, and combined with a reference beam in our lab to generate three beat notes, each at twice the relevant AOM's nominal frequency. The separation of these frequencies is sufficient that simple filters can be used to isolate each beat note. The phase noise for each fibre link can then be independently removed, actuating on the remote AOMs.

The 467 nm light, of which there is 30 mW, is distributed to the traps. A low drive power 125 MHz AOM is used to shift the frequency to the resonance of the ion. The passive short term power stability of the light is limited by the power stability of the AOM RF amplifier. In order to provide improved short term stability and prevent long term drifts, the power in the beam is servoed to a predetermined value during operation. This is achieved by mixing in the servo feedback with the AOM RF signal using a double balanced mixer (DBM) in reverse. One might be worried that this would introduce phase noise to the signal, however when using a mixer in this way it acts solely as an amplitude modulator. The creation and monitoring of this servo is described in more detail in chapter 6.1.

Historically the 467nm light was made using a resonant doubling cavity located on the active vibration isolation (AVI) platform inside the laser and ultra stable cavity box. The cavity was in a bow-tie configuration, with the length of the cavity stabilised using a piezo actuated mirror, locked using the Hänsch-Couillaud method [87]. The bandwidth of the servo was limited to < 14 kHz to avoid resonances of the piezo mirror. This produced > 15 mW of blue light. After this the light was fibred into the blue combining area. The doubling cavity lock was a common source of failure of the clock, either due to the servo running out of range or some spurious noise causing the servo to rail. Apart from this, the performance of the doubling cavity was adequate,

with short term power stability at the ion limited by the AOM RF amplifier power stability, and frequency stability sufficient to drive 100 ms π-pulses with contrast in excess of 90%. In order to drive 2 traps at the same time using hyper-Ramsey, which requires much shorter π-pulses, the cavity was replaced with a waveguide doubler, which provides in excess of 30 mW of blue power in the blue combining area.

The 871nm setup is much the same as the 934nm set-up, except that there is no tapered amplifier, as the E2 transition requires a very small amount of power to drive very short π pulses. Historically the light was created using a single pass of a doubling crystal, but now the setup has been upgraded to a waveguide doubler, allowing for more power. This will be necessary when driving very short π-pulses, such as when measuring the heating rate through the motional sideband imbalance.

Creating an ultra stable laser

As mentioned, ultra stable lasers are created by locking a standard laser to an optical cavity. This cavity exhibits a narrow resonance when the light forms a standing wave between the mirrors. The light can be locked to this narrow resonance, most commonly using the Pound-Drever-Hall technique, described further below.

An optical cavity consists of 2 mirrors that are facing each other, which creates an optical resonance when twice the separation of the mirrors is an integer number of the wavelength of the light. The Q factor of the resonator depends on the loss and absorption of the mirrors: creating a cavity with high reflectivity mirrors creates a high Q-factor resonator. The resonance of the cavity is periodic in frequency. This periodicity is called the free spectral range, FSR, and thus rather than a Q factor, the generally quoted figure of merit for a cavity is the finesse, $\mathcal{F}$[88],

$$\mathcal{F} = \frac{FSR}{FWHM} = \frac{\pi}{2\arcsin\left(\frac{1-\sqrt{\rho}}{2\sqrt[4]{\rho}}\right)} \approx \frac{2\pi}{1-\rho}, \tag{4.1}$$

$FWHM$ is the full width half maximum of the cavity, ρ is the fraction of the power remaining in the cavity after one round trip. Loss mechanisms include the reflectivity of the mirrors, scattering from the mirror surfaces, loss in any medium between the 2 mirrors etc. Modern high reflectivity mirrors have total loss approaching 1ppm, and as such can make very high finesse cavities. A high

finesse results in the light staying in the cavity for a long time, and as such the cavity stores the phase information of the light for a long time.

Because the resonance is determined by the optical path length between the two mirrors, this distance has to be controlled very precisely - fractional changes in length of the cavity map directly to fractional frequency changes of the light. The mirrors are optically contacted onto a spacer that determines the length of the cavity. Most materials change length with changes in temperature. This spacer is made from a low expansivity material that has a linear coefficient of thermal expansion (CTE) that has a zero crossing at a convenient temperature. All NPL cavity spacers are ultralow expansivity glass (ULE) which has a CTE zero crossing close to room temperature. The cavities are held under vacuum in a 2 layer temperature controlled heat shield and vacuum chamber. This provides effective isolation from temperature and pressure fluctuations. The cavity is carefully designed and mounted to minimise changes in length as a result of vibrations. To further mitigate vibration effects the cavity is mounted on a stable platform, either an active vibration isolation (AVI) or minusK platform.

Both of the 934 and 871 lasers are locked to an NPL design 10cm 'mushroom' cut out cavity, see figure 4.3 for an image of the cavity and figure 4.4 for a schematic of the setup. This design provides a low sensitivity to vibrations. The cavities are mounted on AVI legs and are located on the main experiment optical table. To further shield the cavities from the environment of the lab, a wooden box with lead lined foam and a water cooled heat exchange has been placed around these cavities. Due to the materials used and the length of these cavities, they have a noise floor of around 1×10^{-15}. This limits our coherence time to around 300 ms. A new cavity was constructed with a longer 30 cm spacer and fused silica mirrors, which have a lower thermal motion than ULE mirrors. This cavity has a theoretical noise floor of around 1.4×10^{-16}. The cavity resonance has a FWHM of about 1 kHz. By locking the prestabilised clock laser to this cavity, we can further narrow the line width of the laser, improve the coherence time and ultimately resolve narrower features and improve our clock stability and systematic error budget.

The Pound-Drever-Hall technique is used to derive the error signal to lock the laser[84]. Sidebands are added to the laser using a resonant Brewster cut EOM. The 934 nm laser is modulated at $\sim$ 10 MHz and the 871 nm laser is modulated at $\sim$ 2MHz. The reflected light from the cavity is incident on a photodiode, where the sidebands create a beat note with the carrier at the modulation frequency of the EOM. Changes in the laser frequency cause a phase shift of this

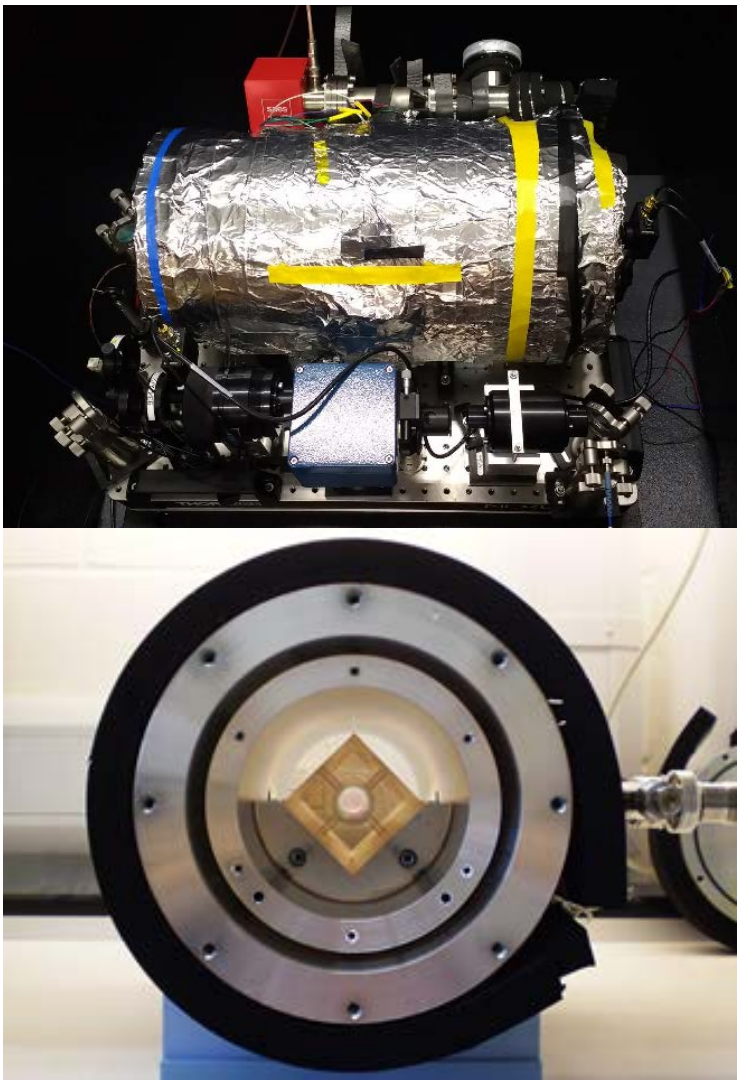

Figure 4.3: Images of the ytterbium ion clock cavities. The top image is the 934 nm 30cm cavity, see text for details. The bottom image is of the long cavity mounted in its vacuum chamber. The cavity is mounted on a cradle via 4 Viton balls. The cradle has spherical supports to isolate it from the inner heat shield. The inner heat shield rests on 4 fused silica balls to isolate it from the outer heatshield/vacuum chamber, which is temperature controlled via heated pads.

beat note relative to the RF source driving the EOM. By mixing these signals a dispersion-shaped DC error signal is created that can be used to lock and narrow the laser given a large enough feedback bandwidth. A Toptica FALC is used

to feedback to the laser current and piezo voltage, with a servo bandwidth of about 1 MHz for the 934 nm laser. A half waveplate before the EOM is used to precisely align the polarisation of the light with the crystal axis of the EOM by rotating the waveplate to minimise the error signal when the laser is far from the cavity resonance. This prevents polarising optics down stream from converting potential polarisation modulation into amplitude modulation. This is known as residual amplitude modulation (RAM), and since it occurs at the modulation frequency, it will appear as an error signal after the demodulation resulting in any small polarisation fluctuations being written onto the laser as frequency fluctuations. Optical isolators are placed in the beam path to prevent parasitic etalons from forming, which would also lead to spurious frequency corrections being written onto the laser.. The lasers lock to these cavities exhibit 1 Hz linewidths (see [10]).

The long cavity setup is shown in figure 4.3. The light is delivered to the long cavity via fibre. In order to cancel any phase noise in the fibre link a small additional optical bread board is mounted inside the acoustic isolation box that has an AOM that serves to bridge the gap between the laser and the cavity and as the phase noise cancellation actuator. The fibre that delivers light from the board to the minusK platform has an FC/PC connector that provides the retro reflection for the phase noise servo. In order to lower the power delivered to the cavity and provide some optical isolation from the fibre facet, the first optic is simply a glass slide, followed by an isolator. This helps to remove any parasitic etalons. The PDH sidebands are added with an EOM running at a ~ 2 MHz. Since the laser is prestabilised to the 10 cm cavity, a large lock bandwidth is not required. A high quality polariser is placed before the EOM to allow the polarisation of the light to be matched to the crystal axis of the EOM, which is necessary to remove RAM. Another isolator ensures there are no parasitic etalons formed by the EOM setup. The light is circularly polarised before 26 μW is sent to the cavity. The cavity transmission is monitored by a photodiode, this also acts as the error signal for the power stabilisation servo. Cavities exhibit shifts in resonant frequency as the power inside the cavity builds up and causes heating of the mirrors. To remove this, the photodiode signal is stabilised to a reference voltage by feeding back to the amplitude of the phase noise AOM driving signal.

In addition to these cavities, one of the frequency combs has its own stable laser locked to a 30 cm cavity of near identical design to our long 934 cavity. This cavity operates at 1064 nm, and by using the comb as a transfer oscillator,

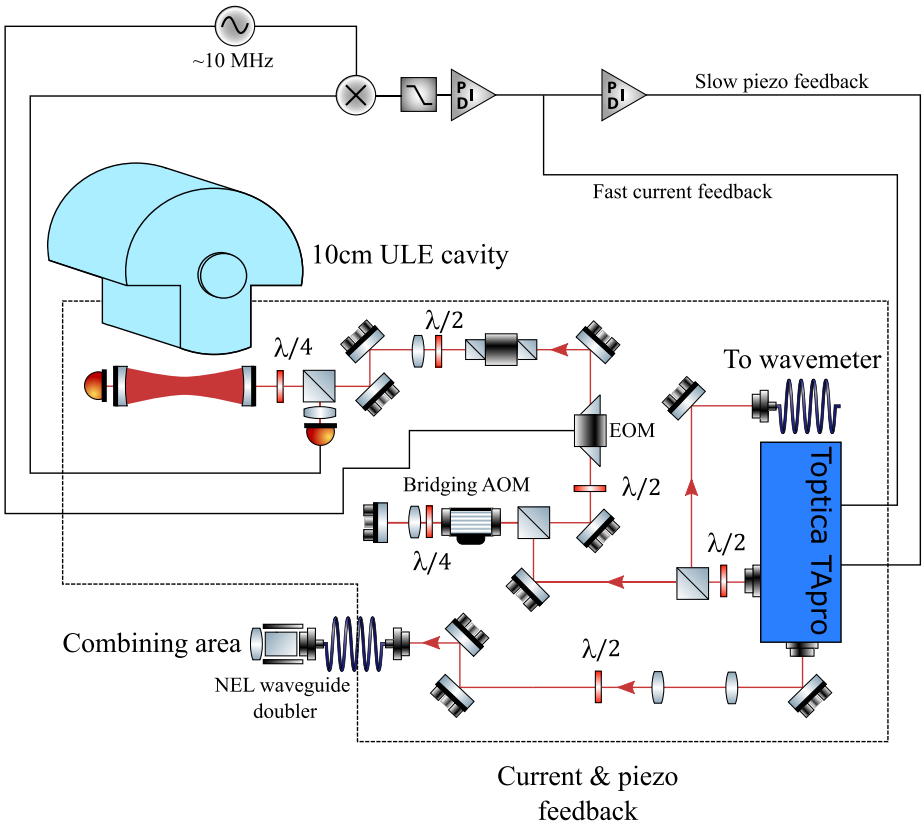

Figure 4.4: Typical clock laser setup, based on the 934 laser. Areas inside the dashed line are mounted on an AVI platform and inside an acoustic insulation box.

we can lock our clock lasers to it. Since the stability of the 1064 nm light can be transferred across the frequency comb to arbitrary frequencies, this set-up is referred to as a universal synthesiser.

4.1.3. Delivery to the trap

There are 3 beams present at the trap, the up, down and horizontal beams. The up and down beams contain only the 369 nm light, with the polarisation spun and state preparation light being delivered by the up beam, and the linearly polarised and far detuned light being delivered by the down beam. The horizontal beam is responsible for delivery of all the other lasers. The fibre for this purpose is an NKT endlessly single mode polarisation maintaining fibre, which

remains single mode for wavelengths between 200 nm and 2000 nm. The beam combining area is shown in figure 4.5. This figure also shows the waveguide doublers that generate the blue clock light, and the delivery to the combs and long cavity labs for the 934 nm light and the beat detection unit for the 3 phase noise cancellation set-ups.

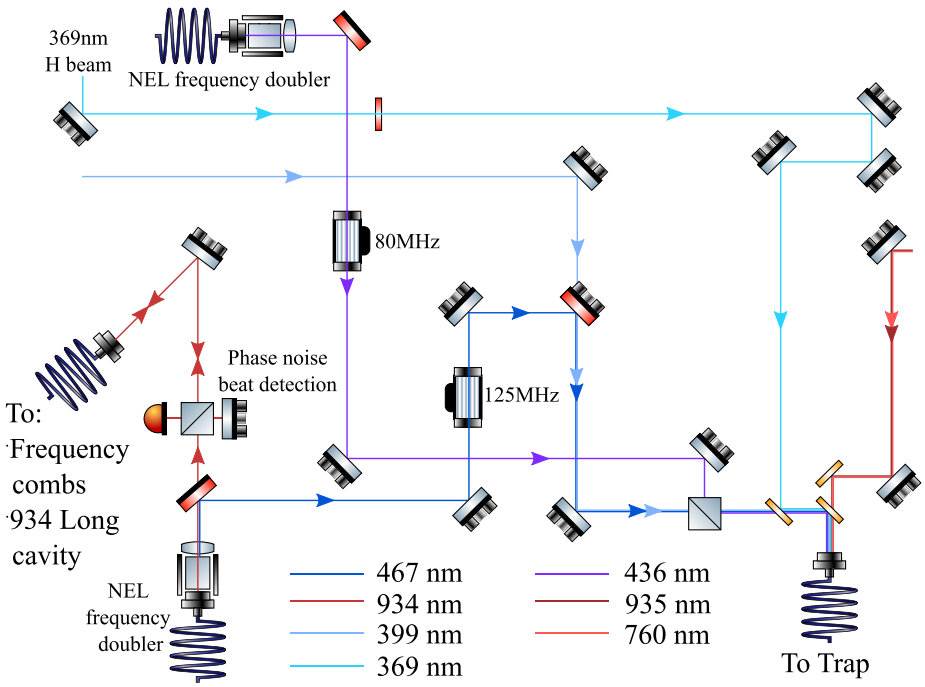

Figure 4.5: Beam combining area. All wavelengths from 369 nm to 935 nm are delivered to the trap using 1 endlessly single mode fibre. Also shown are the waveguide doublers and phase noise cancelation beat detection units. The final fibre to the trap is not path length stabilised, as it is a short fibre in a well controlled laboratory environment.

At the trap, the up and down beams are focussed to a spot size of around 100 μm at the ion using single aspheric lenses, with 2 μW to 10 μW of light in each beam. These beams are only used at high power for micromotion measurement, with low power during operation to cool the ion's vertical motion without introducing too much scatted light. The horizontal beam requires much more care, since we need a much smaller spot size to drive the very weak E3 transition effectively, and because the beam is highly polychromatic, and thus any chromatic aberrations could cause problems. Traps 1 and 2 solve this problem by using bespoke telescopes and counter propagating the red and blue beam

paths to significantly reduce tolerances on the optical setup. For trap 3, the light from the fibre is collimated and focussed using a parabolic mirror collimator and a parabolic mirror for final focusing. By using reflective optics, we significantly reduce the on axis chromatic aberration. These optics are mounted in a cage with a slip plate in order to ensure the optical axis of the 2 mirrors align, preventing the introduction of any off-axis aberrations. The setup is then aligned onto the ion using a 3 axis micrometer. The 467 nm light has a spot size of around 10 μm as measured on the ion, and a slight displacement of the spot centre can be observed for each of the lasers, as judged by the ion. This is probably due to slight off axis aberrations introduced by small misalignments of the parabolic mirrors. The alignment onto the ion is optimised for the 467 nm light by maximising the Stark shift of the E3 transition for a given amount of power in the probe beam. This has a slightly detrimental effect on the observed fluorescence from the ion.

4.2. Interface and control

Each laser beam is controlled with a mechanical shutter. In addition to this the 436 nm, 467 nm and 369 nm beams have an AOM in their beam path, with the 369 nm AOM being double passed. The drive for these AOMs is provided by DDS units with Minicircuits RF switches. This provides a good extinction of the laser beams when required. The RF switches and mechanical shutters are controlled by digital signals from an NI chassis attached to the experimental control computer running the Labview control software. To prevent power fluctuations of the 467 nm laser caused by thermal effects of the AOM, a mechanical shutter is also used, allowing the AOM to be used purely for pulse shaping. The mechanical shutter blocks the beam for the majority of the 'off' time, with the AOM being on, only turning off while the shutter opens or closes, providing very clean edges to the pulse of light.

There are 2 forms of mechanical shutters in operation: most are constructed from a relay with a scalpel blade spot welded to the moving arm of the relay. These relays are large and noisy, causing noticeable vibration of the optics table. The others are a newer design based on a piezo flexure arm with a blackened foil flag attached to the end designed by the strontium lattice clock team at NPL [89]. These shutters can provide very fast shutting times, however long term drifts in the piezo positioning mean they require regular optimisation. In both of these shutters, the knife edge is placed at the focus of a telescope to

provide fast and comprehensive extinction. The piezo shutter case has threads to accept aspheric lenses allowing for very compact telescopes compared to the mechanical shutters, where normal bulk optics are used. Recently we introduced Stanford Research System shutters to the experiment, since they have very large apertures, achieve a high degree of attenuation, and introduces negligible vibrations in operation. These shutters have proved to be much easier to align then either of the home built shutters, and provide similar shuttering times.

CHAPTER 5

Spectroscopy and clock operation

Once the ion has been trapped and cooled, we can begin the process of interrogating the clock transition and producing a clock output - light that is referenced and stabilised to the atomic transition. In this chapter, we shall discuss the excitation of dipole forbidden transition, high precision spectroscopy techniques, and the production and measurement of the output of an optical clock.

5.1. Electric Dipole forbidden transitions

When driving an atomic transition, a number of selection rules involving angular momentum, quantum numbers and parity conservation determine whether the transition may occur. The simplest and most well known selection rules are made under the approximation of light being a pure electric dipole: any transition between 2 states of opposite parity, with an angular momentum change of 0 or 1 unit is allowed, with all other transition being strongly supressed. Transitions of this nature are labelled E1. By considering higher order corrections to the wave function of the photon, some forbidden transition are allowed, though heavily supressed. The first order forbidden transition are magnetic dipole, M1, and electric quadrupole, E2, allow for transition between states of the same

Multipole	ΔJ	$\Delta\pi$
E1	0, ±1 $J = 0 \not\to J' = 0$	✓
M1	0, ±1 $J = 0 \not\to J' = 0$	✗
E2	0, ±1,±2 $J = 0 \not\to J' = 0, 1$	✗
E3	0, ±1, ±2, ±3 $J = 0; 1 \not\to J' = 0, 1, 2; 1$	✓

Table 5.1: Table comparing selection rules of various transitions [13]. Here $\Delta\pi$ indicates a change in atomic parity, and J the atomic spin.

parity and in the case of E2 transition allow for more angular momentum to be transferred. Caesium fountain clocks operate on an M1 transition on the hyperfine splitting of the ground state, and many trapped ion optical clocks operate on an E2 transition, like the ones found in Yb^+, Sr^+ and Hg^+. Electric octupole transitions, notated E3, are weaker still. These transitions allow for 3 units of angular momentum to be transferred to the ion. Currently the only E3 transition to have ever been driven is in the Yb^+ optical clock. Table 5.1 gives a brief summary of the selection rules.

In addition to these selection rules, there are geometric constraints that govern the strength of the observed transition. Certain combinations of magnetic field direction, probe beam propagation direction and probe beam polarisation excite the transition more effectively than others. For a weak transition such as the E3 this is vital, as reducing the line strength with poorly chosen experimental geometry quickly makes the transition require an impractical amount of power to excite. The geometric factor of the line strength is used to calculate the optimum magnetic field to operate the clock in. Of particular concern to us is the strength of the $\Delta m_F = 0$ E3 transition to the $F_{7/2}$ state, and transitions to the whole $m_F = 0, \pm1, \pm2$ manifold of the $D_{3/2}$ state, as the Zeeman splitting of this state is used to measure the magnetic field in the trap. The field (or set of 3 fields) chosen must balance these factors. A recent interest has also developed in the $\Delta m = \pm2$ components of the E3 transition, which will be discussed further in section 6.4. Below are the geometric factors for the line strength of transitions from the $^2S_{1/2}\,|F = 0, m_F = 0\rangle$ ground state to the Zeeman levels of the $^2F_{7/2}\,|F = 2, m_F = m\rangle$ state, where the magnetic quantum number, m, is listed as the subscript of the geometric line strength factor R_m,

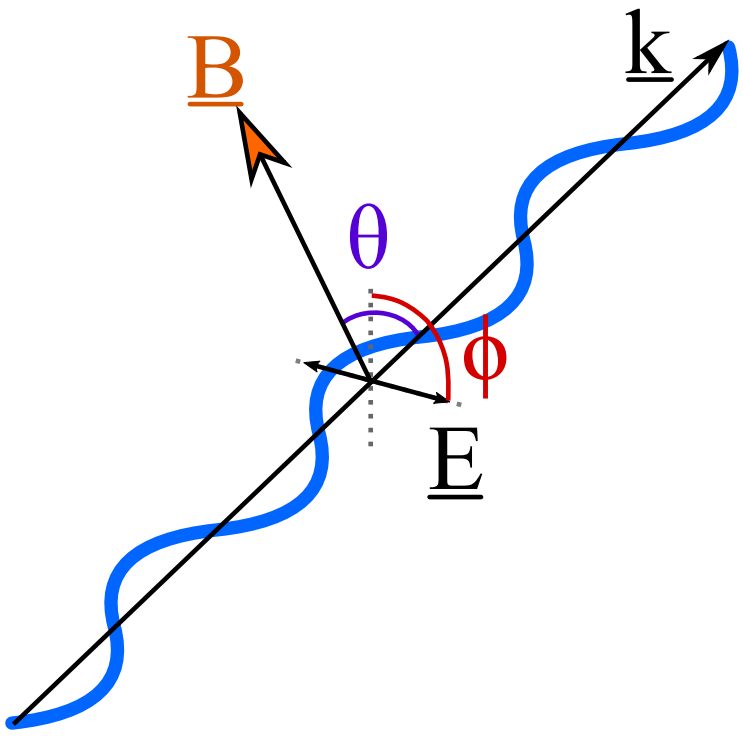

Figure 5.1: Diagram of the relevant quantities for calculating the line strength geometric factors.

$$R_0 = 12\sin^2\theta\cos^2\phi\,(1-5\cos^2\theta)^2, \tag{5.1}$$

$$R_{\pm1} = \cos^2\theta\cos^2\phi(11-15\cos^2\theta)^2 + \sin^2\phi(1-5\cos^2\theta)^2, \tag{5.2}$$

$$R_{\pm2} = 10\sin^2\theta\cos^2\phi(1-3\cos^2\theta)^2 + 40\sin^2\theta\cos^2\theta\sin^2\phi, \tag{5.3}$$

$$R_{\pm3} = 15\sin^4\theta(\cos^2\theta\cos^2\phi + \sin^2\phi), \tag{5.4}$$

where θ is the angle between the probe beam's propagation vector, $\vec{k}$, and the applied magnetic field, $\vec{B}$. ϕ is the angle between the light's $\vec{E}$ field vector and the plane of the probe beam and magnetic field, as shown in figure 5.1. A similar set of factors are for the E2 transitions between ${}^2\mathrm{S}_{1/2}\,|F=0, m_F=0\rangle$ and ${}^2\mathrm{D}_{3/2}\,|F=2, m_F=m\rangle$ are [90],

$$Q_0 = 6\sin^2\theta\cos^2\theta\cos^2\phi, \tag{5.5}$$

$$Q_{\pm1} = \cos^2\phi(\sin^2\theta-\cos^2\theta)^2 + \sin^2\phi\cos^2\theta, \tag{5.6}$$

$$Q_{\pm2} = \sin^2\theta(\cos^2\theta\cos^2\phi + \sin^2\phi). \tag{5.7}$$

In order for these geometric factors to be converted into linestrengths, they are multiplied by the relevant $3-j$ symbol. A key objective in the design of the experiment is allowing for 3 orthogonal fields that give a strong line strength for the E3 and a reasonable line strength for the E2, allowing us to average out any tensor shifts on the transitions (discussed in chapter 6.3.4). Optimisation is done by changing the magnetic field direction the clock operates in, as the probe beam and polarisation are not trivial to change. An interesting option for future operation would be to use multiple probe beams which would allow for a stronger E3 line strength with the magnetic field pointed in more directions.

5.2. Spectroscopic techniques

To excite the clock transition, the atomic sample is probed with a pulse of resonant, or near-resonant, light. The population transfer of a resonant pulse is determined by the length and electric field strength of the pulse. There are 3 spectroscopy sequences generally used in high precision frequency measurements: Rabi spectroscopy uses a single pulse of radiation to excite the clock transition. The Ramsey scheme, used in caesium fountains, is where 2 pulses are separated by a dark period. This creates an interference effect as the phase

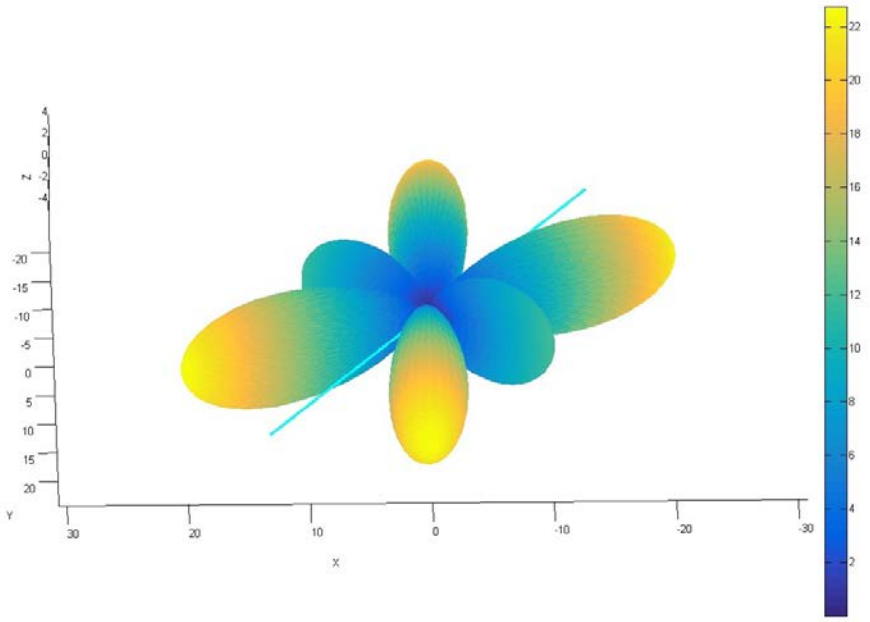

Figure 5.2: 3-D plot of the geometric linestrength of the $\Delta m = 0$ E3 transition for the experimental setup of trap 3 used in this work. The cyan blue line is the direction of the horizontally polarised probing beam.

of the atomic state evolves separately from the phase of the driving field. The result is a series of narrower fringes than observed with a comparable Rabi pulse time. The final technique used is an extension to the Ramsey technique referred to as hyper-Ramsey or generalised-Ramsey. In this family of pulse sequences, the Ramsey scheme is extended with additional pulses, phase steps and frequency steps. The effect of this can be to supress the size of systematic effects during the clock probe pulse, such as the AC Stark shift in Yb^+. Since the first proposed scheme [91] a number of hyper-Ramsey schemes have been proposed and demonstrated (e.g. [92], [93]). Rabi spectroscopy is used exclusively in our measurement campaigns.

A generalised spectroscopy sequence on a two level atom, ($|e\rangle = \binom{0}{1}$, $|g\rangle = \binom{1}{0}$, where the levels are separated by energy $E_e - E_g = \hbar\omega_0$ interacting coherently with a monochromatic radiation field of frequency ω, which is detuned from the atomic resonance by $\omega_0 - \omega = \delta$, with an effective Rabi frequency $\Omega = \sqrt{\Omega_0^2 + \delta^2}$ for a period of time t, can be formed using the matrices[91, 57],

$$\hat{A}(t, \Omega_0, \delta) = \begin{bmatrix} \cos(\Omega_r t/2) + \frac{i\delta}{\Omega_r}\sin(\Omega_r t/2) & \frac{i\Omega_0}{\Omega_r}\sin(\Omega_r t/2) \\ \frac{i\Omega_0}{\Omega_r}\sin(\Omega_r t/2) & \cos(\Omega_r t/2) + \frac{i\delta}{\Omega_r}\sin(\Omega_r t/2) \end{bmatrix} \tag{5.8}$$

and allowing the atom and light to evolve separately without interacting for a period of time T, with the detuning δ'

$$\hat{B}(T, \delta') = \begin{bmatrix} e^{iT\delta'/2} & 0 \\ 0 & e^{iT\delta'/2} \end{bmatrix} \tag{5.9}$$

In general, the atom will be prepared into the ground state with a near 100% fidelity. By stitching together a series of the matrices, each having potentially different times, detunings, phases, power levels etc, any desired pulse shape or sequence can be formed, allowing for exotic spectroscopic sequences [91, 93, 92] that can remove systematic effects that are only present during the interaction of the atom with the light field, or be used to aid in analysis of systematic shifts 6.1.2.

5.2.1. Rabi spectroscopy

When resonant light interacts with an atom, it causes the population of the ground and excited states to coherently oscillate - the population of each state

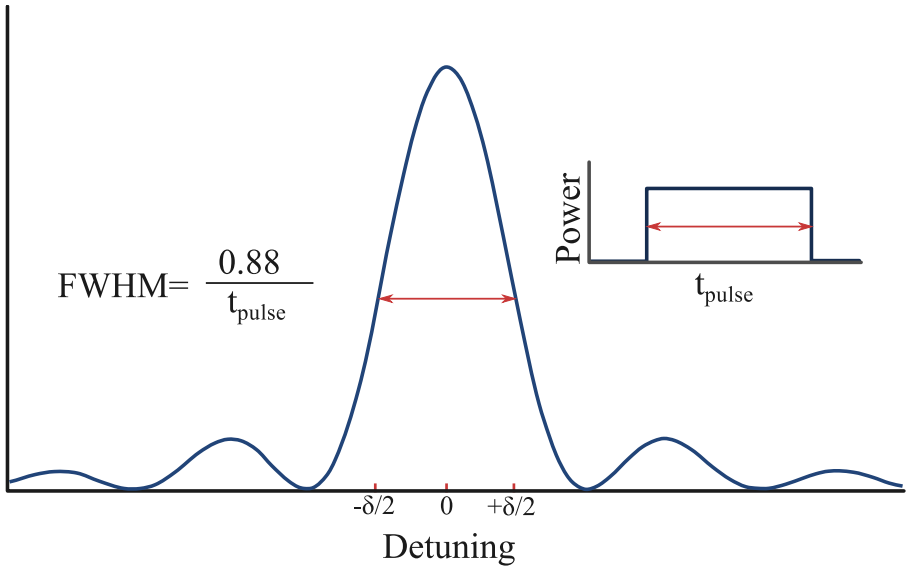

Figure 5.3: Rabi pulse excitation probability as a function of frequency detuning of the excitation pulse. Inset - example Rabi pulse. See text for details.

oscillates as $\sin^2(\Omega_r t)$, called Rabi oscillations, shown in figure 5.4. The frequency of this oscillation, known as the Rabi frequency Ω_r, is related to the electric field strength of the excitation light, and as such is proportional to the square root of the power,

$$\Omega_r \propto |\vec{E}| \propto \sqrt{P}. \tag{5.10}$$

Rabi spectroscopy a single pulse of uniform intensity. Therefore the excitation probability can be characterised by the Rabi frequency and pulse duration t. It is common for a pulse to be referred to by its effective angle, a π-pulse gives 100% excitation, a $\pi/2$-pulse results in 50% excitation etc. For the greatest signal, we want to operate at the maximum excitation probability - a π-pulse. By controlling the power of the light, we can ensure that for a given pulse length we are operating at the optimum excitation.

The resultant line shape as a function of frequency detuning is a sinc^2 function, with a line width (FWHM) of $0.88/t$, where t is the pulse length, as shown in figure 5.3.

$$P(\delta, t) = \frac{\Omega_0^2}{\Omega_r^2} \sin^2\left(\frac{\Omega_r t}{2}\right), \tag{5.11}$$

Things start to get a little bit more complicated when we consider the effect

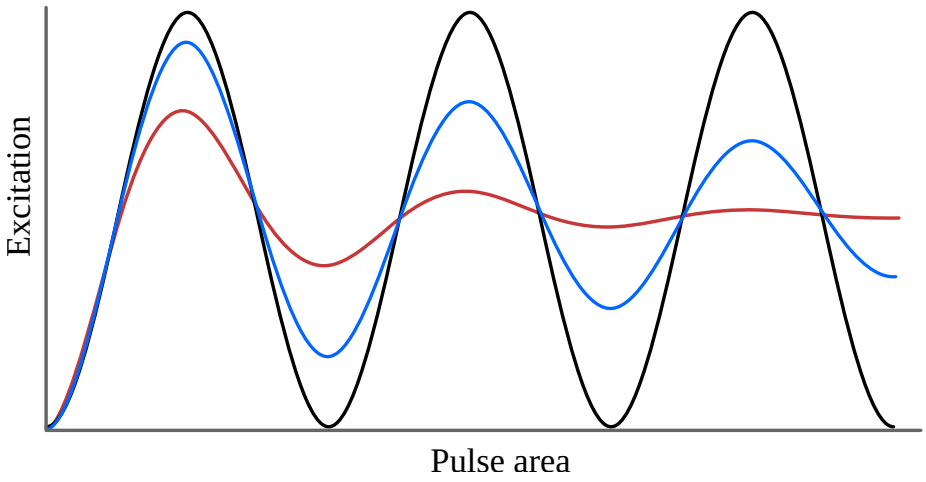

Figure 5.4: Oscillation of the atomic state population as a result of Rabi excitation.(black) Rabi oscillation of a atom interacting with a monochromatic light source. (blue) The finite linewidth and power fluctuations of the laser result in decoherence, This supresses the amplitude of the Rabi oscillations. (red) As decoherence increases, the oscillation decays to a steady 50% population.

of decoherence, as can be seen in figure 5.4, where Rabi flopping with 3 different illustrative decoherence rates is pictured. The decoherence results in a exponential suppression of the flops, to a steady state 50% excitation probability. The finite linewidth of the laser is the dominant cause of decoherence for the E3 transition, as different frequencies interact with the ion they cause a loss of coherence between the ion and the laser field. The finite lifetime of the excited state of the E2 transition dominates its decoherence processes. The choice of pulse length must balance the loss of signal due to decoherence with the benefits of a narrower line width.

5.3. Probing the clock transition

The experimental sequence starts by preparing the ion in the F=0 ground state. As the cooling cycle is based on being in the F=1 ground state, a 369 nm laser tuned to the $^2S_{1/2}(F=1) \rightarrow {}^2P_{1/2}(F=0)$ transition with 2.1 GHz sidebands is used to excite the $^2S_{1/2}(F=1) \rightarrow {}^2P_{1/2}(F=1)$ transition, effectively pumping the ion to the $^2S_{1/2}(F=0)$ ground state. This prepares the ion into the ground state with a high fidelity in only a few milliseconds. Before the clock excitation pulse begins, there is a brief delay which ensures all instruments have

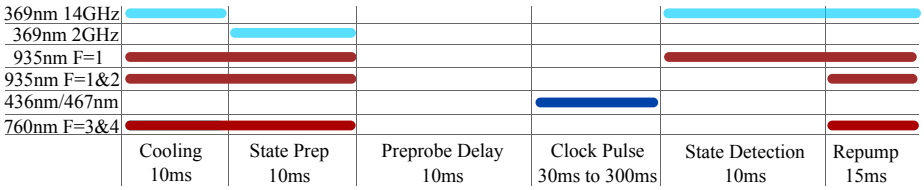

Figure 5.5: The relevant phases of probing the clock transition and lasers used during each state

finished communicating with the experimental control software, and ensures that shutters for cooling and repumping beams are closed, and the mechanical shutter for the clock beam also opens during this time. The intensity of the light is then controlled by an AOM, RF switch and DDS unit preprogramed with the correct spectroscopic sequence.

After the excitation pulse is complete, the state of the ion is detected using electron shelving. If the excitation was not successful, the ion will remain in the ground state, and will therefore fluoresce when exposed to the cooling laser. If the excitation was successful, the ion will be 'shelved' in the clock state, and will not fluoresce when exposed to the cooling laser.

A repumping and cooling phase then follows, which ends once ion fluorescence is detected again. Figure 5.5 shows the phases of one probing cycle and which lasers are active in each phase.

Because of the weak nature of the E3 transition, a large amount of power is needed to excite the transition - a few mW compared to a new nW for the E2. This large power creates a much larger probe light shift than is usual for other atomic clocks, with a shift of many 100s of hertz at typical operating conditions. This large shift puts a stringent requirement on the stability of the probe light power: even a 2% instability results in a change of the shift that is larger than the 10 Hz Fourier limited linewidth of a 100 ms pulse. To remove power fluctuations and ensure a pulse to pulse repeatability, the power in the 467nm probe beam is monitored and servoed to a predetermined value. This set up and its evaluation are discussed in chapter 6.1.

5.4. Locking to the clock transition

To lock to the clock laser to the atomic transition, the ion is repeatedly interrogated at $\omega = \omega_c \pm \delta/2$, where ω_c is the current estimate of the transition centre frequency, and δ is the FWHM linewidth of the observed transition. If the light

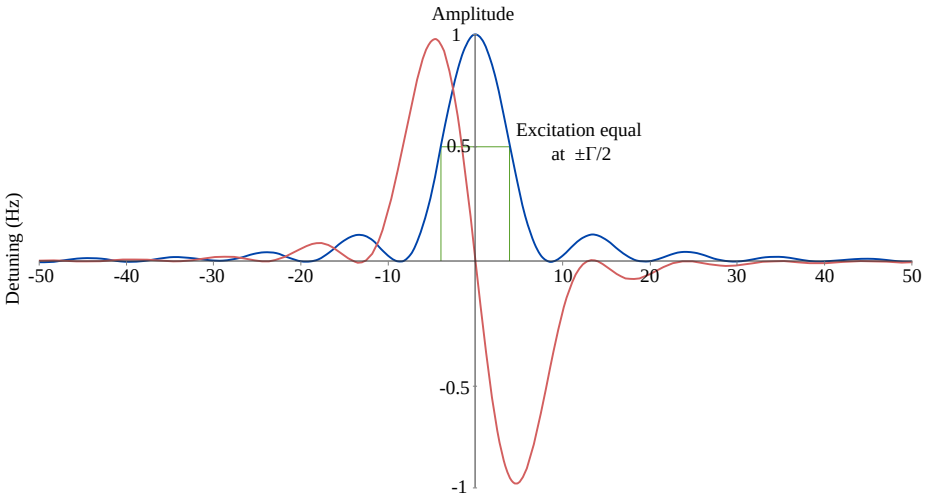

Figure 5.6: Simulated Rabi spectroscopy lineshape (blue) with the corresponding error signal (red) as a function of detuning based on a t_p =100 ms excitation pulse. The transition is alternately probed by laser pulses with relative frequency difference of Γ, the difference in excitation between these 2 pulses generates the error signal, which is zero when the average laser frequency is resonant with the transition (green).

is at the correct frequency the excitation probability will be the same on both half maxima. Any frequency deviation results in lower excitation on one side of the line and increased on the other. A simple subtraction of the observed excitation on the two sides of the line creates a dispersion like error signal than can be used to steer the laser to line centre. Since we only have a single ion, each side of the line is probed repeatedly to build up statistics. Figure 5.6 shows a Rabi lineshape, simulated using equation 5.8, from a 100 ms probe pulse and the corresponding error signal from this process.

To calculate the frequency correction for the observed error signal, the servo also takes into account the line width of the transition, and how many times the transition has been probed in the servo cycle. The servo has gain stages proportional to the error signal, and an integrator gain stage that acts on the total sum of the error signal across the measurement period. The frequency for the next servo cycle f_{i+1} for a given error signal e of the current servo cycle i is given by,

$$f_{i+1} = f_i + G_1 \delta e_i + G_2 \delta \Delta t_{i \to i+1} \sum_{n=0}^{i} e_n, \tag{5.12}$$

where the gains $G_{1,2}$ refer to the proportional and integral gains respectively, and δ is the transition line width. For transitions with an excited state life time close to the coherence time of the laser δ should be carefully chosen to optimise the stability of the clock output, e.g. [40, 94].

The statistical noise of exciting the transition is white, and therefore adds no offset so long as it is averaged to a sufficient level. One might assume that we can negate this effect by increasing the number of probe pulses in each servo cycle. While this has the effect of reducing the readout noise, the extra time taken to acquire the data completely negates the lower noise, resulting in no net change in stability[1]. In general it is better to operate with a shorter servo cycle for technical reasons. For example, due to the drift that ultra stable cavities exhibit, if a very large number of pulses are to be averaged over the laser will have drifted by a very large fraction of a line width. At best this causes a reduction in the signal and an effective broadening of the line, at worse this can lead to a systematic bias. This effect is still present for shorter servo cycles, but to a much smaller extent since the drift on short time scales is small. In order to further mitigate this effect, a pseudo scrambled pulse sequence is used, where rather than simply probing on the low side of the line the required number of times, then the high side of the line, the high side and low side pulses are evenly distributed throughout the servo cycle. To determine whether a particular pulse in a servo cycle is to be on the high side or low, the binary representation of the pulse number is XORed, and the Boolean result represents a high or low pulse, see table 5.2. This sequence has been shown to be immune to both first and second order drift of the error signal amplitude [95].

5.5. Producing a clock output

The output of the clock is an ultra stable optical frequency that is steered to a reference atomic transition. Note that the optical frequency need not be the transition frequency. The light can then be sent to a femtosecond comb where it can be measured relative to the microwave standards that currently define and realise the second, or measured relative to other optical clocks.

The undoubled, infrared light for both clock lasers is coupled to a polarisation maintaining fibre to distribute the light to the frequency comb labs. The areas between the labs where the fibres are laid are not environmentally con-

[1] C.f. lattice clocks or multiple ion clocks, where adding more atoms will increase stability because all the atoms are probed simultaneously

Pulse number	Binary	XOR
n	abc	$a \oplus b \oplus c$
0	000	0
1	001	1
2	010	1
3	011	0
4	100	1
5	101	0
6	110	0
7	111	1

Table 5.2: Table showing how the frequency of each pulse of a servo cycle is determined. The logical result of the XOR operation represents either a high frequency or low frequency pulse. The XOR operation essentially checks if the number of binary 1's is odd or even.

trolled and are subject to acoustic noise and temperature fluctuations. This causes noise on the phase of the light in the frequency comb labs, which can severely affect the stability of the light. When light travels through a medium with an inhomogeneous and time varying refractive index, the phase of the light at the output of the medium varies. If this process is white, it simply causes noise on the phase of the light. Note that if the process is not white, there is a chance that there is some off-set, if the refractive index linearly changes with time the effect is a change in the frequency of the light and a systematic shift on the clock frequency. The additional frequency noise added by transmission through these fibres can be in excess of 10^{-13}, which would broaden a 1 Hz laser to > 100 Hz. By retroreflecting a small portion of the light down any beam path and beating it with a small portion of reference light, we can form an interferometer, which can detect any phase changes of the light.

In the frequency comb lab there is an AOM, the first order of which is sent to the comb. A beam sampler is placed in the 1st order to retroreflect a portion of the light back down the fibre. An interferometer detects any noise picked up by the light transmitted through the fibre. The beat detection unit lies in our lab. Figure 5.7 shows this setup. The performance of these phase noise cancellation loops have been tested by measuring the light on two independent frequency combs, in separate labs with separate phase noise cancellation loops.

In order to relate the light measured by the comb to the ion, a number of corrections must be made. For the 934 nm light, the light that is sent to the ion is frequency doubled, then shifted up in frequency by a 125 MHz AOM. The

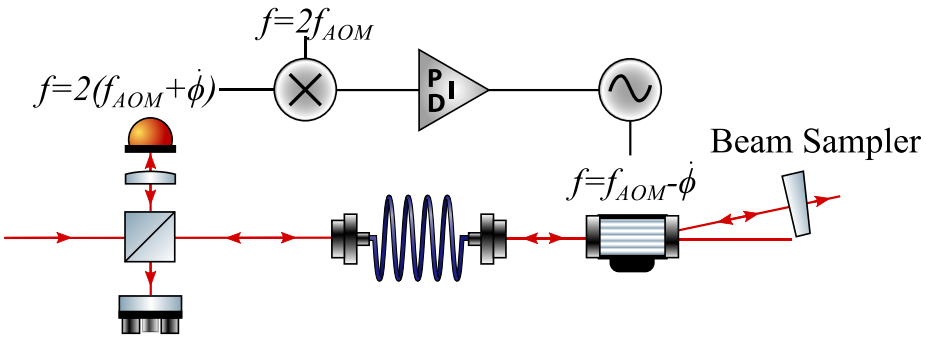

Figure 5.7: Schematic view of a basic phase noise cancellation setup. By using a Michelson interferometer, the phase/frequency noise introduced by the fibre is measured. At the transmission end of the fibre, an AOM is used to shift the frequency of the light. A partial retroreflector is placed on one of the frequency shifted orders. The doubly shifted light is then beat with a reference beam on a photodiode, which measures a beat at twice the AOM frequency plus twice the noise introduced by transmission through the fibre. An electronic feedback loop is used to servo this beat to be twice the AOM frequency, creating a phase stable output on the frequency shifted light. Note the AOM can be placed on either side of the fibre without affecting the technique.

phase noise cancellation set up, shown in figure 5.7 shifts the light at the comb by $\approx 80\,\mathrm{MHz}$ (the precise frequency changes by a few MHz for each comb and each laser), giving the relation,

$$\nu_{934} = \frac{\nu_{ion} - 125\,\mathrm{MHz}}{2} + 80\,\mathrm{MHz}. \tag{5.13}$$

With a similar relation for the 871, with the AOM frequencies and orders changed accordingly:

$$\nu_{871} = \frac{\nu_{ion} + 80\,\mathrm{MHz}}{2} + 80\,\mathrm{MHz}. \tag{5.14}$$

This directly relates the light at the ion to the light at the comb. Systematic shifts are present at the ion and thus also at the comb, however the required clock frequency is almost always the unperturbed frequency. Chapter 6 will discuss with how these systematic frequency shifts are removed.

CHAPTER 6

Systematic shifts and uncertainties

In this chapter we will examine the frequency shifts of the ytterbium ion optical clock. This will involve calculating the shift and its uncertainty, as well as methods used to minimise or null various shifts. The final part of this chapter will discuss some frequency shifts and sources of comparison uncertainty that are not inherent to the clock, but are artefacts of comparing 2 different clocks. We shall see, particularly in chapter 7, that minimising these comparison uncertainties might involve operating in a method that increases the systematic shift uncertainties of the clock, but lowers the overall uncertainty of the comparison. For each measurement campaign, each member of the Yb^+ team would calculate the systematic shifts, corrections and uncertainties independently using their own developed software and techniques to analyse the data. This gives a higher confidence in the resultant numbers than if just one person were to analyse the data with one method. Generally the shifts are not constant across a measurement campaign. We generate a grid of times with a frequency correction to remove our systematic shifts and the corresponding uncertainties that is then used by the frequency comb team to analyse their data an produce the final measurement results.

6.1. AC Stark shift

The AC Stark shift is a perturbation of the clock transition caused by the probe light off-resonantly coupling to other energy levels, and takes the form[96]

$$\Delta\nu = -\frac{1}{2h}\Delta\alpha_{sc}\langle E^2\rangle - \frac{1}{4h}\Delta\alpha_{ten}\frac{3m_F^2 - F(F+1)}{F(2F-1)}(3\langle E_z^2\rangle - \langle E^2\rangle), \qquad (6.1)$$

where the first term is the scalar shift, which depends only on the intensity of the light and the scalar differential polarisability between the two atomic states, $\Delta\alpha$, and is constant for a given wavelength of the electric field, E. The second term in equation 6.1 is the tensor term, that depends on the Zeeman component we are probing and the geometry of the experimental configuration since E_z is the component of the electric field vector parallel to the quantisation axis. For Yb^+, the ground state is a spherically symmetric S-state and hence the differential tensor polarisability $\Delta\alpha_{ten}$ depends only on the tensor polarisability of the excited state. Due to these geometric components, changing the direction of the quantisation axis, light polarisation or Zeeman level can drastically change the size of the total shift measured in the lab. The geometric factor of the tensor shift is common to all tensor shifts, and will be discussed more in the electric quadrupole shift section, where they will be used to completely remove a systematic shift. Vector shifts are absent from both clock transitions, since we drive transitions between the $m_F = 0$ components of both the ground and excited states.

Due to the weak nature of the E3 transition, a relatively large amount of power is required to excite the transition - a 30ms π-pulse on the E3 might require $3.8\,\mathrm{kW/cm^2}$ [1], whereas on the E2 it might be of the order $12.7\,\mathrm{mW/cm^2}$ [2]. This results in a substantial Stark shift of up to several hundred hertz on the E3 transition - a fractional shift of $\Delta\nu/\nu \approx 10^{-13}$. If we wanted to control this shift to the 10^{-18} level, that would require a power stability of better than 1 part in 10^5.

In general the shift can be greatly reduced by going to a longer probe time. If we consider a π pulse of length t, the required Rabi frequency Ω_t satisfies,

$$\pi = \Omega_t t,$$

[1] 3 mW of power in a $\sim 10\,\mu$m spot
[2] 10 nW of power in a $\sim 10\,\mu$m spot

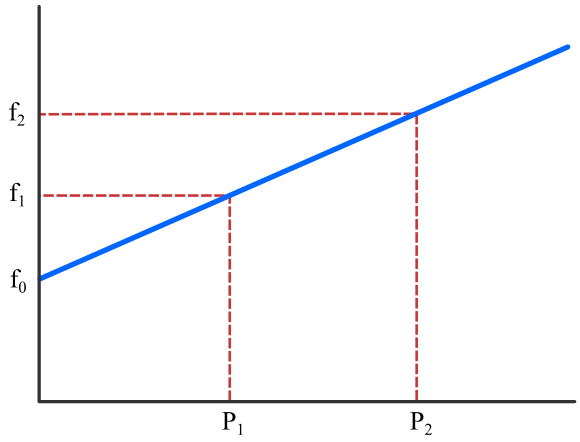

Figure 6.1: By measuring the clock frequency at 2 probe power levels, P_1 and P_2, the ac Stark shift can be extrapolated to the unperturbed frequency f_0. To do this, care must be taken to ensure the clock is operated in the regime where the ac Stark shift is linear with power.

thus a lower Rabi frequency is required at longer pulse lengths. The Rabi frequency is determined by the strength of the electric field at the ion, and thus the square root of the pulse power P. Therefore, to maintain a π pulse as the probe length changes $\sqrt{P}t$ must be constant, thus resulting in the relation for the stark shift

$$\Delta\nu \propto \frac{1}{t^2}, \tag{6.2}$$

yielding a significant reduction in Stark shift as the probe pulse length is increased.

6.1.1. Extrapolation to zero power

One can take advantage of the linearity of the shift with power to remove the shift from the clock output, as shown in figure 6.1. In order to do this, the clock frequency is measured at 2 power levels, with a known ratio $\kappa = P_2/P_1$. We can then extrapolate to the unperturbed frequency at zero power,

$$f_0 = \frac{\kappa f_1 - f_2}{\kappa - 1}. \tag{6.3}$$

The 467 nm light is power stabilised to a reference voltage by feeding back to the RF power driving an AOM, the 2 servo designs used are shown in figure 6.2. The reference voltage is provided by an NI-6012 DAC. The reference voltage is

switchable between 2 values and is controlled via a DIO line by the experimental control software. This allows the high and low power servos to operate in an independent and interleaved fashion. The power ratio is briefly precalibrated, such that the control software can remove the majority of the shift on-the-fly. Any residual Stark shift is removed in post processing (see below). Recently the power servo has been upgraded to consist of 2 servos: one removes the ac power noise from the light during the pulse, the other controls the long term dc power level. The advantage of this setup is that a single servo no longer has to be able to capture from 2 very different power levels whilst maintaining satisfactory capture time and noise reduction, which previously required compromised capture time and band width of the servo to maintain reliable capture at both power levels, see figure 6.3 for examples of the different performance of the servo at 2 power levels. It was also believed that the long term reliability of the servo could be improved by making this change.

In order to verify the performance of the power servo loop, there is an independent photodiode setup sampling the probe beam. This photodiode and transimpedance amplifier setup is calibrated for linearity across a large range of power levels. The output is fed to a 24-bit ADC, and processed in software to produce a relative power level that is free from the background light of the lab. This is then used to calculate the power ratio and its uncertainty, with the corrections being applied post processing. The ADC records the power level on a pulse by pulse basis, and as such allows for the power ratio to be adjusted multiple times in one data set during post processing.

To ensure that we are operating in the linear regime of the shift, the power ratio and absolute power levels are changed multiple times during a measurement campaign. If we are in the linear regime each data set extrapolates to the same unperturbed frequency.

6.1.2. Servo Capture

The power servo takes some time to settle to the correct power level. This will generally be a short period of time but might change for different power levels, see figure 6.3. Due to the large Stark shift, which can be of the order 100 Hz, these deviations from the set power alter the effective detuning of the light. For example see figure 6.4, where a small power overshoot leads to a small change in the Stark shift. This change in shift is a large fraction of the linewidth of the transition, and thus drastically changes the effective detuning of the high

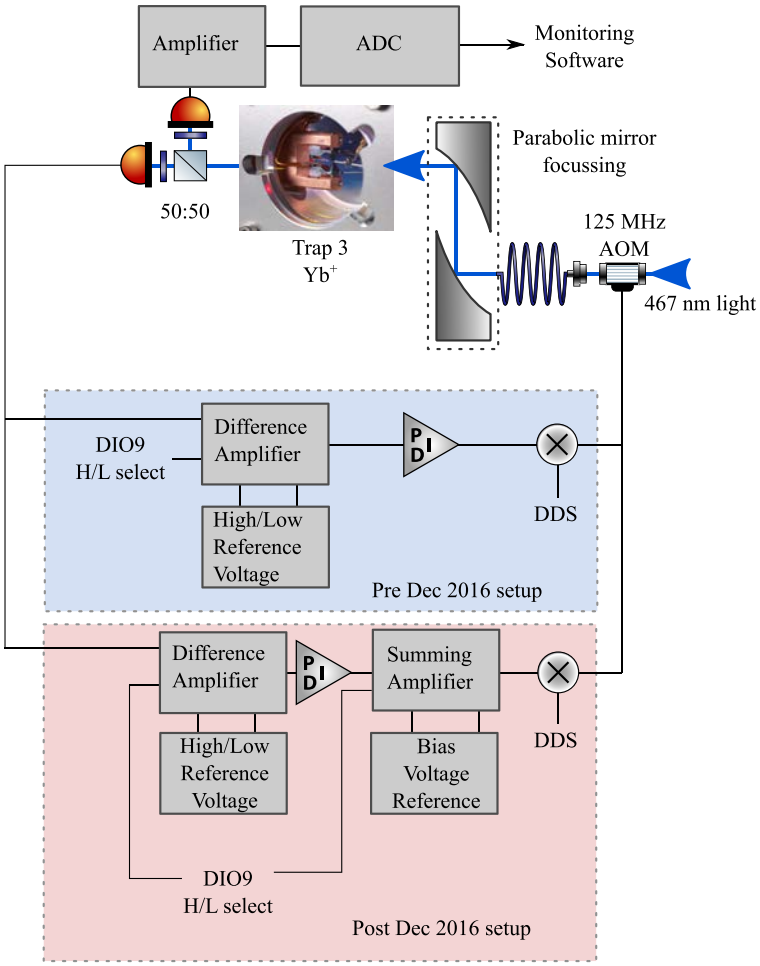

Figure 6.2: Schematic of the 467 power servo. DIO9 is a computer controlled digital channel that switches the servo between high power and low power. The changes made in December 2016 removed the DC level control from the servo electronics, placing it on the computer control instead via the bias voltage reference. The servo electronics are now solely responsible for removing the faster noise and preventing short term changes in the DC level. This helps to mitigate the servo performance shown in figure 6.3, where the servo performance was compromised to enable it to lock at 2 vastly different power levels.

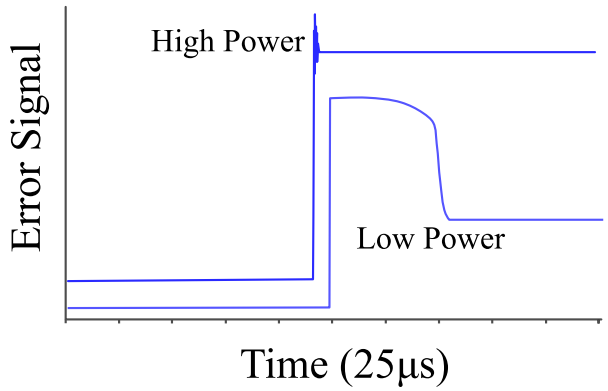

Figure 6.3: Example captures of the pre December 2016 power servo at the high and low power levels. The different behaviour is due to the servo electronics settings having to be the same for the 2 power levels. The traces have been offset for visibility. The entire time scale for the traces is 250 μs.

and low frequency servo pulses during the short transient time before the power level settles. This creates an excess of quantum jumps on one side of the servo and thus a slight biasing of the error signal, leading to a systematic frequency shift.

The shift is calculated by modelling the servo overshoot as a series of time steps at different detunings, and calculating how this biases the error signal of the servo. Figure 6.4 illustrates the most basic implementation of this method, where the overshoot has been modelled as 2 time steps of duration T_1, T_2 and power P_1, P_2, where the effective detuning of the first pulse is changed by $-\Delta\nu_{Stark}$.

6.1.3. Shutter Leakage

The laser beams used for cooling and repumping would also cause an ac Stark shift if they were left on during the clock pulse. In order to extinguish the beams, mechanical shutters are placed in all of the beam paths. The 369, 467 and 436 lasers also have AOMs that can aid in extinction. In general the mechanical shutters will extinguish the beams to a level consistent with zero power to within the resolution limit of the power meter. The shifts are calculated using polarisability values from [97]. In addition to this, we measured the shift caused by a controlled amount of 370 nm light by measuring the shift in an interleaved fashion, by comparing the shifted servo with one having no 370 nm light. Since

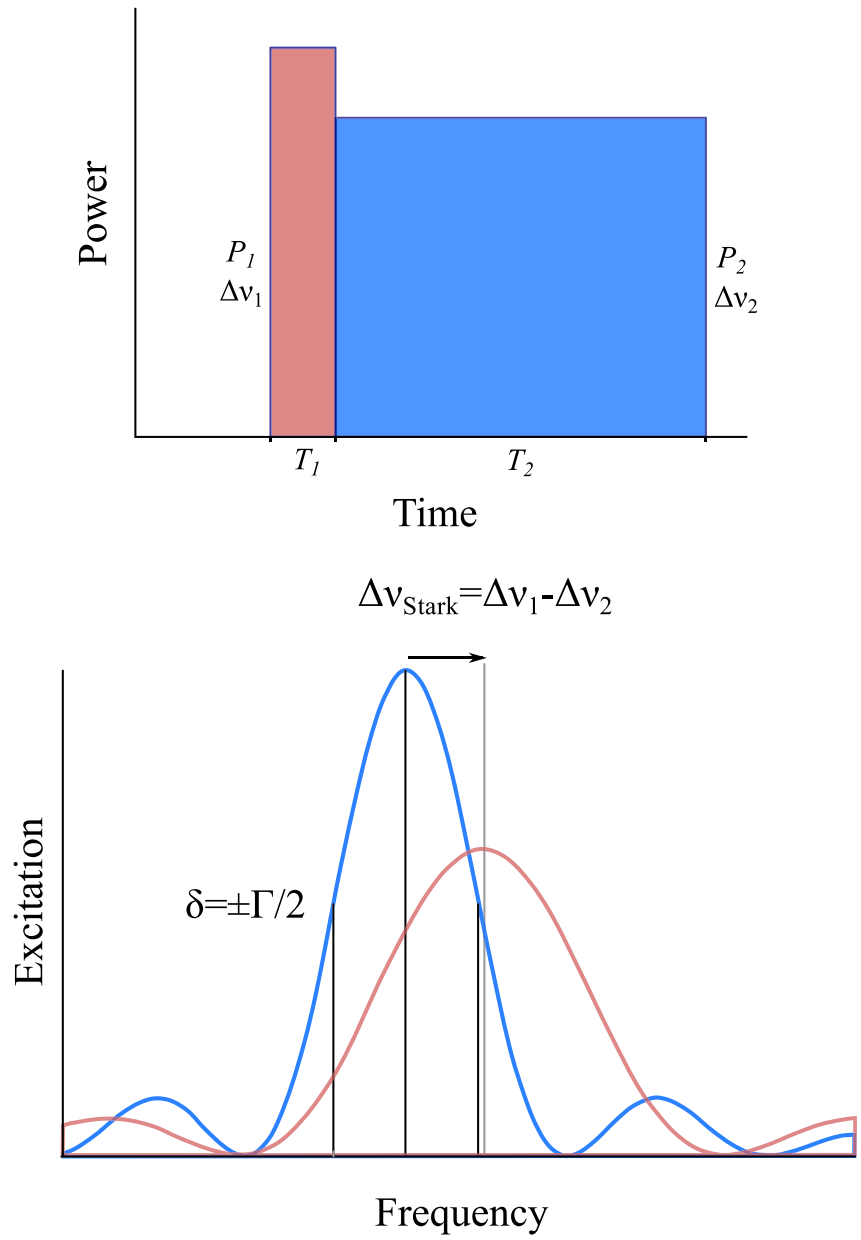

Figure 6.4: As the power servo captures, the first part of the clock pulse occurs at a slightly different power to the majority of the pulse. This initial part of the pulse has a different Stark shift, and hence drastically different detuning compared to the rest of the pulse. This creates a small excess of quantum jumps on one side of the servo, and a deficit of quantum jumps on the other side of the servo, thus leaving us with a small fictitious error signal that creates a systematic shift of the clock output. Note the different excitation rate for T_1 due to the different detuning and Rabi frequency at that power level.

this is a stronger transition than either the 935 nm or 760 nm transitions, leakage through this shutter would be the dominant cause of this type of shift.

6.2. Black body radiation shift

All physical bodies emit thermal radiation, described by Planck's law. This radiation interacts with the atom and, since clock frequencies are defined at absolute zero, causes a Stark shift of the form,

$$\Delta\nu_{\mathrm{BBR}} = -\Delta\alpha^{DC}\frac{4\sigma T^4}{2h\epsilon_0 c}(1+\eta), \tag{6.4}$$

where $\Delta\alpha$ is the differential polarisability of the atomic transition, and η is a small dynamic correction that accounts for the non-zero frequency of the BBR spectrum. Equation 6.4 doesn't have the tensor contribution of the more general equation 6.1, since the BBR field is assumed to be isotropic, averaging the tensor contributions to 0.

The main sources of uncertainty for this shift come from the BBR spectrum the ion is exposed to, and the accuracy of the differential polarisability,

$$\left(\frac{\sigma(\Delta\nu_{BBR})}{\Delta\nu_{BBR}}\right)^2 = \left(4\frac{\sigma(T)}{T}\right)^2 + \left(\frac{\sigma(\Delta\alpha)}{\Delta\alpha}\right)^2. \tag{6.5}$$

The thermal modelling provided by CMI results in a very low uncertainty in the temperature of the trapping environment, thus our uncertainty is dominated by our knowledge of $\Delta\alpha$ across the BBR spectrum.

The differential polarisability is mostly set by the dipole allowed transitions involving the upper and lower energy levels of the clock transition. For the E3 transition, the longest wavelength strongly allowed transition that couples to either of the states involved is the $^2\mathrm{S}_{1/2} \rightarrow ^2\mathrm{P}_{1/2}$ transition at 369 nm[3]. This means that the states couple very weakly to the black body radiation, allowing the transition to have a small black body shift. The E2 $\mathrm{D}_{3/2}$ state has a transition at 2.4 μm that links it to the $^2\mathrm{P}_{1/2}$ state. This leads to the E2 having a BBR shift about 10 times larger than the E3. To predict the shift of the BBR radiation on the clock transition involves calculating the differential polarisability of the states involved in the transition, and then integrating the effect over the BBR spectrum of the temperature of the trapping environment.

[3] there is a weak 3 μm transition that links the $\mathrm{F}_{7/2}$ state to the $\mathrm{D}_{5/2}$ state. This transition is weak enough to have been proposed as a frequency standard itself [68].

This process is incredibly challenging for ytterbium, because the core electrons are heavily involved in some states, such as the F states, and this induces a large number of electron-electron correlations. The current best calculations, inferred from experimental measurements of the DC differential polarisability of the E2 transition [98] and a calculation of the polarisability of the $^2F_{7/2}$ state [99], for the E3 transition result in an uncertainty of 50% on the BBR shift. Fortunately because the shift is so small this allows room temperature Yb^+ clocks to remain competitive with systems that have larger shifts but much more accurate calculations. The effect of the calculation uncertainty can be mitigated by using a cryogenic system, but this adds a large amount of complication and expense to the experiment.

6.3. Zeeman shifts

Both optical clock transitions in ytterbium are driven between $m_F = 0$ states of the ground and excited levels, and are therefore free from Zeeman shifts to first order. There is still a second order effect, proportional to the magnetic field squared. The magnetic field is measured by looking at the splitting of the Zeeman components of the E2 transition. The shift is then calculated for both transitions using measured coefficients. One might consider using the smallest field possible to minimise this shift, however this is a trade off, as 3 orthogonal and equal magnetic fields are required to average out the quadrupole shift. It is easier to satisfy these criteria with larger fields, since stray magnetic fields and technical limitations such as the resolution of current supplies become a smaller effect.

The shift is given by,

$$\Delta\nu = KB^2, \tag{6.6}$$

where B is the applied field in micro tesla and K is an experimentally measured constant. For the E2, $K = 52\,\mathrm{mHz}/\mu\mathrm{T}^2$, and for the E3, $K = -2\,\mathrm{mHz}/\mu\mathrm{T}^2$ [2].The clock operates in a field of $8\,\mu$T, generally in 3 sets of 3 mutually orthogonal fields to remove tensor shifts. These set of 3 fields are all measured using the splitting on the E2 Zeeman components, and must all be within 1% of the target magnitude when checked before and after a clock measurement for the measurement to be considered valid. In addition to the applied bias field, there is a small AC field present, the magnitude of which is estimated from the broadening of the Zeeman components - since the shift is second order in B,

any AC components do not cancel to zero. This means the net magnetic field is,

$$\langle B^2 \rangle = \langle B_{DC}^2 \rangle + \frac{\langle B_{AC}^2 \rangle}{2}. \tag{6.7}$$

The Zeeman splitting of the E2 transition is $8.4\,\mathrm{kHz}/\mu\mathrm{T}$. Due to the AC field noise, the Zeeman components are broadened to a few kHz, this gives us an estimate of the magnitude of the AC field, but it also introduces some slight fitting uncertainty in the splitting of the Zeeman components, which is a potential source of uncertainty to this shift.

6.3.1. Motional shifts

As the ion is trapped in a quadrupole electric field, the motion of the ion causes 2 kinds of shifts: time dilation shifts due to the non zero velocity, and Stark shifts caused by the trapping electric field. Since the motion of the ion in the trap is harmonic and in the Lamb-Dicke regime, there is no first order Doppler shift, but there are non negligible second order effects. Note that if there is a drift in the location of the trapping potential relative to the probe beam, a first order shift can be observed [100].

6.3.2. Ion velocity and displacement

The velocity and displacement of the ion comes from 2 causes, the slow 'secular' thermal motion of the ion, and the driven micromotion of the ion. The micromotion can be quantified with RF-photon correlation, whereas the extent of the secular motion is calculated from trapping parameters.

The micromotion results in an oscillatory Doppler shift of the cooling transition, of amplitude $\Delta\omega$, at the trap drive frequency, Ω, resulting in an oscillation of the ion fluorescence at the trap drive frequency, with an amplitude Δh,

$$\Delta h \propto \Delta\omega.$$

The modulation depth of this signal, M, is simply the oscillation amplitude normalised by the mean amplitude $h/2$, where h is the peak fluorescence. The modulation depth is then related to the mean ion displacement through the relation [101],

$$\bar{x} = \frac{M\lambda\Gamma}{4\sqrt{2}\pi\omega_x}, \tag{6.8}$$

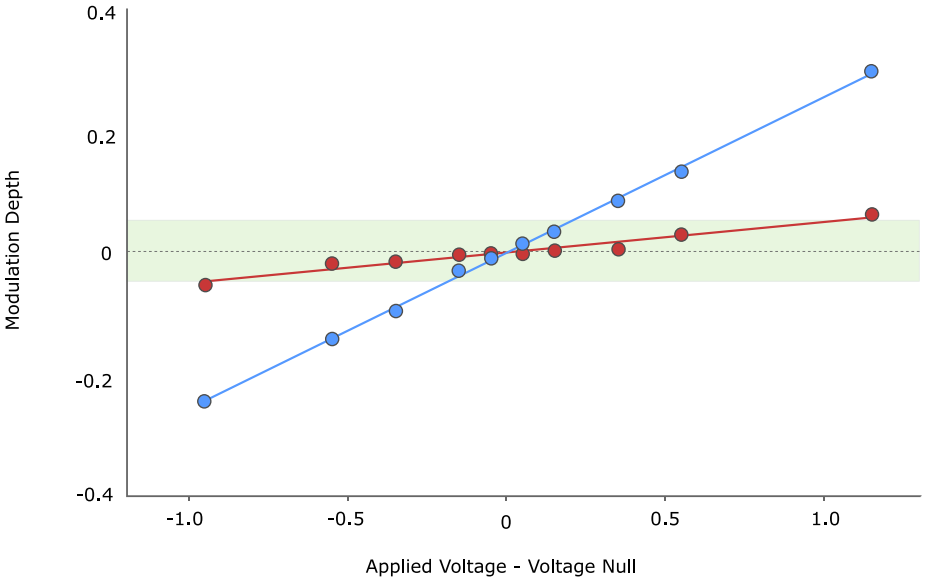

Figure 6.5: Ion fluorescnce modulation when excited with the horizontal beam. Blue and red data correspond to different compensation electrodes. Total micromotion shifts can be controlled to well below the 10^{-18} level on the E3 transition, shown by the green shaded band.

where ω_x is the secular frequency in the x direction, and λ and Γ are the wavelength and width of the cooling transition. Since the motion of the ion is harmonic, the mean displacement leads to a peak velocity of,

$$v_{max} = \sqrt{2}\omega_x \bar{x}. \tag{6.9}$$

The x direction in this case is the propagation direction of the laser. To get 3-D information about the displacement of the ion, 3 different lasers must be used. From these measurements the displacement of the ion in all 3 dimensions can be determined. This will normally be used to minimise the displacement, but typically some small displacement will remain. So long as the measured shift is small in comparison to other systematics and is not so large that the performance of the trap is degraded, this is not a problem. Figure 6.5 shows the modulation depth observed from the ion as a micromotion compensation voltage is altered, clearly showing that the micromotion, and thus the shifts it induces, can be controlled to a very high level.

6.3.3. 2nd Order Doppler Shifts

Both the secular and micromotion of the ion are harmonic and have a period much smaller than the probe time, and as the ion is in the Lamb-Dicke regime there is no recoil shift. This means there is no Doppler shift to 1st order in velocity, but there is still a second order shift, proportional to v^2. The shift is given by,

$$\frac{\delta\nu}{\nu} = -\frac{\langle v^2\rangle}{2c^2}. \tag{6.10}$$

Since the ion is cooled to $< 1\,\mathrm{mK}$, the average velocity is very low, $< 30\,\mathrm{cm{\cdot}s^{-1}}$ at the Doppler cooling limit. This leads to the correction being very small, it would be -4×10^{-19} at the Doppler cooling limit. The driven motion of the ion increases the average velocity, resulting in a larger correction. The velocity induced by micromotion can be calculated from equation 6.9. Due to the slower secular motion of the ion, there is an additional smaller contribution to the shift due to the temperature of the ion, T, giving a total shift of [102],

$$\frac{\delta\nu}{\nu} = -\frac{\langle v^2\rangle}{2c^2} - \frac{5k_BT}{2mc^2}. \tag{6.11}$$

In general this shift is controlled very well, with the absolute value of the shift being well below the 10^{-19} level.

6.3.4. RF Quadratic Stark shifts

The motion of the ion displaces it from the RF null of the trap. This means that is experiences a non-zero average electric field squared, resulting in a Stark shift to the clock transitions. The mean squared electric field resulting from this displacement can be found by using the gradient of equation 3.2,

$$\langle E_x^2\rangle = \frac{1}{2}(U_{ac}x)^2 = \frac{1}{2}\left(\frac{q_x m r_0^2\Omega^2}{2|e|\varepsilon'}\bar{x}\right)^2 \tag{6.12}$$

Since the trapping field is very far detuned from any atomic transitions, we consider the radio frequency field to be a DC field of RMS strength. The shift is given by,

$$\Delta\nu = \frac{1}{2h}\Delta\alpha_{DC}\langle E^2\rangle. \tag{6.13}$$

Similar to the 2nd order Doppler shift, there is an additional 2nd order Stark

shift from the thermal motion of the ion, giving a total shift of,

$$\Delta\nu = \frac{1}{2h}\Delta\alpha_{DC}\left(\langle E^2\rangle + \frac{mr_0^2\Omega^2 k_B T}{2e^2\varepsilon'^2\beta^2}\right) \tag{6.14}$$

6.4. Electric quadrupole shift

The electric quadrupole shift is caused by the interaction of the ion's electron cloud with the electric field. If the electron cloud distribution is not spherically symmetric, it possesses an electric quadrupole moment, which interacts with electric field gradients and causes a tensor shift of the clock transition. Any state with $J > 1/2$ exhibits this shift, and therefore both Yb^+ clock states exhibit this shift, though it is absent from the ground state. The atomic state $|\gamma J m_F F\rangle$ with quadrupole moment $\Theta(\gamma, J)$ has a quadrupole shift with the form,

$$\Delta\nu_{\text{quad}} \propto Q_{dc}\Theta(\gamma, J)\left(3m_F^2 - F(F+1)\right)\left(3\cos^2(\beta) - 1\right), \tag{6.15}$$

where Q_{dc} is a tensor that describes the electric field gradient. The remaining terms can be considered as geometric factors involving the Zeeman manifold of the state and the angle, β, between the electric field gradient axis and the quantisation axis.

6.4.1. Removing the shift

There are 2 commonly used methods for removing the shift. Both the magnetic sublevel term and the angular term of the shift average to zero when integrated over all sublevels or angles. The angular term also sums to zero when averaged over 3 orthogonal fields [103], and this method is used to remove the quadrupole shift for the work presented in this thesis. For the E3 clock state with F=3, a special condition is met; $3m_F^2 = F(F+1)$ for the $m_F = \pm 2$ sub levels. This means that the ± 2 components are completely free of ALL tensor shifts. The linear Zeeman shift can be removed by averaging over the positive and negative components, therefore making this a very attractive choice for a future improvement to the clock.

Rather than completely removing the shift, one could also work in a magnetic field that has a small quadrupole shift. By carefully calibrating the shift from a field in a fixed direction, a respectable uncertainty can be achieved whilst

also simplifying clock operation and increasing the clock uptime, which will become of importance in chapter 7. The uncertainty would then be limited by the statistics of the shift calibration, which is done by measuring relative to orthogonal magnetic fields.

6.4.2. Minimising the field gradient

The residual electric field gradient at the position of the ion is predominantly aligned with the trap axis [103], and can be changed by a suitable choice of micromotion compensation voltages, specifically when one has a pair of opposing electrodes to control the ion position along that axis (for example the end caps). The position of the ion is determined by the potential difference between the two electrodes, but the electric field gradient, as it is a tensor, is determined collectively by the voltages between all of the electrodes. One may be able to null the vertical micromotion with a 10V potential difference between the electrodes, however a poor choice in compensation voltages can cause the trap to have a non-zero a_i parameter which induces a potentially large quadrupole shift. Therefore one should select the exact values of the endcaps that minimise the electric field gradient. By using this method it is possible to make the quadrupole shift in trap 3 unresolvable in 3 orthogonal fields within the statistical noise after several hours of averaging. This method is also used to calibrate the shift in each field for measurement campaigns where we only operate in one field, as will be discussed in chapter 7. Note in all our ion traps we only have the ability to perform this nulling in the axial direction, since it is the only direction that has opposing sets of electrodes. For future designs of endcap traps, opposing electrodes will also be included for the radial directions to allow complete control of this systematic shift.

6.5. Comparison shifts

In order to verify the performance of a clock, it needs to be compared to something. During this comparison process, there are some uncertainties and shifts that can appear, especially if the comparison is between clocks located at different facilities.

6.5.1. Gravitational red shift

A result of the General theory of relativity is that clocks in different gravitational potentials tick at different rates. This was verified in the Hafle Keating experiment, where atomic clocks were flown on aeroplanes, and compared to atomic clocks that weren't flown around [51]. At the surface of the earth, the fractional gravitational red shift is well approximated by,

$$\frac{\Delta\nu}{\nu} = -\frac{gdr}{c^2}, \tag{6.16}$$

resulting in a shift of 10^{-16} per metre change in height, so for a comparison at the 10^{-18} level, the relative heights of the clocks need to be known to the 1 cm level!

A conventional choice of height reference level used by atomic clocks is the geoid, as the international timescale UTC uses the SI second on the geoid for its unit of time interval. Unfortunately the atomic clocks themselves are not static in height. They are affected by tides, weather systems, and even recoil effects from the melting of ice age glaciers. All of these effects have been well studied in the field of gravimetry. Given the location of the laboratories, corrections can be calculated by collaborating with gravimetry experts, as was done as part of the ITOC collaboration. Due to the effect of short term weather systems and such, these corrections must be calculated for each remote comparison.

6.5.2. Stability & link uncertainty

All measurements are subject to noise processes. In general, the effects of noise can be removed by repeating a measurement numerous times, averaging away the effects the noise. In time and frequency measurements, the statistical uncertainty of a measurement after a period of averaging is called stability (or instability). It is usually shown on Allan deviation plots, that display the fractional stability achieved as a function of averaging time. The operation of locking to the clock transition has a fundamental limit to the stability, governed by the noise of projecting the state vector, which can be averaged away, as discussed in chapter 1.4.4 . In addition to this there will be some noise related to any links between two clocks, which must be averaged through. This can be caused by the noise of transmitting the light through a fibre, which can be mitigated using the techniques discussed earlier. For remote clock comparisons using satelite based time transfer techniques, everything from transmitter temperature variations

to atmospheric propagation delays can degrade the quality of the link many components in a transmission link can cause phase noise which will degrade the stability in some way. The ideal state for a measurement campaign is that we average for long enough so that the statistical uncertainties are lower than clock shift uncertainties, and thus not affecting the accuracy of the comparison. This is not always practical.

6.6. Summary

This section has explained the cause of and methods used to measure and mitigate the systematic shift of the Yb^+ optical clock at NPL. The exact techniques used, and the resulting systematic uncertainties depend upon the exact set-up and conditions of each measurement campaign, which will be the topic of the next chapter.

CHAPTER 7

Measurement campaigns

The measurement of any absolute frequency requires relating it to the definition of the SI second through a realisation of the hyperfine ground state splitting of caesium 133. The most accurate realisation of the second is produced by caesium fountains. Due to the poor short-term stability of the realisation of the second, hydrogen masers are used as a flywheel standard, which is calibrated long term against caesium fountains. This allows us to use the higher stability of the hydrogen maser and the better accuracy of the caesium fountains. As we shall see in section 7.3, calibration of the maser does not always require a local primary standard.

Since optical clocks have a much higher stability and accuracy than microwave standards, the measurement and comparison of optical clocks is always degraded by any microwave standards explicitly used in the comparison. Using a frequency comb it is possible to measure the frequency ratio of two or more optical clocks completely independently of any microwave standards (even those used to stabilise f_{rep} and f_o of the comb)[33, 35], as explained in chapter 1.4.3. This allows for comparison of optical standards at a level better than the systematics floor of even the best microwave clocks. Since there is now a large international network of optical fibres, it also somewhat simplifies and greatly improves the accuracy and stability of international comparisons of optical clocks.

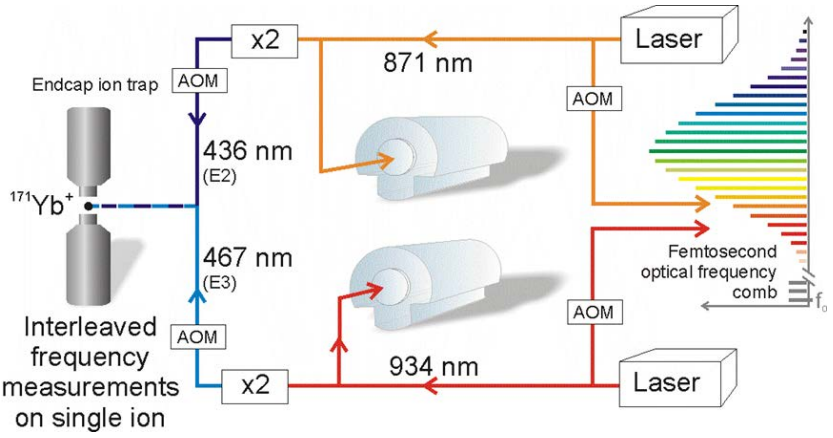

Figure 7.1: Setup during the optical ratio measurement campaign. In addition to this, the caesium fountain was also running, enabling absolute frequency measurements to be made at the same time.

The author's role during the measurement campaigns was day-to-day operation and optimisation of the clock, such as micromotion minimisation, ion loading, laser locking etc, as well as independant calculation of the systematic shifts, corrections, up times and uncertainties to compare with the values determined by the other team members.

7.1. February-March 2014

In February 2014, we undertook a measurement campaign to measure the direct frequency ratio of the E2 and E3 transitions in ytterbium and simultaneously to measure the absolute frequencies of both transitions relative to NPL's caesium fountain NPL-CsF2. This is the first time that the frequency ratio between the E3 and E2 transition had been measured, and the first time it was directly measured using the same single ion.

The basic setup of the experiment is shown in figure 7.1. The optical clocks were run in an interleaved manner, meaning that both the E2 and E3 clock laser were referenced to the ion at the same time. This leads to a perfect cancelling of the 2nd order Doppler shifts and the gravitational red shift between the two clocks, and allows the optical frequency to be measured using the comb as a transfer oscillator, without any reference to a microwave standard. This measurement was carried out in trap 1, and achieved the lowest systematic uncertainty budget in that trap for both transitions. Running in such an inter-

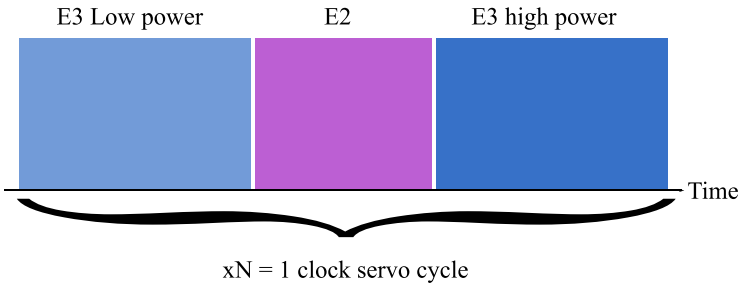

Figure 7.2: During interleaved operation, each clock interrogation phase has 3 clock pulses. The first and last pulse are for the E3 transition, and are at different power levels in order to remove the AC Stark shift. The middle pulse is the E2 clock pulse. This results in both the E2 and E3 servos having a mean temporal distribution at the centre of the servo cycle, removing possible laser drifts from the resultant frequency ratio.

leaved manner is not without issue. This technique requires 3 clock servos: 2 for the ac Stark shift cancellation on the E3 transition, and one for the lock to the E2 transition. They were interleaved on a pulse by pulse basis, meaning that the servos had a large amount of dead time while the other transition was being probed. This led to each step of the servo having 3 pulses: the first pulse being the low power E3, the middle pulse the E2 and the last pulse the high power E3, resulting in both E2 and E3 servo pulses being distributed with the same temporal mean. For this campaign the E3 transition was run with a 100ms probe pulse, and the E2 transition with a 30ms probe pulse, giving Fourier limited line widths of approximately 10 Hz and 30 Hz respectively. The dead time leads to a large reduction in the stability of both clock outputs. For the absolute frequencies, this was of no importance, as the statistical uncertainty was dominated by caesium. This did affect the optical ratio but a systematics limited uncertainty was achievable within a reasonable averaging time of 72 hours of simultaneous data. For the absolute frequencies 105 hours of E2 data and 81 hours of E3 data were recorded against caesium. A summary of the systematic uncertainties for the absolute measurements can be found in table 7.1.

The clock operated in a magnetic field of $10.00(5)\,\mu$T, measured by the splitting of the $\Delta m = \pm 1, 2$ Zeeman components of the E2 transition in 6 different fields, 3 of which were used for clock measurements. In order to null the quadrupole shift, as well as other tensor shifts, a set of 3 mutually orthogonal magnetic fields was used to measure the clock transitions, the average of which is free of all tensor shifts, as described in chapter 6.4. These field directions are

chosen to keep a relatively equal E3 line strength while having a useable E2 line strength. The field direction was rotated every 5 minutes, producing a tensor free frequency every 15 minutes. The quadrupole shift on the E2 transition was approximately +0.5 Hz, +9.5 Hz and −10 Hz in the chosen magnetic fields. The E3 transition has a much smaller quadrupole shift due to the smaller quadrupole moment of the F state. The tensor component of the AC Stark shift for the E3 is very large, approximately 10% of the ∼600 Hz scalar shift.

To allow the 10-60 Hz frequency step between each field direction, the steps are precalibrated into the computer control software, and then the first 30 seconds of each field direction is ignored to allow the servo to pull in. This is not the ideal way to run, as it results in 10% of all the data taken being deleted. Due to the large stainless steel vacuum chamber and design of the magnetic field coils, the magnetic fields cannot be quickly switched on e.g. a pulse by pulse basis. Table 7.2 shows the systematic uncertainties of the ratio measurement during the 72 hours of overlapping E2 & E3 data.

The absolute frequency of the E3 transition was found to be

$$\nu_{E3} = 642\,121\,496\,772\,644.91(37)\,\text{Hz},$$

and the absolute frequency of the E2 transition was found to be

$$\nu_{E2} = 688\,358\,979\,309\,308.42(42)\,\text{Hz}.$$

These numbers are in good agreement with values published by PTB and other measurements taken by NPL, see figures 7.3a & 7.3b. The direct optical frequency ratio was measured to be,

$$r = \nu_{E3}/\nu_{E2} = 0.932\,829\,404\,530\,964\,65(31).$$

This result is the first such measurement of this quantity, and is in good agreement with the ratio of absolute frequencies. Due to the E2 uncertainty being larger than the Cs fountain uncertainty, the direct optical frequency ratio uncertainty 3×10^{-16} is still above the uncertainty floor of the best Cs fountains $\sim 1 \times 10^{-16}$. In addition to this, due to the large ammount shared data between the absolute frequency measurements and the optical ratio measurement, the value and uncertainty of the ratio of absolute frequencies is almost identical to the optical ratio.

Since there is an established history of absolute frequency measurements, we

can use historic data to set a limit on any time variation of the fundamental constants. Since these are absolute frequency measurements, which therefore involve caesium, this measurement will have a sensitivity to both $\dot{\alpha}$, time variation of the fine structure constant, and $\dot{\mu}$, time variation of the proton-electron mass ratio. Figures 7.3a & 7.3b have lines of best fit to indicate any possible linear change of the absolute frequencies with time. Figure 7.3c shows the limits on $\dot{\alpha}$ and $\dot{\mu}$ set by these data, using techniques outlined in chapter 1.5.

By combining this result with previous absolute frequency measurements of Sr[5, 110], Sr^+[42, 43], Hg^+[46], Yb^+ E2 & E3, as well as measurements of the Al^+/Hg^+ optical clock frequency ratio made by NIST [45] and data from a radiofrequency transition in dysprosium[66], a best limit on the time variation of α and μ was made. Due to the rapid improvement in accuracy of frequency measurements in recent years, the results are mostly determined by the NIST optical frequency ratio, strontium lattice absolute measurements from PTB and SYRTE, and the measurements presented above. Figure 7.4 visualises the constraint, which has a 1σ value of,

$$\frac{\dot{\alpha}}{\alpha} = -0.7(2.1) \times 10^{-17} yr^{-1}, \tag{7.1}$$

$$\frac{\dot{\mu}}{\mu} = 0.2(1.1) \times 10^{-16} yr^{-1}, \tag{7.2}$$

indicating no violation of the standard model.

7.2. Precise Point Positioning (PPP)

In October 2014, we performed an international comparison of the E2 clock transition with the ytterbium ion system located at PTB in Germany. The method for this comparison was precise point positioning GPS using the international GPS service timescale (IGST). At the same time a broad band two way satellite test was performed in preparation for a European wide satellite based comparison happening in June 2015. Using dedicated GPS links at the 2 institutions, the local timescales produced by the hydrogen masers at both labs can be accurately compared - the rate of change of the time differences reveals the frequency difference between the two masers. By referencing each institutions optical clocks to their hydrogen masers they can then be compared.

The stability of the GPS PPP link is at the level of 10^{-15} at 1 day of averag-

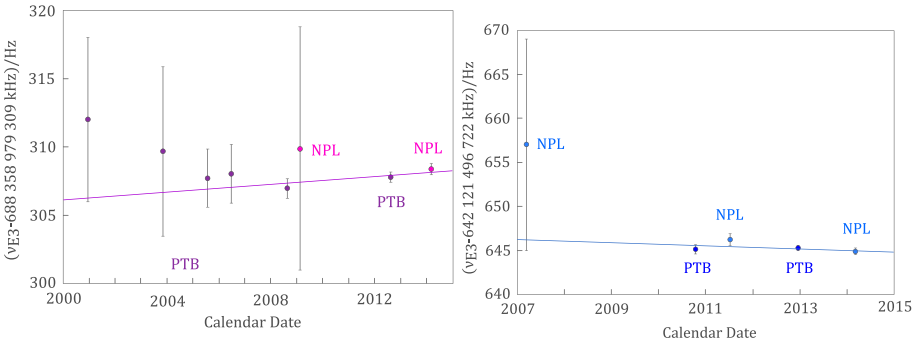

(a) The history of E2 absolute frequency measurements at both NPL and PTB [104, 98, 105, 106, 107, 108].

(b) The history of E3 absolute frequency measurements [109, 10, 8, 9].

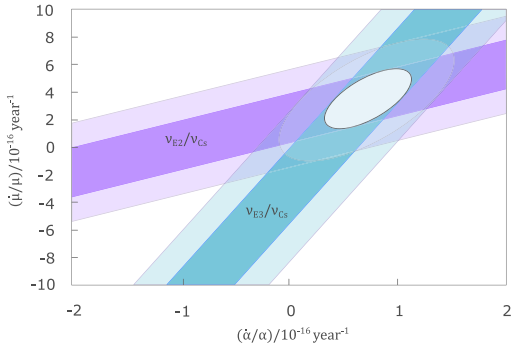

(c) Constraints on the linear variation of α and μ from the history of absolute frequency measurements of the E3 and E2 transitions in Yb^+. The darker shaded regions show the 1σ confidence and the lighter shaded areas the 2σ confidence.

Figure 7.3: Using the history of measurements of the E3 & E2 transitions, limits can be placed on $\dot{\alpha}$ and $\dot{\mu}$.

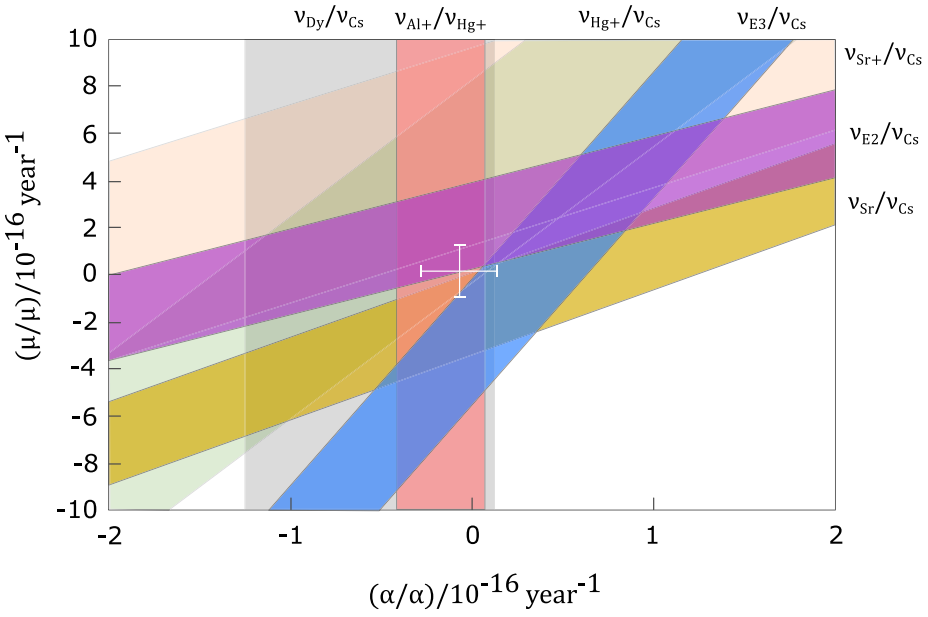

Figure 7.4: Constraints on α and μ when combining data from historical frequency measurements of numerous clocks from groups around the world. The white cross indicates the weighted mean of the variation of α and μ and the extent of the cross is the 1σ uncertainty on the mean. When published, this represented the best modern-day constraints on $\dot{\alpha}$ and $\dot{\mu}$. Chou 2010[3], Torgerson 2013[4], LeTargat 2013[5]

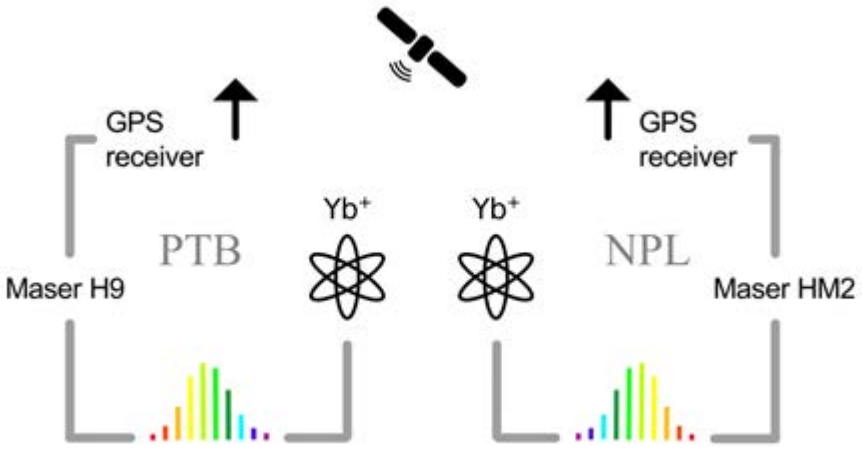

Figure 7.5: Setup of the PPP measurement, reproduced from [6].

ing[1], compared to the NPL E2 clock's stability of $1 \times 10^{-14}/\sqrt{\tau(\mathrm{s})}$, requiring in excess of 10 days of phase continuous averaging to reach the systematics floor of the E2 optical clocks at PTB and NPL. Even for the E2 transition, which has only modest stability for an optical clock, the averaging time is dominated by the link stability which takes 1 day to reach the same uncertainty the E2 clocks have in 100 seconds. For this reason much work has been put into optical fibre based comparisons where the stability of the link is better than that of the optical clocks.

The measurement of the E2 at PTB started on the 22nd of October, and at NPL on the 28th of October. The measurements ended on the 31st of October when the PTB hydrogen maser failed. This resulted in about 46 hours of overlapping data once dead time had been removed. The use of masers to bridge this dead time and the additional PTB E2 data to precalibrate the masers was studied in detail by J. Leute and colleagues at PTB and was the focus of the published analysis of this campaign [6].

This measurement campaign was conducted in trap 1. The clock was run very much as previous campaigns, except only the E2 transition was used. The magnetic fields were spun every 5 minutes to cancel the quadrupole shift. The removal of the first 30 seconds of data from each of these 5 minute chunks proved to make data analysis tricky, and a great deal of effort from our colleagues at PTB was put into performing modelling and data analysis to deal with how the maser is used to bridge this gap in the data. This injection of 10% dead time to give optimum systematic performance ended up not being the best choice, as the additional link uncertainty led to a very complicated analysis. An additional difficulty to this campaign was the large drift of the E2 clock laser due to a failed cavity temperature controller. This led to a cavity drift over 10 times larger than normal and delayed the start of the measurement at NPL.

The dominant systematic uncertainty of this campaign was the quadrupole shift. Due to fluctuations in the background field, the orthogonal field cancellation method does not work perfectly. In addition to this, even the applied fields absent of background fluctuations have some direction uncertainty. Analysis of these effects are discussed in the chapter 6. The added dead time and large uncertainty of this cancellation method led to a change in operation for future measurements, see section 7.3. Table 7.3 lists the salient systematic effects and their uncertainties for this measurement campaign, as well as the total values

[1] the link noise processes are dominated by white phase noise, and generally will average down as $1/\tau$

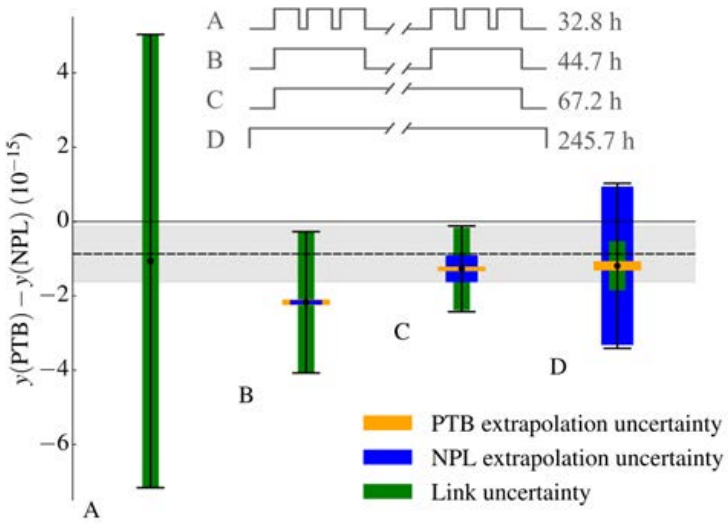

Figure 7.6: Total comparison uncertainty for different methods of bridging gaps in the data sets, reproduced from [6]. See text for details.

of the PTB E2 clock.

The dead time introduced by our quadrupole shift nulling had a large adverse effect on the overall uncertainty of the measurement. In order to ensure the data were valid, the magnetic fields were checked at least once every 24 hours, and the first 30 seconds of every 5 minutes of data were removed to ensure the servo recaptured after changing magnetic field. PTB developed a series of models of the hydrogen masers and GPS PPP link to examine how using the masers as flywheels to bridge these data gaps affects the total uncertainty of the comparison, discussed in detail in [6]. By using only the overlapping optical clock data 32.8 hours of data is available giving an uncertainty dominated by the link stability of 6×10^{-15} (point A in figure 7.6). By 'bridging' the 10% intrinsic dead time of the NPL clock and any gaps in the PTB data where NPL data is available by using the hydrogen masers as flywheel oscillators, 44.7 hours of data is available, point B in figure 7.6. This adds small uncertainties due to the extrapolation at the $\sim 10^{-16}$ level but reduces the link uncertainty to 2×10^{-15}. Further benefits can be made by extrapolating across all dead times, such as those used for checking magnetic fields, from the start of the NPL data to the end of the campaign, at the cost of a higher extrapolation uncertainty. Using this method 67.2 hours of data becomes available, point C in figure 7.6, with

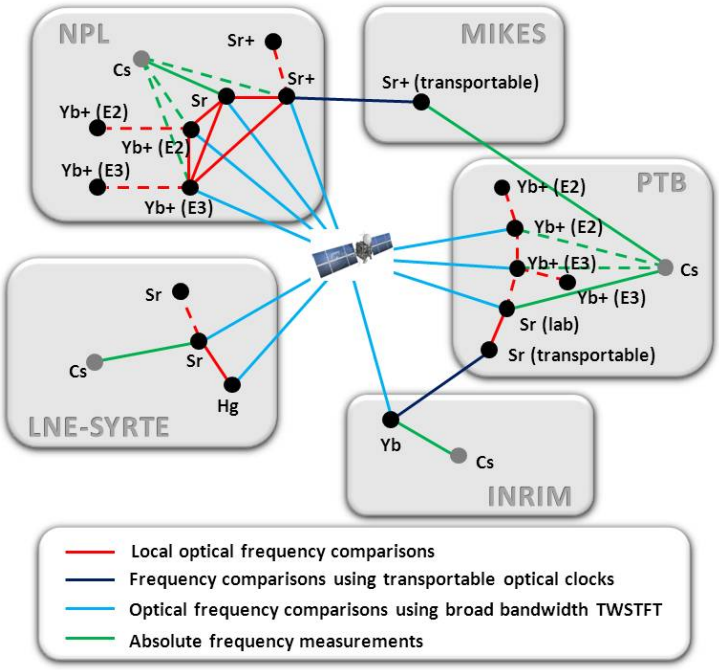

Figure 7.7: Scope of the ITOC broadband two way time and frequency transfer satellite measurement campaign. Reproduced from [7].

an extrapolation uncertainty of 3×10^{-16} with a total statistical uncertainty of 1.2×10^{-15}. PTB also looked at using the PTB data from before the NPL clock started running, but found the performance of the NPL hydrogen maser at these time scales started to degrade the total systematic uncertainty. Using the method that yields the minimum uncertainty, the fractional frequency difference between the 2 optical clocks was found to be,

$$\nu(\text{PTB}) - \nu(\text{NPL}) = -1.3(1.2) \times 10^{-15}, \tag{7.3}$$

in good agreement with the absolute frequency measurements relative to primary frequency standards found in section 7.1: $-0.87(75) \times 10^{-15}$.

7.3. ITOC

In June 2015, we participated in the largest international comparison of optical clocks to date, involving 7 different systems in 4 countries, as well as numerous

primary frequency standards, though the primary standard at NPL was not operational in the period. For more information about the ITOC project and the scope of the measurement campaigns, the user is directed to [111] and [7]. This measurement involved using a satellite to compare the local time scales of the laboratories involved, allowing for, in principle, a better comparison than the more traditional GPS based comparisons due the much better link stability that this comparison method was expected to achieve. Currently the extensive data analysis is still being performed, and as such results from this satellite comparison will not be presented here.

The large number of primary frequency standards contributing to this measurement also resulted in Circular T, the BIPMs monthly publication that provides traceability of local standards to UTC, having an unusually low uncertainty for that month, allowing for a very good absolute frequency measurement to be carried out relative to remote primary standards. The Cirular T data for June 2015 can be found in reference [112]. The Yb^+ clock operated between the 4^{th} of June and the 29^{th} of June 2015. A total of 1 661 688 s of data were taken with an up time of 75.9%. In order to achieve this uptime, which is impressive when compared to previous campaigns, the clock had to be operated in a new manner. This was the first measurement campaign that used trap 3. In addition to this it is therefore also the first international comparison using trap 3. This gave an exciting opportunity to test the benefits of the new system.

Historically we have removed tensor shifts by averaging the clock transition over 3 mutually orthogonal magnetic fields. This was accomplished by changing the field every 5 minutes and removing the first 30 seconds of data in order to allow the servo to capture on the new frequency, as described in previous sections. The frequency steps were precalibrated as the change in tensor Stark shift could be many tens of hertz, thus the servo would only have to pull in by the amount the precalibrated step was wrong by. This immediately gave the clock a 10% dead time, which can seriously degrade the statistical accuracy of an international comparison, as we found in the PPP campaign in section 7.2. Any data where the magnetic fields were found to be outside of their magnitude tolerances (usually 0.1 μ T) were removed since we could not be assured the direction of the magnetic fields had not changed. In addition to this, a compromised set of field directions had to be used such that the line strength of the E3 transition was similar in each direction and there was a reasonable E2 linestrength for the magnetically sensitive components used to measure the fields. This normally results in 3 fields with an orthogonality of better than 1 degree, with an E3

linestrength geometric factor of 20-25%. This reduced linestrength requires an increased power and thus Stark shift, which is detrimental to the overall clock accuracy. For this measurement campaign, the quadrupole shift was precalibrated using the E2 transition. Before the measurement started, a long E2 comparison was made, comparing the E2 frequency in 3 orthogonal fields. In trap 3 the quadrupole shift can be made very small, and the measurement was limited by the averaging time available. The shift in the 3 fields was resolved to the fractional frequency level of 1×10^{-15} on the E2 transition. Since the E2 quadrupole moment is 50 times larger than the E3, the E3 uncertainty is 50 times smaller than this. This allows us to measure with a reduced dead time and still achieve an uncertainty budget that does not limit the accuracy of the result. The quadrupole shift measurement was repeated during the campaign and after the campaign to verify that the shift had remained constant to within the uncertainty of the measurement.

Throughout this section a fractional frequency offset will be used where our measured frequency f will be compared to some reference frequency f_0, which is the 2013 CIPM recommended frequency value for the E3 clock transition,

$$f_0 = 642\,121\,496\,772\,645.6\,\text{Hz}, \tag{7.4}$$

and the reported offset is,

$$\frac{f}{f_0} - 1 \tag{7.5}$$

The frequency comb measures the frequency of the optical clock relative to the 10 MHz output of one of the NPL hydrogen maser HM2. Normally, the 10 MHz output of a maser is not exactly 10 MHz, therefore the frequencies measured have to have a correction applied to them. This task is normally achieved with local caesium fountains but in this measurement campaign Circular T is used. Circular T is a monthly publication from the Bureau International des Poids et Mesures (BIPM) that provides 5 day time offsets between Coordinated Universal time, UTC, and a national institute's local realisation of UTC, in our case UTC(NPL). Since UTC(NPL) is derived from HM2, we can use the reported value of UTC-UTC(NPL) to calculate the maser frequency offset from 10 MHz, which is found on average during the data acquisition period to be

$$\frac{f_{\text{HM2}} - f_{\text{UTC}}}{f_{\text{UTC}}} = -7793(164) \times 10^{-18}. \tag{7.6}$$

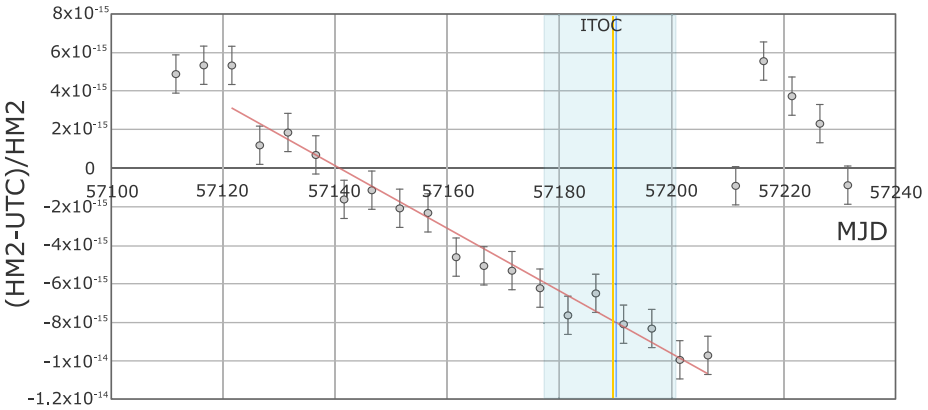

Figure 7.8: Fractional frequency difference between maser HM2 and UTC. The blues shaded region shows the ITOC measurement period, with the blue line being the centre of mass of the Yb^+ clock data and the yellow line the centre of mass of the HM2-UTC data. The red line shows the data used to estimate the drift of HM2 over the ITOC campaign.

This implies that HM2's frequency is too low, thus the result of any frequency measurement made relative to it will be too high and require a negative frequency correction. The optical clock dead time is not uniformly distributed throughout the data, so the temporal distribution mean of the measurement is slightly displaced. The mean fractional frequency drift of HM2 in this time period is $1.484(97) \times 10^{-16}$ /day requiring a further fractional frequency correction of $-312(20) \times 10^{-18}$ to the measured data. To link UTC to the SI second, Cirular T contains the fractional deviation of UTC from TT (terrestrial time - the SI second on the geoid), denoted d. The estimation of d is based on all the available primary and secondary standards' measurements over the preceding year. For our measurement period the best estimate gives $d = 0.81(0.18) \times 10^{-15}$ implying that a negative correction must be made to the measured frequency. The measured offset from the CIPM value is thus,

$$\frac{f}{f_0} - 1 = -718(398) \times 10^{-18}, \tag{7.7}$$

which equivalently gives the absolute frequency of the E3 transition as,

$$f = 642\,121\,496\,772\,645.14(26)\,\text{Hz}. \tag{7.8}$$

Table 7.4 enumerates the sources of uncertainty for this measurement.

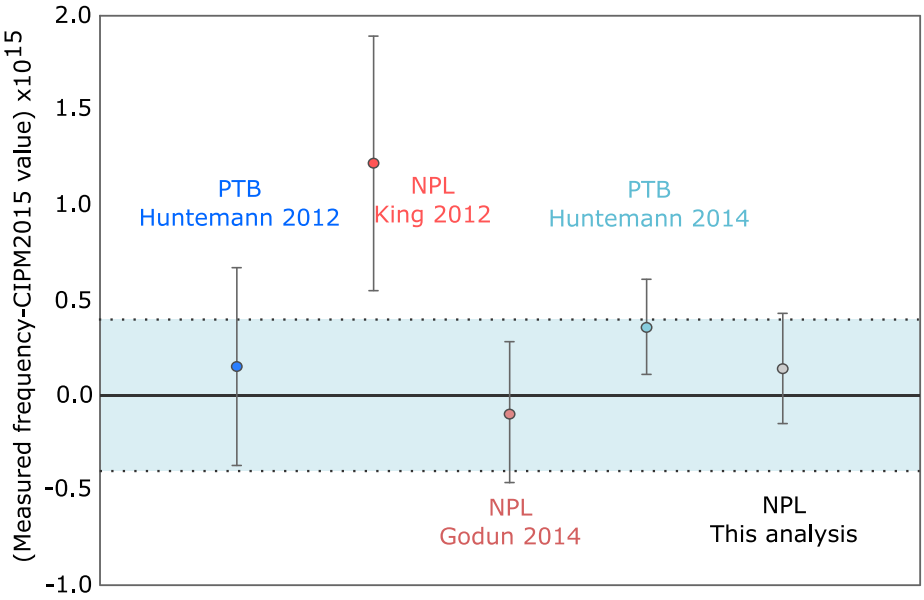

Figure 7.9: Comparison of the frequency measurement relative to circular T (black), with other recent measurements of the E3 transition. Included is the 2014 measurement from section 7.1 of this work (pale red). The pale blue band indicates the 2015 CIPM value of the transition and its associated uncertainty. Other measurements are shown in dark blue [8], light blue [9] and bright red [10].

This measurement compares very favourably with previous absolute frequency measurements using local fountains, see figure 7.9. With a value consistent with previous measurements and an uncertainty that is competitive with the best published measurement, this is an impressive feat given that there was no primary standard in operation at NPL over the measurement period. A paper containing this detailed analysis has been submitted for publication [113].

	E2		E3	
Source	$\delta\nu/\nu \times 10^{-16}$	$\sigma/\nu \times 10^{-16}$	$\delta\nu/\nu \times 10^{-16}$	$\sigma/\nu \times 10^{-16}$
Residual Quadrupole	0	2.91	0	0.06
Black Body Shift (Polarizability)	-4.86	0.99	-0.98	0.45
Black Body Shift (Temperature)	0	0.13	0	0.03
Quadratic Zeeman	75.76	0.77	-3.24	0.04
Quadratic RF Stark (Trap)	-0.41	0.41	-0.09	0.09
Second-order Doppler	-0.10	0.10	-0.10	0.10
Residual AC Stark (Probe Laser)	0	0.02	0	0.20
Servo Error	0	0.07	0	0.08
AOM Phase Chirp	0	0.06	0	0.06
AC Stark (370, 760 & 935)	0	0.07	0	0.08
Subtotal	70.39	3.19	-4.41	0.53
Statistical	0	4.77	0	5.35
Gravitational Redshift	-0.71	0.16	-0.71	0.16
Cs Fountain Systematics	0	1.90	0	1.90
RF Distribution and Synthesis	0	1.00	0	1.00
Total	69.68	6.13	-5.12	5.79

Table 7.1: Uncertainty budget for the absolute frequency measurements during the ratio measurement campaign. Columns labelled $\delta\nu/\nu \times 10^{-16}$ show the size of the shift and $\sigma/\nu \times 10^{-16}$ the uncertainty of that shift.

Source	Ratio E3/E2 σ/ratio(10^{-16})
Residual Quadrupole	2.97
Black Body Shift (Polarisability)	1.09
Black Body Shift (Temperature)	0.11
Quadratic Zeeman	0.80
Quadratic RF Stark (Trap)	0.33
Residual AC Stark (Probe Laser)	0.20
Servo Error	0.11
AOM Phase Chirp	0.09
AC Stark (370, 760 & 935)	<0.01
Subtotal	3.29
Statistical	0.68
Total	3.36

Table 7.2: Uncertainty budget for the ratio measurement during the 72 hours of overlapping E3 & E2 data.

	$\delta\nu/\nu \times 10^{-16}$	$\sigma/\nu \times 10^{-16}$
BBR	-4.86	0.99
2^{nd} Order Zeeman	75.66	0.77
Residual Quadrupole	0.00	2.90
Quadratic DC Stark Shift	-0.19	0.19
Pathlength Error	0.00	0.06
Servo Error	0.00	0.07
2^{nd} Order Doppler	-0.05	0.05
Light Shift	0.00	0.08
Total	70.56	3.16
PTB Total	4.34	1.04

Table 7.3: Summary of the systematic shifts of the E2 standard. The PTB total numbers are also included for comparison. Note how although there is a factor of 16 difference between the size of the total shifts, the total uncertainties are quite similar - only a factor of 3 difference.

Process	$\sigma(f/f_0) \times 10^{-18}$
HM2 v UTC correction	164
UTC v SI correction	180
HM2 extrapolation	120
EAL extrapolation	250
HM2 drift	20
RF distribution and synth	100
E3 statistics	16
E3 AC Stark	106
E3 systematics (other)	20
Total	398

Table 7.4: Uncertainty budget of the measurement of the Yb^+ E3 clock transition relative to HM2 calibrated using circular T.

CHAPTER 8

Conclusions

This work has focussed on development of an Yb^+ optical clock system, and using it to partake in measurements and comparisons with other clocks both locally and internationally. The techniques used to both operate the clock, and evaluate its systematic uncertainty have been presented and discussed, and then applied to the measurement campaigns performed. The first of these was the measurement of the E2/E3 ratio; this was the first time this quantity had been measured directly and the first time an optical ratio had been measured in a single ion. This measurement was the pinnacle of the older design of Schrama trap at NPL, with the design choices that were made when they were constructed in the late 90s now limiting the accuracy of the clock operation. We also undertook an international comparison with the PTB Yb^+ system, comparing the E2 transition frequency at the 10^{-15} level by using GPS PPP. This measurement was also part of a warm-up campaign for one of the ITOC measurements - a much larger, wide ranging campaign involving all of the optical clocks in 4 NMIs across Europe, and a dedicated broadband satellite link between the institutions. The data analysis for this vast measurement is still ongoing, and a number of publications are expected to be submitted in the near future. These range from gravimetry measurements in and around the clock laboratories to better define the heights of the European clocks above the geoid, to potential measurements/limits of fundamental physics effects.

A new trap was designed and built, and in chapter 3 we explored some of the advantages of this design. Once this trap assembly had been loaded, it was able to perform its first measurement campaign - taking part in the aforementioned ITOC satellite comparison. Due to the large number of primary standards operating at this time, a very accurate absolute frequency measurement could be made, even though the NPL Cs fountain was not in action at the time. This was done by using Circular T to calibrate the NPL timescale during the measurement. This has resulted in NPL's most accurate measurement of the E3 transition to date, all whilst the NPL primary standard was not reporting to BIPM.

Due to the sensitivity of the Yb^+ E3 transition to changes in the fine structure constant, we have also been able to use it to set stringent modern-day limits to time variation of α. The increasing number of clock comparisons and ever reducing uncertainty budgets means that new best limits on this variation are being set regularly.

The conclusion of this work is that the Yb^+ optical clock at NPL is now progressing from an experimental apparatus to more of a functional clock. Great steps forwards have been made in terms of unattended operation, reliability, clock up time, and required maintenance. This has been achieved partly by changes in the optical setup, for instance using waveguide doublers rather than resonant doubling cavities, partly because of the new trapping apparatus, described in detail in chapter 3, and partly because of electronics upgrades, such as the new micromotion compensation voltage supplies described in detail in chapter 3.3.4.

8.1. Next steps

The immediate future of the Yb^+ system will be numerous improvements aimed at improved reliability and reduced uncertainty. Over the next couple of years there is an ambitious measurement campaign schedule, including many comparisons with European optical clocks as part of the OFTEN project[114]. This will help demonstrate the repeatability and general performance of the system, providing a stronger case for an optical redefinition of the second.

Improving reliability

There are still a number of improvements that can be made to make the clock more robust. The biggest causes of dead time are the day to day maintenance of the magnetic field null, micromotion null, and reloading the trap when the ion is lost. With the new micromotion voltage supplies constructed as part of this work, automating the micromotion minimisation is now feasible, requiring only the addition of 3 shutters, which have recently been installed. A new 399 nm laser has been ordered, based on an NEL waveguide frequency doubler and a Sacher micron laser operating at 798 nm, since the biggest time sink during loading has historically been the time taken to get the home-made 399 nm laser to lase single mode at the correct wavelength. Generally the first or second loading attempt will be successful once the laser is at the correct mode. The next generation trap, currently being constructed, has 3 layer mu-metal shields to help suppress any background magnetic field changes. Once these hardware changes have been completed, changes must be made to the trap control software to allow us to take full advantage of them, potentially pausing the lock to the ion every so often to measure the magnetic fields or micromotion, potentially even allowing the clock to automatically reload the ion and relock to the transition. This ability to operate unattended is not only desirable for operation as a primary standard, but will be needed for any potential commercialisation of an optical ion clock.

8.1.1. SI second

An optical redefinition of the second has long been proposed, with optical atomic clocks being anticipated as early as 1982 [27], and many detailed review articles detailing the progress towards this goal, e.g. [115]. This was spurred on by rapidly decreasing uncertainties of optical clocks, quickly surpassing even modern caesium fountains, and the greatly improved stability compared to caesium that made reaching these uncertainties possible. Only recently has the technology required for a high up-time, reliable optical clock actually become feasible. Even during the ITOC campaign the best uptime throughout the measurement was close to 80% - and that was over a prearranged period of time where the experimenters had time to prepare. So although there is definitely some work still to do, the progress has been remarkable and rapid - compare the frequency ratio measurement campaign that we undertook in 2014, which was about 3 weeks long and took about 70 hours of data, to the 75% uptime we achieved

during ITOC in 2015. Before a redefinition can be considered, which ever species is eventually chosen will need to demonstrate its performance with numerous independent international comparisons with a low comparison uncertainty.

Demonstration of uncertainty & repeatability

When attempting to redefine the second, care must be taken that the transition is smooth - at the point of changing the definition, the length of a second shouldn't change. This requires a comprehensive determination of the frequency of the new defining transition relative to caesium. BIPM maintains a library of recommended values for transitions based on these absolute frequency measurements (and more recently some optical ratio measurements) but many of these values are heavily weighted by measurements from just one or two groups. This could cause a potential issue if there is some unknown offset in these heavily weighted measurements. As such it is vital that many truly independent measurements are used to determine the frequency of the new transition at the point of redefinition.

8.2. Outlook

In the more recent measurement campaigns, the Yb^+ optical clock at NPL has skirted ever closer to achieving a systematic uncertainty budget at the 10^{-18} level. In the past we have been prevented from achieving this by failures in certain parts of the experiment, such as the power servo monitoring system. Each of these failures resulted in improvements to the system to prevent it from happening again, and it will not be long before a whole measurement campaign is conducted where the total systematic uncertainty is at the mid-low 10^{-18} level. The development of techniques to counter the large AC Stark shift of Yb^+, advances in laser technology, and the numerous tests of fundamental physics available to Yb^+ optical clocks means that this system will be of interest for many years to come.

Bibliography

[1] H. S. Margolis, "Frequency metrology and clocks," *Journal of Physics B: Atomic, Molecular and Optical Physics*, vol. 42, p. 154017, Aug. 2009.

[2] R. M. Godun, P. B. R. Nisbet-Jones, J. M. Jones, S. A. King, L. A. M. Johnson, H. S. Margolis, K. Szymaniec, S. N. Lea, K. Bongs, and P. Gill, "Frequency Ratio of Two Optical Clock Transitions in $^{171}Yb^{+}$ and Constraints on the Time Variation of Fundamental Constants," *Phys. Rev. Lett.*, vol. 113, p. 210801, Nov 2014.

[3] C. W. Chou, D. B. Hume, J. C. J. Koelemeij, D. J. Wineland, and T. Rosenband, "Frequency Comparison of Two High-Accuracy Al^{+} Optical Clocks," *Physical Review Letters*, vol. 104, p. 070802, Feb. 2010.

[4] J. R. Torgerson and D. Budker, "New Limits on Variation of the Fine-Structure Constant Using Atomic Dysprosium," *Physical Review Letters*, vol. 060801, no. August, pp. 1–5, 2013.

[5] R. Le Targat, L. Lorini, Y. Le Coq, M. Zawada, J. Guéna, M. Abgrall, M. Gurov, P. Rosenbusch, D. G. Rovera, B. Nagórny, R. Gartman, P. G. Westergaard, M. E. Tobar, M. Lours, G. Santarelli, A. Clairon, S. Bize, P. Laurent, P. Lemonde, and J. Lodewyck, "Experimental realization of an optical second with strontium lattice clocks.," *Nature communications*, vol. 4, p. 2109, Jan. 2013.

[6] J. Leute, N. Huntemann, B. Lipphardt, C. Tamm, P. Nisbet-Jones, S. King, R. Godun, J. Jones, H. Margolis, P. Whibberley, A. Wallin, M. Mermiaa, P. Gill, and E. Peik, "Frequency Comparison of $^{171}Yb^{+}$ Ion Optical Clocks at PTB and NPL via GPS PPP," *IEEE Transactions on Ultrasonics, Ferroelectrics, and Frequency Control*, vol. 63, no. 7, 2016.

[7] "NPL's ITOC project website." `http://projects.npl.co.uk/itoc/`. Accessed: 07-07-2017.

[8] N. Huntemann, M. Okhapkin, B. Lipphardt, S. Weyers, C. Tamm, and E. Peik, "High-Accuracy Optical Clock Based on the Octupole Transition in $^{171}Yb^{+}$," *Physical Review Letters*, vol. 108, p. 090801, Feb. 2012.

[9] N. Huntemann, B. Lipphardt, C. Tamm, V. Gerginov, S. Weyers, and E. Peik, "Improved Limit on a Temporal Variation of m_p/m_e from Comparisons of Yb^{+} and Cs Atomic Clocks," *Phys. Rev. Lett.*, vol. 113, p. 210802, Nov 2014.

[10] S. A. King, R. M. Godun, S. A. Webster, H. S. Margolis, L. A. M. Johnson, K. Szymaniec, P. E. G. Baird, and P. Gill, "Absolute frequency measurement of the $^2S_{1/2} \rightarrow {}^2F_{7/2}$ electric octupole transition in a single ion of $^{171}Yb^{+}$ with 10^{-15} fractional uncertainty," *New Journal of Physics*, vol. 14, p. 013045, Jan. 2012.

[11] "Nist atomic data for ytterbium." `http://physics.nist.gov/PhysRefData/Handbook/Tables/ytterbiumtable1.htm`. Accessed: 15-02-2017.

[12] V. V. Flambaum and V. A. , Dzuba, "Search for variation of the fundamental constants in atomic, molecular, and nuclear spectra," *Canadian Journal of Physics.*, vol. 87, pp. 25–33, Jan 2009.

[13] M. Auzinsh, D. Budker, and S. M. Rochester, *Optically Polarized Atoms: Understanding light-atom interactions*. 2010.

[14] F. Riehle, *Frequency Standards: Basics and Applications*. Wiley-VCH, 2005.

[15] L. Rogers, "A brief history of time measurement," *https://nrich.maths.org/6070*, 2008.

[16] BIPM, "Unit of time (second)," *SI Brochure: The International System of Units (SI) [8th edition, 2006; updated in 2014*, no. 2.1.1.3, 2016.

[17] W. M. Itano and D. J. Wineland, "Laser cooling of ions stored in harmonic and Penning traps," *Phys. Rev. A*, vol. 25, pp. 35–54, Jan 1982.

[18] K. B. Davis, M. O. Mewes, M. R. Andrews, N. J. van Druten, D. S. Durfee, D. M. Kurn, and W. Ketterle, "Bose-Einstein Condensation in a Gas of Sodium Atoms," *Phys. Rev. Lett.*, vol. 75, pp. 3969–3973, Nov 1995.

[19] M. H. Anderson, J. R. Ensher, M. R. Matthews, C. E. Wieman, and E. A. Cornell, "Observation of Bose-Einstein Condensation in a Dilute Atomic Vapor," *Science*, vol. 269, no. 5221, pp. 198–201, 1995.

[20] Nobelprize.org, "The Nobel Prize in Physics 2001." http://www.nobelprize.org/nobel_prizes/physics/laureates/2001/, 2001.

[21] C. Monroe, D. M. Meekhof, B. E. King, W. M. Itano, and D. J. Wineland, "Demonstration of a fundamental quantum logic gate," *Phys. Rev. Lett.*, vol. 75, pp. 4714–4717, Dec 1995.

[22] S. N. Lea, "Limits to time variation of fundamental constants from comparisons of atomic frequency standards," *European Physical Journal: Special Topics*, vol. 163, pp. 37–53, Sept. 2008.

[23] V. A. Dzuba, A. Derevianko, and V. V. Flambaum, "Ion clock and search for the variation of the fine-structure constant using optical transitions in Nd^{13+} and Sm^{15+}," *Physical Review A - Atomic, Molecular, and Optical Physics*, vol. 86, p. 054502, Nov. 2012.

[24] J. Guéna, M. Abgrall, D. Rovera, P. Rosenbusch, M. E. Tobar, P. Laurent, A. Clairon, and S. Bize, "Improved Tests of Local Position Invariance Using ^{87}Rb and ^{133}Cs Fountains," *Physical Review Letters*, vol. 109, p. 080801, Aug. 2012.

[25] P. Whibberley, "Optical Atomic Clocks for Space," no. 21641, 2008.

[26] S. Schiller, G. M. Tino, P. Gill, C. Salomon, U. Sterr, E. Peik, A. Nevsky, a. Görlitz, D. Svehla, G. Ferrari, N. Poli, L. Lusanna, H. Klein, H. Margolis, P. Lemonde, P. Laurent, G. Santarelli, A. Clairon, W. Ertmer, E. Rasel, J. Müller, L. Iorio, C. Lämmerzahl, H. Dittus, E. Gill, M. Rothacher, F. Flechner, U. Schreiber, V. Flambaum, W.-T. Ni, L. Liu, X. Chen, J. Chen, K. Gao, L. Cacciapuoti, R. Holzwarth, M. P. Hess, and W. Schäfer, "Einstein Gravity Explorera medium-class fundamental physics mission," *Experimental Astronomy*, vol. 23, pp. 573–610, Nov. 2008.

[27] H. G. Dehmelt, "Mono-Ion Oscillator as Potential Ultimate Laser Frequency Standard," *IEEE Transactions on Instrumentation and measurement*, vol. IM-31, no. 2, pp. 83–87, 1982.

[28] P. Gill, G. P. Barwood, H. Klein, G. Huang, S. A. Webster, P. J. Blythe, K. Hosaka, S. N. Lea, and H. S. Margolis, "Trapped ion optical frequency standards," *Meas. Sci. Technol.*, vol. 14, 2003.

[29] M. Roberts, P. Taylor, G. P. Barwood, P. Gill, H. A. Klein, and W. R. C. Rowley, "Observation of an Electric Octupole Transition in a Single Ion," *Physical Review Letters*, pp. 8–11, 1997.

[30] M. Roberts, P. Taylor, R. B. M. Clarke, W. R. C. Rowley, and P. Gill, "Measurement of the $^2S_{1/2} \rightarrow {}^2D_{5/2}$ clock transition in a single $^{171}Yb^+$ ion," *Physical Review A*, vol. 60, no. 4, pp. 2867–2872, 1999.

[31] M. Roberts, P. Taylor, G. P. Barwood, W. R. C. Rowley, and P. Gill, "Observation of the $^2S_{1/2} \rightarrow {}^2F_{7/2}$ electric octupole transition in a single Yb^+ ion," *Physical Review A*, vol. 62, no. 020501, pp. 1–4, 2000.

[32] P. Blythe, S. Webster, H. Margolis, S. Lea, G. Huang, S. Choi, W. Rowley, P. Gill, and R. Windeler, "Subkilohertz absolute-frequency measurement of the 467 nm electric octupole transition in $^{171}Yb^{+}$," *Physical Review A*, vol. 67, p. 020501, Feb. 2003.

[33] H. R. Telle, B. Lipphardt, and J. Stenger, "Kerr-lens mode-locked lasers as transfer oscillators for optical frequency measurements," *Applied Physics B*, vol. 47, pp. 1–6, July 2002.

[34] Nobelprize.org, "The Nobel Prize in Physics 2005." http://www.nobelprize.org/nobel_prizes/physics/laureates/2005/, 2005.

[35] L. A. M. Johnson, P. Gill, and H. S. Margolis, "Evaluating the performance of the NPL femtosecond frequency combs: Agreement at the 10^{-21} level," *Metrologia*, vol. 52, no. 1, p. 62, 2015.

[36] J. A. Barnes, S. Member, A. R. Chi, L. S. Cutler, J. A. Mullen, W. L. Smith, R. L. Sydnor, R. F. C. Vessot, and G. M. R. Winkler, "Characterization of Frequency Stability," *IEEE Transactions on instruments and measurement*, vol. IM, no. 2, 1971.

[37] J. Rutman and F. L. Walls, "Characterization of frequency stability in precision frequency sources," *Proceedings of the IEEE*, vol. 79, pp. 952–960, Jul 1991.

[38] W. J. Riley, *Handbook of Frequency Stability Analysis*. NIST Special Publication 1065, 2008.

[39] W. M. Itano, J. C. Bergquist, J. J. Bollinger, J. M. Gilligan, D. J. Heinzen, F. L. Moore, M. G. Raizen, and D. J. Wineland, "Quantum projection noise: Population fluctuations in two-level systems," *Physical Review A*, vol. 47, no. 5, 1993.

[40] E. Peik, T. Schneider, and C. Tamm, "Laser frequency stabilization to a single ion," *Journal of Physics B: Atomic, Molecular and Optical Physics*, vol. 39, pp. 145–158, Jan. 2006.

[41] N. Shiga and M. Takeuchi, "Locking the local oscillator phase to the atomic phase via weak measurement," *New Journal of Physics*, vol. 14, p. 023034, Feb. 2012.

[42] H. Margolis, G. Huang, G. Barwood, S. Lea, H. Klein, W. Rowley, P. Gill, and R. Windeler, "Absolute frequency measurement of the 674-nm $^{88}Sr^{+}$ clock transition using a femtosecond optical frequency comb," *Physical Review A*, vol. 67, p. 032501, Mar. 2003.

[43] P. Dubé, A. Madej, Z. Zhou, and J. Bernard, "Evaluation of systematic shifts of the $^{88}Sr^{+}$ single-ion optical frequency standard at the 10^{-17} level," *Physical Review A*, vol. 87, p. 023806, Feb. 2013.

[44] G. P. Barwood, G. Huang, H. A. Klein, L. A. M. Johnson, S. A. King, H. S. Margolis, K. Szymaniec, and P. Gill, "Agreement between two $^{88}Sr^{+}$ optical clocks to 4 parts in 10^{-17}," *Physical Review A*, vol. 89, p. 050501, May 2014.

[45] T. Rosenband, D. B. Hume, P. O. Schmidt, C. W. Chou, A. Brusch, L. Lorini, W. H. Oskay, R. E. Drullinger, T. M. Fortier, J. E. Stalnaker, S. A. Diddams, W. C. Swann, N. R. Newbury, W. M. Itano, D. J. Wineland, and J. C. Bergquist, "Frequency ratio of Al^{+} and Hg^{+} single-ion optical clocks; metrology at the 17th decimal place.," *Science (New York, N.Y.)*, vol. 319, pp. 1808–12, Mar. 2008.

[46] W. M. Itano, J. C. Bergquist, A. Brusch, S. A. Diddams, T. M. Fortier, T. P. Heavner, L. Hollberg, D. B. Hume, S. R. Jefferts, L. Lorini, T. E. Parker, T. Rosenband, and J. E. Stalnaker, "Optical frequency standards based on mercury and aluminum ions," in *Proceedings of SPIE* (R. J. Jones, ed.), vol. 6673, pp. 667303–667303–11, Sept. 2007.

[47] S. Falke, N. Lemke, C. Grebing, B. Lipphardt, S. Weyers, V. Gerginov, N. Huntemann, C. Hagemann, A. Al-Masoudi, S. Hfner, S. Vogt, U. Sterr, and C. Lisdat, "A strontium lattice clock with 3×10^{-17} inaccuracy and its frequency," *New Journal of Physics*, vol. 16, no. 7, p. 073023, 2014.

[48] B. J. Bloom, T. L. Nicholson, J. R. Williams, S. L. Campbell, M. Bishof, X. Zhang, W. Zhang, S. L. Bromley, and J. Ye, "An optical lattice clock with accuracy and stability at the 10^{-18} level.," *Nature*, vol. 506, pp. 71–5, Feb. 2014.

[49] N. Huntemann, C. Sanner, B. Lipphardt, C. Tamm, and E. Peik, "Single-Ion Atomic Clock with 3×10^{-18} Systematic Uncertainty," *Phys. Rev. Lett.*, vol. 116, p. 063001, Feb 2016.

[50] R. Li, K. Gibble, and K. Szymaniec, "Improved accuracy of the NPL-CsF2 primary frequency standard: evaluation of distributed cavity phase and microwave lensing frequency shifts," *Metrologia*, vol. 48, pp. 283–289, Oct. 2011.

[51] J. C. Hafele and R. E. Keating, "Around-the-World Atomic Clocks: Observed Relativistic Time Gains.," *Science (New York, N.Y.)*, vol. 177, pp. 168–170, 1972.

[52] J. P. Uzan, "The fundamental constants and their variation : observational and theoretical status," *Reviews of Modern Physics*, vol. 75, no. April, p. 403, 2003.

[53] W. J. Marciano, "Time Variation of the Fundamental 'Constants' and Kaluza-Klein Theories," *Physical Review Letters*, vol. 52, no. 7, pp. 489–491, 1984.

[54] T. Damour, F. Piazza, and G. Veneziano, "Runaway Dilaton and Equivalence Principle Violations," *Physical Review Letters*, vol. 89, p. 081601, Aug. 2002.

[55] M. J. Duff, "Comment on time-variation of fundamental constants," 2016.

[56] "Dirac Lecture 4 (of 4) - Does 'G' vary? (Large Numbers Hypothesis)." `https://www.youtube.com/watch?v=P174LmmQYy4`, Jan 2013.

[57] C. J. Foot, *Atomic physics*. Oxford University Press, 2012.

[58] V. A. Dzuba and V. V. Flambaum, "Highly charged ions for atomic clocks and search for variation of the fine structure constant," *Hyperfine Interactions*, vol. 236, pp. 79–86, Nov 2015.

[59] V. A. Dzuba and V. V. Flambaum, "Calculation of nuclear-spin-dependent parity nonconservation in S→D transitions of Ba^+, Yb^+, and Ra^+ ions," *Physical Review A*, vol. 83, p. 052513, May 2011.

[60] V. Dzuba and V. Flambaum, "Relativistic corrections to transition frequencies of AgI, DyI, HoI, YbII, YbIII, AuI, and HgII and search for variation of the fine-structure constant," *Physical Review A*, vol. 77, p. 012515, Jan. 2008.

[61] V. Dzuba, V. Flambaum, and M. Marchenko, "Relativistic effects in Sr, Dy, Yb II, and Yb III and search for variation of the fine-structure constant," *Physical Review A*, vol. 68, p. 022506, Aug. 2003.

[62] J. Bagdonaite, P. Jansen, C. Henkel, H. L. Bethlem, K. M. Menten, and W. Ubachs, "A stringent limit on a drifting proton-to-electron mass ratio from alcohol in the early universe.," *Science (New York, N.Y.)*, vol. 339, pp. 46–8, Jan. 2013.

[63] J. K. Webb, J. A. King, M. T. Murphy, V. V. Flambaum, R. F. Carswell, and M. B. Bainbridge, "Indications of a Spatial Variation of the Fine Structure Constant," *Physical Review Letters*, vol. 107, p. 191101, Oct. 2011.

[64] J. Webb, M. Murphy, V. Flambaum, V. Dzuba, J. Barrow, C. Churchill, J. Prochaska, and A. Wolfe, "Further Evidence for Cosmological Evolution of the Fine Structure Constant," *Physical Review Letters*, vol. 87, p. 091301, Aug. 2001.

[65] E. Angstmann, V. Dzuba, and V. Flambaum, "Relativistic effects in two valence-electron atoms and ions and the search for variation of the fine-structure constant," *Physical Review A*, vol. 70, p. 014102, July 2004.

[66] N. Leefer, C. Weber, and A. Cingöz, "New limits on variation of the fine-structure constant using atomic Dysprosium," *Physical Review Letters*, Jan. 2013.

[67] E. Biémont, J.-F. Dutrieux, I. I. Martin, and P. Quinet, "Lifetime Calculations in Yb II," *J. Phys. B: At. Mol. Opt. Phys.*, vol. 3321, no. 31, 1998.

[68] P. Taylor, M. Roberts, G. P. Barwood, and P. Gill, "Combined optical-infrared single-ion frequency standard," *Optics Letters*, vol. 23, no. 4, 1998.

[69] R. H. Dicke, "The Effect of Collisions upon the Doppler Width of Spectral Lines.," *Physical Review*, vol. 89, no. 2, 1953.

[70] D. J. Berkeland and M. G. Boshier, "Destabilization of dark states and optical spectroscopy in Zeeman-degenerate atomic systems," *Physical Review A*, p. 14, Nov. 2001.

[71] BIPM, "Recommended values of standard frequencies," *Practical realizations of the definitions of some important units*, vol. 11 May, no. 31, 2016.

[72] T. Pruttivarasin, M. Ramm, S. Porsev, I. Tupitsyn, M. S. Safronova, M. A. Hohensee, and H. A. Häffner, "Michelson-Morley analogue for electrons using trapped ions to test Lorentz symmetry," *Nature*, vol. 517, no. 517, 2014.

[73] V. A. Dzuba, V. V. Flambaum, M. S. Safronova, S. G. Porsev, T. Pruttivarasin, M. A. Hohensee, and H. Häffner, "Strongly enhanced effects of Lorentz symmetry violation in entangled Yb^+ ions," *Nature Physics*, vol. 12, no. 517, 2014.

[74] C. Delaunay, R. Ozeri, P. Gilad, and Y. Soreq, "Probing the Atomic Higgs Force," *arxiv.org*, no. arXiv:1601.05087v2 [hep-ph], 2016.

[75] D. Leibfried, R. Blatt, C. Monroe, and D. Wineland, "Quantum dynamics of single trapped ions," *Rev. Mod. Phys.*, vol. 75, pp. 281–324, Mar 2003.

[76] M. Brownutt, M. Kumph, P. Rabl, and R. Blatt, "Ion-trap measurements of electric-field noise near surfaces," *Reviews of Modern Physics*, no. 87, p. 1419, 2015.

[77] R. J. Epstein, S. Seidelin, D. Leibfried, J. H. Wesenberg, J. J. Bollinger, J. M. Amini, R. B. Blakestad, J. Britton, J. P. Home, W. M. Itano, J. D. Jost, E. Knill, C. Langer, R. Ozeri, N. Shiga, and D. J. Wineland, "Simplified motional heating rate measurements of trapped ions," *Phys. Rev. A*, vol. 76, p. 033411, Sep 2007.

[78] C. Schrama, E. Peik, W. Smith, and H. Walther, "Novel miniature ion traps," *Optics Communications*, vol. 101, no. 1, pp. 32 – 36, 1993.

[79] T. Rosenband, P. Schmidt, D. Hume, W. Itano, T. Fortier, J. Stalnaker, K. Kim, S. Diddams, J. Koelemeij, J. Bergquist, and D. Wineland, "Observation of the $^1S_0 \rightarrow {}^3P_0$ Clock Transition in $^{27}Al^+$," *Physical Review Letters*, vol. 98, p. 220801, May 2007.

[80] M. Doležal, P. Balling, P. B. R. Nisbet-Jones, S. A. King, J. M. Jones, H. A. Klein, P. Gill, T. Lindvall, A. E. Wallin, M. Merimaa, C. Tamm, C. Sanner, N. Huntemann, N. Scharnhorst, I. D. Leroux, P. O. Schmidt, T. Burgermeister, T. E. Mehlstäubler, and E. Peik, "Analysis of thermal radiation in ion traps for optical frequency standards," *Metrologia*, vol. 52, no. 6, p. 842, 2015.

[81] NPL, "Image of Sr Ion Trap."

[82] J. H. Wesenberg, R. J. Epstein, D. Leibfried, R. B. Blakestad, J. Britton, J. P. Home, W. M. Itano, J. D. Jost, E. Knill, C. Langer, R. Ozeri, S. Seidelin, and D. J. Wineland, "Fluorescence during doppler cooling of a single trapped atom," *Phys. Rev. A*, vol. 76, p. 053416, Nov 2007.

[83] R. W. P. Drever, J. L. Hall, F. V. Kowalski, J. Hough, G. M. Ford, A. J. Munley, and H. Ward, "Laser phase and frequency stabilization using an optical resonator," *Applied Physics B: Lasers and Optics*, vol. 31, pp. 97–105, June 1983.

[84] E. D. Black, "An introduction to PoundDreverHall laser frequency stabilization," *American Journal of Physics*, vol. 69, no. 1, p. 79, 2001.

[85] NPL, "Low Drift Etalons." `http://www.npl.co.uk/science-technology/time-frequency/products-and-services/products-and-services/low-drift-etalons`, 2018.

[86] L.-S. Ma, P. Jungner, J. Ye, and J. L. Hall, "Delivering the same optical frequency at two places: accurate cancellation of phase noise introduced by an optical fiber or other time-varying path," *Opt. Lett.*, vol. 19, pp. 1777–1779, Nov 1994.

[87] T. W. Hansch and B. Couillaud, "Laser frequency stabilization by polarization spectroscopy of a reflecting reference cavity," *Optics Communications*, vol. 35, pp. 441–444, Dec. 1980.

[88] R. Paschotta, "Article on Finesse in the Encyclopedia of Laser Physics and Technology," *https://www.rp-photonics.com/finesse.html*.

[89] W. Bowden, I. R. Hill, P. E. G. Baird, and P. Gill, "Note: A high-performance, low-cost laser shutter using a piezoelectric cantilever actuator," *Review of Scientific Instruments*, vol. 88, no. 1, p. 016102, 2017.

[90] I. Sobelman, *Atomic Spectra and Radiative Transitions*. New York: Springer-Verlag, 1979.

[91] V. I. Yudin, a. V. Taichenachev, C. W. Oates, Z. W. Barber, N. D. Lemke, A. D. Ludlow, U. Sterr, C. Lisdat, and F. Riehle, "Hyper-Ramsey spectroscopy of optical clock transitions," *Physical Review A*, vol. 82, p. 011804, July 2010.

[92] N. Huntemann, B. Lipphardt, M. Okhapkin, C. Tamm, E. Peik, A. V. Taichenachev, and V. I. Yudin, "A generalized Ramsey excitation scheme with suppressed light shift," *Physical Review Letters*, p. 5, Sept. 2012.

[93] R. Hobson, W. Bowden, S. A. King, P. E. G. Baird, I. R. Hill, and P. Gill, "Modified hyper-Ramsey methods for the elimination of probe shifts in optical clocks.," *Physical Review A*, vol. 93, no. 010501(R), 2016.

[94] E. Riis and A. G. Sinclair, "Optimum measurement strategies for trapped ion optical frequency standards," *Journal of Physics B: Atomic, Molecular and Optical Physics*, vol. 37, pp. 4719–4732, Dec. 2004.

[95] J. C. Bergquist, A. Brusch, S. A. Diddams, T. A. Fortier, T. P. Heavner, L. Hollberg, D. B. Hume, S. R. Jefferts, L. Lorini, T. E. Parker, T. Rosenband, J. E. Stalnaker, and D. J. Wineland, "Stable and accurate single-ion optical clocks," in *Proceedings of the 2nd International Conference on TIME AND MATTER*, pp. 3–18, University of Nova Gorica Press, 2008.

[96] J. R. P. Angel and P. G. H. Sandars, "The Hyperfine Structure Stark Effect. I. Theory," *Proceedings of the Royal Society A: Mathematical, Physical and Engineering Sciences*, vol. 305, pp. 125–138, May 1968.

[97] E. Biémont, J.-F. Dutrieux, I. I. Martin, and P. Quinet, "Lifetime Calculations in Yb II," *J. Phys. B: At. Mol. Opt. Phys.*, vol. 3321, no. 31, 1998.

[98] T. Schneider, E. Peik, and C. Tamm, "Sub-Hertz Optical Frequency Comparisons between Two Trapped $^{171}Yb^{+}$ Ions," *Phys. Rev. Lett.*, vol. 94, p. 230801, Jun 2005.

[99] S. N. Lea, S. A. Webster, and G. P. Barwood, "Polarisabilities and blackbody shifts in Sr^{+} and Yb^{+}," in *Proceedings of the 20th European Frequency and Time Forum*, pp. 302–307, March 2006.

[100] C. W. Chou, D. B. Hume, T. Rosenband, and D. J. Wineland, "Optical clocks and relativity.," *Science (New York, N.Y.)*, vol. 329, pp. 1630–3, Sept. 2010.

[101] D. J. Berkeland, J. D. Miller, J. C. Bergquist, W. M. Itano, and D. J. Wineland, "Minimization of ion micromotion in a Paul trap," *Journal of Applied Physics*, vol. 83, no. 10, 1998.

[102] J. Keller, H. L. Partner, T. Burgermeister, and T. E. Mehlstubler, "Precise determination of micromotion for trapped-ion optical clocks," *Journal of Applied Physics*, vol. 118, no. 10, p. 104501, 2015.

[103] W. M. Itano, "External-Field Shifts of the $^{199}Hg^{+}$ Optical Frequency Standard," *Journal of Research of the National Institue of Standards and Technology*, vol. 105, no. 6, pp. 829–837, 2000.

[104] J. Stenger, C. Tamm, N. Haverkamp, S. Weyers, and H. R. Telle, "Absolute frequency measurement of the 435.5 nm ^{171}Yb+ clock transition with a Kerr-lens mode-locked femtosecond laser," *Opt. Lett.*, vol. 26, pp. 1589–1591, Oct 2001.

[105] C. Tamm, B. Lipphardt, H. Schnatz, R. Wynands, S. Weyers, T. Schneider, and E. Peik, "$^{171}Yb^{+}$ Single-Ion Optical Frequency Standard at 688 THz," *IEEE Transactions on Instrumentation and Measurement*, vol. 56, pp. 601–604, April 2007.

[106] C. Tamm, S. Weyers, B. Lipphardt, and E. Peik, "Stray-field-induced quadrupole shift and absolute frequency of the 688-THz $^{171}Yb^{+}$ single-ion optical frequency standard," *Phys. Rev. A*, vol. 80, p. 043403, Oct 2009.

[107] S. Webster, R. Godun, S. King, G. Huang, B. Walton, V. Tsatourian, H. Margolis, S. Lea, and P. Gill, "Frequency measurement of the $^{2}S_{1/2} \rightarrow ^{2}D_{3/2}$ electric quadrupole transition in a single $^{171}Yb^{+}$ ion," *IEEE Transactions on Ultrasonics, Ferroelectrics, and Frequency Control*, vol. 57, pp. 592–599, March 2010.

[108] C. Tamm, N. Huntemann, B. Lipphardt, V. Gerginov, N. Nemitz, M. Kazda, S. Weyers, and E. Peik, "Cs-based optical frequency measurement using cross-linked optical and microwave oscillators," *Physical Review A*, vol. 89, p. 023820, Feb. 2014.

[109] K. Hosaka, S. A. Webster, A. Stannard, B. R. Walton, H. S. Margolis, and P. Gill, "Frequency measurement of the $^{2}S_{1/2}-^{2}F_{7/2}$ electric octupole transition in a single $^{171}Yb^{+}$ ion," *Phys. Rev. A*, vol. 79, p. 033403, Mar 2009.

[110] S. Falke, H. Schnatz, J. S. R. V. Winfred, T. Middelmann, S. Vogt, S. Weyers, B. Lipphardt, G. Grosche, F. Riehle, U. Sterr, and C. Lisdat, "The ^{87}Sr optical frequency standard at PTB," *Metrologia*, vol. 48, no. 5, p. 399, 2011.

[111] H. S. Margolis, R. M. Godun, P. Gill, L. A. M. Johnson, S. L. Shemar, P. B. Whibberley, D. Calonico, F. Levi, L. Lorini, M. Pizzocaro, P. Delva, S. Bize, J. Achkar, H. Denker, L. Timmen, C. Voigt, S. Falke, D. Piester, C. Lisdat, U. Sterr, S. Vogt, S. Weyers, J. Gersl, T. Lindvall, and M. Merimaa, "International timescales with optical clocks (ITOC)," in *2013 Joint European Frequency and Time Forum International Frequency Control Symposium (EFTF/IFC)*, pp. 908–911, July 2013.

[112] "Circular T publication from June 2015." `ftp://ftp2.bipm.org/pub/tai//Circular-T/cirt/cirt.330`.

[113] C. F. A. Baynham, R. M. Godun, J. M. Jones, S. A. King, P. B. R. Nistbet-Jones, F. Baynes, A. Rolland, P. E. G. Baird, K. Bongs, P. Gill, and H. S.

Margolis, "Absolute frequency measurement of the $^2S_{1/2} \rightarrow ^2 F_{7/2}$ optical clock transition in $^{171}Yb^+$ with an uncertainty of 4×10^{16} using a frequency link to International Atomic Time," *arXiv*, p. 1707.00646, July 2017.

[114] "Optical frequency transfer a European network." `http://www.ptb.de/emrp/often_home.html`.

[115] N. Poli, C. Oates, P. Gill, and G. Tino, "Optical Atomic Clocks," *La Rivista del Nuovo Cimento della Societa Italiana di Fisica*, vol. 36, no. 12, 2013.